COPPE
Instituto Alberto Luiz Coimbra de Pós-Graduação e Pesquisa de Engenharia
UFRJ

DATA-DRIVEN CALIBRATION OF COMPUTATIONAL COMBUSTION MODELS EMPLOYING REDUCED CHEMICAL KINETICS

Rodolfo da Silva Machado de Freitas

Tese de Doutorado apresentada ao Programa de Pós-graduação em Engenharia Mecânica, COPPE, da Universidade Federal do Rio de Janeiro, como parte dos requisitos necessários à obtenção do título de Doutor em Engenharia Mecânica.

Orientador: Fernando Alves Rochinha

Rio de Janeiro
Agosto de 2020

DATA-DRIVEN CALIBRATION OF COMPUTATIONAL COMBUSTION MODELS EMPLOYING REDUCED CHEMICAL KINETICS

Rodolfo da Silva Machado de Freitas

TESE SUBMETIDA AO CORPO DOCENTE DO INSTITUTO ALBERTO LUIZ COIMBRA DE PÓS-GRADUAÇÃO E PESQUISA DE ENGENHARIA DA UNIVERSIDADE FEDERAL DO RIO DE JANEIRO COMO PARTE DOS REQUISITOS NECESSÁRIOS PARA A OBTENÇÃO DO GRAU DE DOUTOR EM CIÊNCIAS EM ENGENHARIA MECÂNICA.

Orientador: Fernando Alves Rochinha

Aprovada por: Prof. Fernando Alves Rochinha
Prof. Rubens Sampaio Filho
Prof. Alvaro Luiz Gayoso de Azeredo Coutinho
Prof. Helcio Rangel Barreto Orlande
Prof. Thiago Gamboa Ritto

RIO DE JANEIRO, RJ – BRASIL
AGOSTO DE 2020

Freitas, Rodolfo da Silva Machado de

Data-driven Calibration of Computational Combustion Models Employing Reduced Chemical Kinetics/Rodolfo da Silva Machado de Freitas. – Rio de Janeiro: UFRJ/COPPE, 2020.

XIII, 101 p.: il.; 29, 7cm.

Orientador: Fernando Alves Rochinha

Tese (doutorado) – UFRJ/COPPE/Programa de Engenharia Mecânica, 2020.

Referências Bibliográficas: p. 77 – 88.

1. Uncertainty Quantification. 2. Combustion. 3. Model Discrepancy. 4. Deep Learning. I. Rochinha, Fernando Alves. II. Universidade Federal do Rio de Janeiro, COPPE, Programa de Engenharia Mecânica. III. Título.

Dedico esta Tese a minha família, que muito me apoiou e incentivou a realizá-la.

Agradecimentos

Em primeiro lugar, gostaria de agradecer a todos os meus familiares que ajudaram, apoiaram e acreditaram nas minhas decisões. Em especial, gostaria de agradecer pelo apoio e paciência da minha namorada Vitória. Apesar dos muitos dias e noites de trabalho, ela ficou ao meu lado e me ajudou a passar por esta etapa.

Em seguida, gostaria de agradecer ao meu orientador Prof. Fernando Alves Rochinha. O processo de obtenção do meu doutorado me levou a muitos tópicos de pesquisa, alguns dos quais eu não tinha nenhuma experiência. Sem seus conselhos e orientação, obter meu doutorado teria sido praticamente impossível.

Gostaria de também agradecer ao Prof. Xi Jiang (Queen Mary – University of London) e ao pesquisador Daniel Mira (Barcelona Supercomputing Center). Ao longo da minha pesquisa, a ajuda do Prof. Xi e do Daniel no esclarecimento de certos conceitos de combustão foi inestimável para melhorar o meu conhecimento neste tópico.

Gostaria de agradecer também a todos os professores da COPPE pelos ensinamentos passados, em especial aos professores do Programa de Engenharia Mecânica. Aqui também vai meu agradecimento aos amigos do Laboratório de Mecânica dos Sólidos (LMS) que estiveram presentes colaborando, apoiando e incentivando durante esta jornada.

Por fim, gostaria de agradecer a fundação COPPETEC que viabilizou em parte o desenvolvimento desta pesquisa de Tese, sobretudo através do projeto de pesquisa High Perfomance Computing for Energy (`https://hpc4e.eu/`). Aqui, também gostaria de agradecer a CAPES pelo financiamento de um período de doutorado sanduíche na Queen Mary – University of London.

Enfim, a todas as pessoas que ajudaram, apoiaram e acreditaram em mim durante essa jornada.

Resumo da Tese apresentada à COPPE/UFRJ como parte dos requisitos necessários para a obtenção do grau de Doutor em Ciências (D.Sc.)

CALIBRAÇÃO ORIENTADA POR DADOS DE MODELOS COMPUTACIONAIS DE COMBUSTÃO EMPREGANDO CINÉTICA QUÍMICA REDUZIDA

Rodolfo da Silva Machado de Freitas

Agosto/2020

Orientador: Fernando Alves Rochinha

Programa: Engenharia Mecânica

Nesta tese, é adotada uma abordagem probabilística de discrepância encapsulada para entender os limites do uso de cinética química reduzida em modelos computacionais de combustão e também melhorar a capacidade de tais modelos prever quantidades de interesse importantes. Além disso, é proposta uma abordagem de aprendizagem profundo de discrepância de modelo encapsulada. Mais especificamente, uma rede neural profunda é imersa como uma função aditiva para modelar a evolução temporal das concentrações de espécies químicas que servem como termo fontes para o escoamento. Uma calibração orientada a dados é adotada com um conjunto de dados produzido por simulações numéricas de mecanismos detalhados, em uma calibração bayesiana modelo-a-modelo. Os métodos propostos são avaliados em cenários de combustão de referência, amplamente utilizados para avaliar o papel desempenhado pela cinética química nas principais propriedades físico-químicas que caracterizam os sistemas de combustão. Os cenários correspondem aos casos de aplicação de combustão homogênea durante autoignição e propagação da chama. Os resultados demonstram a capacidade das abordagens adotadas para otimizações de modelos de cinética química. Mostra-se como o alcance de aplicação do modelo químico reduzido pode ser estendida para prever quantidades de interesse sem aumentar o número de espécies reagentes no sistema de combustão e a um custo computacional reduzido.

Abstract of Thesis presented to COPPE/UFRJ as a partial fulfillment of the requirements for the degree of Doctor of Science (D.Sc.)

DATA-DRIVEN CALIBRATION OF COMPUTATIONAL COMBUSTION MODELS EMPLOYING REDUCED CHEMICAL KINETICS

Rodolfo da Silva Machado de Freitas

August/2020

Advisor: Fernando Alves Rochinha

Department: Mechanical Engineering

In this thesis, a probabilistic embedded discrepancy approach to understanding the limits of the use of reduced chemical kinetics in computational combustion models and also to improve the ability of such models to predict key quantities of interest is adopted. Also, an embedded deep learning model discrepancy approach is proposed. More specifically, a deep neural network is embedded as an additive function to model the temporal evolution of chemical species concentrations that serves as a source to the flow field. A data-driven calibration is adopted with data set produced by numerical simulation of detailed mechanisms, in a model-to-model Bayesian calibration. These proposed strategies are evaluated in benchmark combustion scenarios widely used to evaluate the role played by chemical kinetics on main physicochemical properties characterizing combustion systems. The scenarios correspond to the application cases of homogeneous combustion during autoignition and flame propagation. The results demonstrate the ability of adopted approaches for model calibration in chemical kinetics. It is shown how the application range of the reduced chemical model can be extended to predict quantities of interest without increasing the number of reacting species in the combustion system and at a reduced computational cost.

Contents

List of Figures

List of Tables

Chapter 1

Introduction

The development of computational models for characterization of physical systems is of major relevance in engineering applications. In particular, computational models are an essential topic of combustion research nowadays. In large applications, combustion simulations are supporting the design and optimization of internal combustion engines, such as solid-fuel rocket motors, industrial burners and furnaces, and gas turbine combustors, using the power of parallel supercomputers [3].

From a macroscopic perspective, the governing equations for combustion are the Navier-Stokes equations, which include the balance of mass, momentum and energy in addition to conservation for N chemical species into mixture, including source terms associated with chemical reactions [4, 5]. Computational combustion models of practical engineering systems require an extensive computational burden. Those simulations must combine the capability to predict the relevant flow features with the ability to solve the relevant chemistry involved in the combustion process, as well as any other important physical phenomena. Thus, like many other research areas, combustion researches is highly dependent on the progress of the computer power.

The continual growth in computing power has become feasible the increase in the size and complexity of combustion models. This growth can be measured by the number of grid points in Computational Fluid Dynamics (CFD) calculations, in the number of chemical species and reactions in the chemical kinetics mechanisms, in the spatial refinement of Direct Numerical Simulations (DNS) of turbulent flows. Therefore, increasing computer power enabled combustion models to embed a greater level of complexity and realism in computational simulations. Specifically, this has made possible to emerge more coupled physical and chemical processes in the models, a more complex turbulence model, a more sophisticated radiation model, multiple phase phenomena such as a spray model or a soot model, or moving objects such as intake valves or piston blades [3].

In power and propulsion applications such as engines, the thermal energy

contained in the fuel is usually converted to heat through combustion. This process is responsible not only to provide the heat release rate and power output, but also for dictating the formation of pollutants. Also, there is a complex interaction between the chemical reactions and the flow field, specially when the flow is turbulent. There are many studies dedicated to developing computational predictive models for turbulent flows [6] and turbulent reacting flows [7, 8], with the latter showing a high influence of the chemistry in the flow. While CFD has been traditionally used in the context of Reynolds-Averaged Navier-Stokes (RANS), the application of Large-Eddy-Simulation (LES) and direct numerical simulations (DNS) has been largely extended [9] thanks to the advances in computing power.

Despite the advancement in numerical calculations and computing power, the challenge of modeling detailed chemistry is not alleviated. The majority of computational combustion models to simulate practical applications fall in the use of low fidelity chemical mechanisms to make these simulations computationally feasible since chemical reaction mechanisms are frequently the most computationally demanding of a computational combustion model.

Chemical mechanisms and kinetics models describe the processes and rates of chemical reactions [4]. In general, the chemistry involved in the oxidation process of a reactive mixture can be excessively complex and highly non-linear. Detailed description of a reactive process, for example the hydrocarbon combustion, typically involves hundreds or thousands of chemical reactions with hundreds of chemical species, leading to tens of thousands of chemical kinetic parameters [10]. In the most common formulation, a time-dependent stiff differential equation describes the evolution of the mass fraction for each chemical species.

Reaction mechanisms capable of describing chemical kinetics must be able to correctly describe the separate chemical evolution of the major species relevant to pollutant formation along with the heat release rate coming from combustion. The use of detailed chemical kinetic models in CFD, including LES or DNS, can pose a significant challenge for the calculation of turbulent reacting flows in complex geometries under engine-like conditions, unless techniques for chemistry reduction are used [11, 12]. Usually to reduce the computational cost, reduced reaction mechanisms are employed to describe the kinetics of the combustion process [10–12]. However, reduced mechanisms can be inadequate, leading to a detectable inconsistency between model predictions and observations [13]. Therefore, consisting in a major source of uncertainties in the modelling.

In addition to errors introduced by computing the reactive process chemistry by reduced kinetics, there is a large number of parametric uncertainties in chemical kinetics models. In practice, kinetic parameters are estimated through indirect, scarce and noisy measurements. Hence, there is a large number of parametric

uncertainties in chemical kinetics models, involving reaction rate constants and thermodynamic parameters, many of which are poorly known [14–16]. They also present strong non-linearities that can intensify small parametric uncertainties, leading to large uncertainties in predictions.

1.1 Objectives

In the present work, the motivation relies on the use of computer models for describing biogas combustion. More particularly, on Uncertainty Quantification (UQ) related problems. Biogas is a mixture of methane diluted with CO_2, it is composed of 40–75% of methane, 25–55% of carbon dioxide (and possibly 0–10% of hydrogen). Biogas originates from the fermentation of biomass by anaerobic bacteria. It can be produced from organic wastes, energetic plants and sources of biomass. Its many applications include the combined generation of heat and electricity and its conversion into liquid or gaseous fuels and hydrogen [17, 18].

One of the major problems related to the application of biogas is that such fuels do not have reliable models for describing the closure equations of chemistry kinetics. Reaction mechanisms capable of describing biogas chemical kinetics must be able to correctly describe the chemical evolution of the major or relevant species along with the heat release rate coming from the exothermic process. However, this is not a sufficient condition since the simultaneous presence of methane and carbon dioxide can change the chemical behavior of the whole system in an unpredictable fashion. Consequently, there is a need to evaluate how well reaction mechanisms accounting for the combustion of hydrocarbons perform for the combustion of biogas. In general, detailed kinetic mechanisms developed for simulation of light hydrocarbons combustion appears to be appropriate for reliable simulations of biogas combustion [19].

Given the considerable computational costs involved, CFD simulations of real combustion industrial systems necessitates the utilization of simplified chemical kinetic models [20] which themselves are obtained from the systematic reduction of detailed reaction mechanisms [21, 22]. The accuracy and reliability of a reduced model are always inferior to those of the detailed mechanism.

As biogas combustion processes are likely to be used more extensively due to the lower emissions, it is needed the evaluation of using reduced mechanisms for biogas combustion simulations. The purpose of this work is to analyze the impact of using reduced kinetic mechanisms in biogas combustion through an UQ perspective.

Particularly, model discrepancy (also referred to as model errors or structural errors), expressing the difference between high and low fidelity models regarding the captured physics, is a critical issue that affects different realms of computational

models and engineering. A discrepancy in the model is demonstrated when the imperfections lead to a detectable inconsistency between the model and observations [13, 23]. In combustion processes, model discrepancies resulting from employing simplified physics or chemistry, motivated by the need for seeking a balance between easiness of computation and accuracy along the simulations, tend to be difficult to handle.

In order to improve the predictability of the kinetics in combustion modeling, a probabilistic perspective can be adopted to describe such uncertainty. Stochastic Bayesian inference in the realm of UQ has become a common approach to handle model inadequacy [24–26] and parametric uncertainties. It is considered a powerful framework for combining experimental (or field) data with prior knowledge to develop chemical kinetics models and quantify the associated uncertainties in model structure [1].

As a start point, the aim of the present work is focused on employ advanced UQ techniques in calibrating reduced kinetic models for this flow conditions, thereby enabling predictions with quantified uncertainty that provide an indication of the error in particular quantities of interest, relative to the detailed model. A model-to-model Bayesian calibration approach is adopted to understanding the limits of such low-fidelity models. The objective is the calibration of a reduced chemistry model designed for biogas combustion using Bayesian embedded model-error representation [27]. The key advantage of this method is that it represents discrepancy due to model structure, and associated predictive uncertainty. In the present context, it offers predictions with error bars, to any model output variable, that include structural uncertainty due to the simple form of the reduced kinetic models, relative to a detailed model.

Also, it is presented a topic that involves the construction of a surrogate model using deep learning to evaluate the degree of uncertainty due to the fluctuations of model parameters. Deep neural networks are becoming a widely use tool in surrogate constructing community due to their robustness and generalization property. In order to improve the computational efficiency, a deep neural network surrogate is constructed for uncertainty quantification analysis.

The final topic of the present work involves the construction of a neural network model discrepancy. The model discrepancy representation is embedded as a source term in the equations describing the evolution of the chemical system. Also, the model inadequacy is constructed using a deep neural network, wherein chemical system outputs are fed repeatedly back into the neural network as inputs to compute the full evolution of the chemical system.

1.2 Outline

Building upon the above introduction and objectives, this dissertation is laid out as follows. Chapter 2 presents the Kinetics and Combustion models used in the present thesis. Next, Chapter 3 presents a model-to-model Bayesian calibration approach to understanding the limits of using reduced models to predict biogas combustion performance. Also, an embedded machine learning approach is proposed to characterize the model error inherent in the use of low-fidelity physical models. In Chapter 4, the results achieved are presented. These consist of combustion properties obtained using a calibrated reduced mechanism that accounts for model discrepancy via probabilistic embedding. After, a deep neural surrogate model is constructed to evaluate the variability of the flame characteristics in different operations conditions, defined by equivalence ratio, pressure and inlet temperature, promoted by the Arrhenius parameters of the reduced mechanism. Finally, the results of the embedded deep learning discrepancy model approach are depicted. Chapter 5 presents the conclusions and future research directions.1

Chapter 2

Mathematical Models

The development of physics-based computational models combines reliable theoretical first principles (governing equations) with phenomenological accumulated knowledge (closure equations). Also, a physics-based model can be informally defined as an inputs-outputs relationship. More specifically, a model describes how predictions of specific quantities of interest (QoI's) of the system are related to input variables [1, 28–30]. In particular, mathematical modeling of combustion or reacting flows involves multiple species reacting through multiple chemical reactions. Most computational combustion models are built based on balance equations of fluid mechanics, which are combined with chemical kinetic models, being those derived, often, by experts and a limited number of experiments. Figure 2.1 depicts an overview of a typical combustion model. Inputs may be related to operating conditions variables such as pressure, inlet temperature, fuel/oxidizer mixture, etc, with specific outputs such as burnt mass fractions, ignition delay time, flame speed, delivered energy, etc.

In combustion flows, fuel and oxidizer combine and react to form products. In this process, the reactants through various chemical pathways will form intermediate species, which will ultimately react to form the combustion products. Hence, combustion modeling must combine the capability to solve the relevant flow features with the ability to solve the relevant chemistry, as well as any other important physical phenomena. Traditionally, the majority of combustion processes are

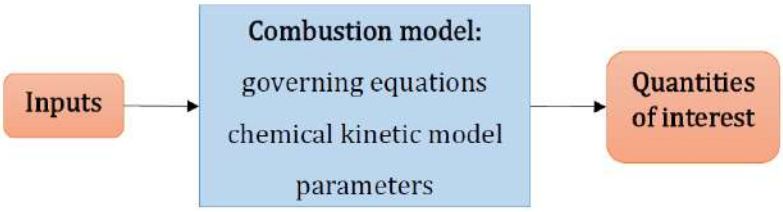

Figure 2.1: An overview of a combustion model, adapted from [1].

modeled through balance equations for reacting flows [5]. Being that, reactive flows are all types of fluid flows in which chemical reactions occurs. So, this chapter presents a brief overview of mathematical models for reacting flows, as well as the introduction of the main physicochemical properties that characterize them. More specifically, physicochemical properties are physical properties, i.e. any property that is measurable, whose value describes a state of a physical system, and properties or chemical attributes that define a chemical process. In the following, a brief introduction to the basic concepts of chemical kinetics models is introduced followed by a description of the combustion scenarios studied in this thesis. The scenarios, organized in a hierarchy from the most simple to more complex, consist of the zero-dimensional reactor [31, 32] and laminar premixed flame [4, 5, 31, 33]. These are well-known scenarios explored from theoretical, experimental and numerical standpoints. Computational models for these scenarios are very important because they are one of the few models where comparisons can be performed between the computation predictions and results from theory and experiments. Furthermore, the laminar flame is widely used to validate chemical models and is the foundation to build more complex turbulent combustion models such as flamelet models, which each element of the flame front can be viewed as a small laminar flame [5]. In fact, those scenarios are often used in the literature to evaluate the accuracy and reliability of reaction mechanisms [34].

2.1 Governing equations for reacting flows

In combustion flows, more specifically chemically reacting flows, chemical reactions are triggered by the flow local thermodynamic states and species (hydrocarbons, oxygen, hydrogen, etc) concentrations. So, there are important differences between the mathematical modeling of reacting and non-reacting flows. First, a reacting gas is a non-isothermal mixture of species which must be treatable individually, where the reacting species and the rates at which these reactions take place require modeling. Since the flow conveys a mixture of species, transport coefficients such as heat diffusivity, species diffusion, viscosity, and others physical properties require specific attention.

Here, the governing equations for chemically reacting flows are presented from a continuum mechanics perspective [4, 5]. So, the compressible Navier-Stokes equations is extended to chemical reacting flows as follows,

$$\frac{\partial \rho}{\partial t} + \nabla \cdot (\rho \mathbf{v}) = 0 \tag{2.1}$$

$$\frac{\partial \rho Y_k}{\partial t} + \nabla \cdot [\rho Y_k (\mathbf{v} + \mathbf{V}_k)] = \dot{\omega}_k, \quad k = 1, .., N \tag{2.2}$$

$$\rho \left(\frac{\partial \mathbf{v}}{\partial t} + \mathbf{v} \cdot \nabla \mathbf{v} \right) = -\nabla p + \nabla \cdot \tau + \rho \sum_{k=1}^{N} Y_k \mathbf{f}_k \tag{2.3}$$

$$\rho c_p \left(\frac{\partial T}{\partial t} + \mathbf{v} \cdot \nabla T \right) = \dot{\omega}_T + \left(\frac{\partial p}{\partial t} + \mathbf{v} \cdot \nabla p \right) + -\nabla \cdot \mathbf{q} + \dot{\mathbf{Q}} + \Phi + \rho \sum_{k=1}^{N} Y_k \mathbf{f}_k \mathbf{V}_k \tag{2.4}$$

where the governing equations consist of mass conservation (2.1), chemical species conservation (2.2), momentum conservation (2.3), and energy conservation (2.4). In Eqs. (2.1)-(2.4), ρ, c_p, T, $\mathbf{v}$ are the density, specific heat capacity, temperature of the mixture and velocity vector of the fluid respectively, while $\mathbf{V}_k$ and $\dot{\omega}_k$ are the diffusion velocity and net production rate of chemical species k from 1 to N (total number of species), respectively.

Additionally, the term $\mathbf{f}_k$ in the momentum equation represents the volume force acting on species. Moreover, $\dot{\mathbf{Q}}$ represents a heat source term. The energy flux $\mathbf{q}$ due the heat and species diffusion is expressed as follows

$$\mathbf{q} = -\lambda \nabla T + \rho \sum_{k=1}^{N} h_k Y_k \mathbf{V}_k. \tag{2.5}$$

where, Φ is the mixture viscous heating source term.

Note that in a three-dimensional geometry combustion models require solving for N+5 variables instead of 5. Since the detailed description of a reactive process typically involves hundreds of chemical species, the first significant effort in computational combustion models is due to the increase in the number of conservation equations to compute.

Also, the closure equations which describe the chemical interactions between species are modeled using a set of differential equations defined by the law of mass action [4]. More specifically, these chemical interactions acting as source terms into chemical species conservation equation (2.2), through the net production rates of species $\dot{\omega}_k$, and also the heat release $\dot{\omega}_T$ due to the chemical process in the energy equation (2.4). These chemical closure relations are further explored in the next section.

After defining the governing equations for reacting flows, the main physical properties of combustion models are introduced. In most combustion models,

chemical species are characterized through their mass fractions Y_k defined by

$$Y_k = \frac{m_k}{m} \qquad k = 1, \ldots, N \tag{2.6}$$

where N and is the number of chemical species in the reacting mixture, m_k is the mass of species k present in a given volume V, and m is the total mass of mixture.

Considering that the mixture is composed of N perfect gases, the total pressure is defined by the sum of the partial pressures

$$p = \sum_{k=1}^{N} p_k \quad \text{with } p_k = \rho_k \frac{RT}{W_k} \tag{2.7}$$

where T is the temperature, $R = 8.314$ J/molK is the ideal gas constant, $\rho_k = \rho Y_k$ and W_k are the density and molecular weight of the k-th species, respectively. Here, the density of the mixture is given by,

$$\rho = \sum_{k=1}^{N} \rho_k. \tag{2.8}$$

So, the total pressure of the mixture is,

$$p = \rho \frac{RT}{W} \tag{2.9}$$

where W is the mean molecular weight of the mixture defined as follows,

$$\frac{1}{W} = \sum_{k=1}^{N} \frac{Y_k}{W_k}. \tag{2.10}$$

For reacting flows, the enthalpy h_k of the chemical species is defined by,

$$h_k = \int_{T_0}^{T} c_{p_k} dT + \Delta h_k^0 \tag{2.11}$$

where Δh_k^0 is the mass enthalpy of formation of species k at reference temperature T_0. Usually, the standard reference temperature used to calculate formation enthalpies is set to $T_0 = 298.15$K [35]. c_{p_k} is heat capacity at constant pressure of the species, wherein the heat capacity of the mixture is given as

$$c_p = \sum_{k=1}^{N} c_{p_k} Y_k. \tag{2.12}$$

Therefore, the total enthalpy is given by

$$h = \sum_{k=1}^{N} h_k Y_k = \sum_{k=1}^{N} \left(\int_{T_0}^{T} c_{p_k} dT + \Delta h_k^0 \right) Y_k = \int_{T_0}^{T} c_p dT + \sum_{k=1}^{N} \Delta h_k^0 Y_k \tag{2.13}$$

, while the total energy in reacting flows is given by $e = h - p/\rho$.

2.2 Chemical kinetics

Chemical kinetics is the study of reaction rates to infer the rate in which reactants are transformed into products in a chemical process [36, 37]. Chemical kinetics includes the study of how different conditions can influence the speed of a chemical reaction and yield information about the mechanism reaction and transition states, as well as the construction of mathematical models that can describe the characteristics of a chemical reaction. More specifically, in reacting flows the chemical kinetics is responsible for determining the rates of heat release $\dot{\omega}_T$ of the chemical process and also dictating the formation of the major combustion products $\dot{\omega}_k$.

The rate of the reaction can be expressed in terms of the concentration of any of the reacting substances or of any reaction product, i.e., the rate may be expressed as the rate of decrease of the concentration of a reactant or the rate of increase of a reaction product [33]. To introduce the main concepts, consider an arbitrary chemical reaction

$$\sum_{k=1}^{N} \nu_k^{'} \Gamma_k \rightleftharpoons \sum_{k=1}^{N} \nu_k^{''} \Gamma_k \tag{2.14}$$

where $\nu_k^{''}$ and $\nu_k^{'}$ are the stoichiometric coefficients of reactants and products of species k, respectively, and Γ_k is the chemical symbol for species k. The phenomenological law of mass action states that the rate of a reaction is proportional to the product of the concentrations of the reactants [4]. For the general reaction given in equation (2.14), the reaction rate is defined as

$$r = K_f(T) \prod_{k=1}^{N} C_k^{\nu_k^{'}} - K_b(T) \prod_{k=1}^{N} C_k^{\nu_k^{''}}, \tag{2.15}$$

where $C_k = \frac{\rho Y_k}{W_k}$ denotes the molar concentration of all species k.

Here it is worth mentioning that the stiffness associated with the prediction of reaction rates creates a central difficulty for computational combustion models. Usually, space and time scales associated with the reaction rates terms are very small, tend to be very smaller than the scales associated with the flow, and requires computational meshes and temporal discretizations which can be orders of magnitude smaller than non-reacting flows [5].

For the chemical species k, the net production rates $\dot{\omega}_k$ is the sum of the reaction rates produced by all M reactions into chemical mechanism

$$\dot{\omega}_k = W_k \sum_{j=1}^{M} \nu_{k,j} r_j \tag{2.16}$$

where $\nu_{k,j} = \nu''_{k,j} - \nu'_{k,j}$.

The proportionality factors $K_f(T)$ and $K_b(T)$ are called the forward and reverse specific reaction rates of the reaction. Here, the reaction rate $K_f(T)$ is determined by Arrhenius law

$$K_f(T) = AT^b e^{-\frac{E}{RT}} \tag{2.17}$$

where A is the pre-exponential Arrhenius factor, b is the temperature exponent, E is the activation energy.

The backwards rate K_b is computed from the forward rate through the equilibrium constant

$$K_b = \frac{K_f}{\left(\frac{p}{RT}\right)^{\sum_{k=1}^{N} \nu_k} \exp\left(\frac{\Delta s}{R} - \frac{\Delta h}{RT}\right)} \tag{2.18}$$

where $P = 1$ bar, and Δs and Δh are the entropy and enthalpy changes occurring when passing from reactants to products in the reaction, respectively. These quantities are obtained from tabulations.

Finally, the heat release due to the chemical process is given by

$$\dot{\omega}_T = -\sum_{k=1}^{N} h_k \dot{\omega}_k \tag{2.19}$$

where h_k is the enthalpy of the chemical species.

2.3 Benchmark Combustion Scenarios

In this section, it is presented benchmark combustion scenarios used to evaluate the role played by chemical kinetics on main physicochemical properties characterizing combustion systems. The scenarios correspond to the application cases of homogeneous combustion during autoignition and flame propagation. More specifically, it is worked on the homogeneous 0-D reactor, the simplest form of a chemical reacting system, where in this scenario all states variables are homogeneously distributed in a control volume, and transient state changes are due to chemical reactions. Also, it is investigated the basic combustion scenario describing a 1-D laminar flame propagating into a premixed gas. Both scenarios are widely used as building blocks of more complex simulations such as turbulent combustion. Here, these two scenarios are employed to evaluate the accuracy and

reliability of chemical mechanisms. More specifically, the aim is to evaluate the impact of using low-fidelity chemical kinetics on combustion systems. Furthermore, it aims to develop embedded-like discrepancy terms to understanding the limits of such low-fidelity models in combustion modeling. That will be more explored in the next chapter.

2.3.1 Zero-dimensional reactor

A zero-dimensional reactor represents the simplest form of a chemically reacting system. It can be viewed as a volume reduced to a single point, such that the combustion is homogeneous in space and only a temporal evolution of the quantities, as shown for the temperature in Fig. 2.2. In this simplified context, the chemical species balance Eq. (2.2), in terms of mass fractions Y_k, of a mixture of N species is reduced to,

$$\frac{\partial Y_k}{\partial t} = \frac{\dot{\omega}_k}{\rho}, \quad k = 1, \cdots, N. \tag{2.20}$$

Assuming the 0-D setting implies that convection and diffusion are neglected, hence, temperature changes occur only due to the energy provided by the combustion of the species. In the constant-pressure case, the internal energy depends only on the temperature and the species mass fractions Y_k. Thus, the energy balance Eq. (2.4) is reduced to

$$\frac{\partial T}{\partial t} = -\frac{1}{\rho c_p} \sum_{k=1}^{N} h_k \dot{\omega}_k. \tag{2.21}$$

The ideal gas state equation provides the density as

$$\rho = \frac{pW}{RT}, \tag{2.22}$$

where W the molar mass of the mixture. Further, the enthalpy h_k of each chemical species k in the gas mixture can be found in the literature, where the standard NASA polynomials [35] data fits are used to compute this quantity.

In a homogeneous 0-D reactor simulation, the auto-ignition delay time is an important quantity of interest. Ignition delay times are substantially mostly kinetically controlled, thus they can be used to validate or calibrate chemical mechanisms. More specifically, the autoignition delay time is the period necessary to the preheated mixture achieves the reaction zone, wherein the combustion reactions occur, as shown in Fig. 2.2.

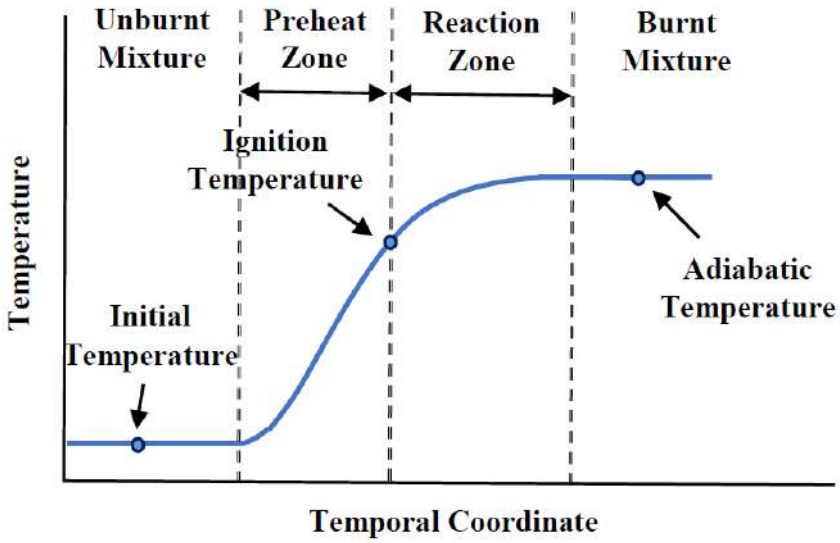

Figure 2.2: Overview of temperature evolution in a 0D-reactor.

2.3.2 One-dimensional laminar premixed flame

The hypothesis of a freely laminar propagation, i.e., the flame is contained in an infinite domain with zero gradients of state variables (velocity, temperature and mass fractions) at either end [38], allows to assume the problem as a one-dimensional confined flame propagating the combustion towards the non-burnt mixture and achieving a steady state [4, 5, 38, 39]. The laminar premixed flame calculation is based on the solution of a freely propagating laminar flame in adiabatic conditions. So, the governing equations for reaction flows can be simplified as follows

$$\frac{\partial \rho}{\partial t} + \frac{\partial \rho v}{\partial x} = 0 \tag{2.23}$$

$$\frac{\partial \rho Y_k}{\partial t} + \frac{\partial}{\partial x}(\rho(v + V_k)Y_k) = \dot{\omega}_k \quad k = 1, \ldots, N \tag{2.24}$$

$$\rho c_p \left(\frac{\partial T}{\partial t} + v \frac{\partial T}{\partial x} \right) = \dot{\omega}_T + \frac{\partial}{\partial x} \left(\lambda \frac{\partial T}{\partial x} \right) - \rho \frac{\partial T}{\partial x} \left(\sum_{k=1}^{N} c_{p,k} Y_k V_k \right) \tag{2.25}$$

These governing equations describe a flame propagating from the burnt to the unburnt gas at a speed that reaches a constant value s_L when transients are ignored.

Note that the momentum conservation equation (2.3) is not necessary anymore when the flame reaches the steady-state, the conservation equations can be written in the reference frame of a flame moving at a constant speed s_L. Therefore,

$$\rho v = \rho_0 s_L \tag{2.26}$$

where ρ_0 is the non-burnt density mixture.

The boundary conditions for this scenario in the unburnt mixture are

$$T(-\infty) = T_u, \tag{2.27}$$

$$Y_k(-\infty) = M_k(\phi), \quad k = 1, \cdots, N, \tag{2.28}$$

where T_u is the non-burnt mixture temperature and $M_k(\phi)$ is the known incoming mass fraction of the k-th species in function of the equivalence ratio ϕ. In the burnt mixture, the boundaries conditions are

$$\frac{dT}{dx}(+\infty) = 0, \tag{2.29}$$

$$\frac{dY_k}{dx}(+\infty) = 0, , \quad k = 1, \cdots, N. \tag{2.30}$$

Also, in a freely propagating flame, the mass flow rate $\dot{M}$ is not known, it is an eigenvalue to be determined. The flow rate is calculated by introducing the trivial differential equation,

$$\frac{d\dot{M}}{dx} = 0, \tag{2.31}$$

and an additional boundary condition to the scenario. The extra boundary condition is chosen arbitrarily. However, it must be chosen to ensure that the spatial gradients of the state variables vanishing at either end. Typically, the temperature at one additional point is imposed, wherein a natural choice is to impose the temperature at the origin $x = 0$,

$$T(0) = T_i \tag{2.32}$$

which also removes the translational invariance of the problem [38].

The problem set-up is closed if a chemical model is given and if proper boundary conditions are provided. Here, the flame is considered an ideal gas mixture with pressure assumed as constant and with a non-unity Lewis number ($Le \neq 1$). The Lewis number compares the diffusion speeds of heat and species k. It is used to characterize fluid flows where there is simultaneous heat and mass transfer [5]. The Lewis number is defined as $Le_k = \lambda/\rho c_p D_k$.

In the present work, this problem is solved using the Cantera software [40] with the possibility to choose different chemistry mechanisms to close the mathematical problem. Here, the goal is to predict key quantities of interest of the flame such as laminar flame speed s_L, i.e, the speed at which the flame front is moving with respect to the fresh gases in a one-dimensional geometry, adiabatic flame temperature, burnt molar/mass fractions and flame thickness. The flame thickness is an important property of numerical combustion problems because this thickness controls the

required mesh resolution. In most combustion approaches, the flame structure must be resolved and enough points must be localized within the flame thickness [5].

Chapter 3

Model Calibration

Typically, weak points in the modeling of reaction flows, as in many other physics based computational models, are associated with the closure equations. That is, for instance, the case of turbulent combustion simulation [8, 41] in which mass, momentum and energy balance, and species transport equations are combined with reaction mechanisms, being those derived, often, by experts and a limited number of experiments. Such construction of the closure reaction mechanisms leads to uncertainties for the modeling. On one side, due to the estimation of parameters, impacted by noise and indirect measurements. In addition, model discrepancies (also referred to as model errors or structural errors) resulting from employing simplified physics or chemistry, motivated by the need for seeking a balance between easiness of computation and accuracy, tend to be more difficult to handle. Specifically, simplified chemistry or reduced chemical models are reaction models that always contain fewer reactions, and usually, the number of species included in the reduced model is smaller than the detailed models. Being the detailed mechanisms those with large numbers of reactions describing complex chemical systems with reliable accuracy. Also, reduced chemical models can be seen as subsets of the species and reactions from the detailed model.

This chapter provides an overview of the calibration approach employed to account model discrepancies via probabilistic embedding within the model. Also, an embedded deep learning model discrepancy approach is proposed. More specifically, a deep neural network is embedded as an additive function to model the temporal evolution of chemical species concentrations that serves as a source to the flow field. Here, it is followed a traditional route in physics-based models, wherein the closure models are calibrated in the simplest scenario and validated in a more complex one. More specifically, in traditional combustion modeling, the chemical kinetics model is calibrated in the 0D homogeneous scenario and extrapolated to a more complex and challenging simulations such as the 1D laminar flame scenario. Consequently, this chapter depicts an overview of the model discrepancy approaches used to improve

the ability to predict key QoI's in computational combustion models, from low to high fidelity chemical models. An overview of surrogate modeling construction using deep neural network is described in the last section.

3.1 Model Discrepancy Approaches

Model calibration has a central role on the development of computer models and consists on using data from field and experimental observations, or even from simulations based on higher fidelity models, to tune lower fidelity models, learn about parameters and identify sources of uncertainty. In the past years, Bayesian inference has been widely used to model model inadequacy [24–26]. This approach is considered a strong framework for combining previous knowledge and experimental data to developed chemical models, as well as quantify the associated uncertainties due to structural deficiencies of the model [1]. Also, machine learning and artificial intelligence techniques can be used to characterize the error inherent to the use of low-fidelity physics-based models. More specifically, neural network architectures can be constructed to characterize the discrepancy term due to the use of limited physics and be embedded in the computational model [42], allowing to improve the predictability of low fidelity models as well as to quantify uncertainties in the predictions due to the use of such models. Both approaches are pursued in the next subsections.

3.1.1 A probabilistic approach

Now, a Bayesian embedded discrepancy approach is employed to enhance the predictive ability of the final modal and understanding the limits of using reduced chemical models. Here, the description of this strategy follows the article published in [43] by me and co-authors Prof. Fernando A. Rochinha, Prof. Xi Jiang (Queen Mary-University of London), and Dr. Daniel Mira (Barcelona Supercomputing Center). This approach provides a way to reduce systematically the cost of chemical kinetics in simulations while quantifying the accuracy of predictions of key QoI's.

As a starting point, it is worth highlighting a pioneer seminal approach proposed by Kennedy and O'Hagan (KO) [44]. They introduced a Bayesian approach for parameter calibration taking into account model discrepancies. It is built upon an observation equation considering the model discrepancy bias through an additive term, expressed as,

$$\mathbf{z} = G(\mathbf{s}) + \mathbf{e} = f(\mathbf{s}, \boldsymbol{\theta}) + \epsilon(\mathbf{s}) + \mathbf{e}, \tag{3.1}$$

where $\mathbf{z}$ is a vector of observable outputs, $\mathbf{s}$ is a vector containing input variables

that define a scenario S (e.g., boundary and initial conditions, geometry, material properties), $G(\mathbf{s})$ represents the physical truth, and $\mathbf{e}$ is the observation noise. The dependence on state variables is omitted to keep the notation simple. Moreover, $f(\mathbf{s}, \boldsymbol{\theta})$ is a short notation for the model, which is a function of the input variable $\mathbf{s}$ and parameters to be calibrated $\boldsymbol{\theta}$, and $\epsilon(\mathbf{s})$ denotes the model discrepancy assumed as a Gaussian vector or process. However, the KO approach carries a number of challenges [27]. First, the imposition of a statistical structure for model discrepancy $\epsilon(\mathbf{s})$ can lead to violation of physical constraints, particularly when considering physics-based models. Another challenge, is that this approach provides a model discrepancy correction to specific cases only. In the case of physical system models intended for predicting numerous quantities of interest, there is no provision for an associated discrepancy correction.

Instead of dealing with these difficulties, a calibration approach [27] that accounts for model discrepancy via probabilistic embedding within the model is investigated here. In particular, the model error is embedded in the key parameters of the model $f(\mathbf{s}, \boldsymbol{\theta}(\boldsymbol{\alpha}))$. More specifically, the model discrepancy is embedded in the Arrhenius (kinetic) parameters of the reduced chemical model, since these parameters play an essential role in the computing of the net production rates of species, as well as the heat release in the chemical process [15]. Thus, $\boldsymbol{\theta}$ is a random vector with a Probability Distribution Function (PDF) depending on the hyper-parameters $\boldsymbol{\alpha}$ that one wishes to learn from Bayesian inference. An advantage of this approach is that since the error is now embedded in the model parameters, it can easily be propagated through the computer model to get the related uncertainty on any quantity of interest impacted by the model parameters.

In this context, given the data D, the calibration builds on the following expression derived from Bayes's formula [45, 46],

$$\underbrace{p(\boldsymbol{\alpha}|D)}_{\text{posterior}} \propto \underbrace{p(D|\boldsymbol{\alpha})}_{\text{likelihood}} \underbrace{p(\boldsymbol{\alpha})}_{\text{prior}} \tag{3.2}$$

where $\boldsymbol{\alpha}$ is the vector of hyper-parameters to be identified, describing the inputs $\boldsymbol{\theta}$ as random variables.

The prior $p(\boldsymbol{\alpha})$ is chosen to encode accumulated knowledge about the model parameters. Prior selection is a challenge for any Bayesian method. In this context, $p(\boldsymbol{\alpha})$ can be selected according to some physical considerations, e.g., expert knowledge, or as a result of a previous calibration. An additional difficulty arises from the fact that $\boldsymbol{\alpha}$ are not physical model parameters, but rather parameters that define the discrepancy term. Furthermore, prior selection offers several opportunities for imposing specific constraints or regularization. It is important to choose appropriate priors that capture the initial knowledge on $\boldsymbol{\alpha}$ before any

observational or simulation data is available. In this work, the priors are strictly uniform, potentially with physics-based support constraints.

As the model discrepancy are embedded in the parameters $\boldsymbol{\theta}$, It is followed the approach adopted in [47] which the model parameters are expanded using a first-order Gauss-Hermite Polynomial Chaos Expansion (PCE) [48]. Thus, a multivariate normal distribution for $\boldsymbol{\theta}$ is adopted, that is,

$$\begin{aligned}
\theta_0 &= \alpha_{00} + \alpha_{01}\xi_1 \\
\theta_1 &= \alpha_{10} + \alpha_{11}\xi_1 + \alpha_{12}\xi_2 \\
&\vdots \\
\theta_i &= \alpha_{i0} + \alpha_{i1}\xi_1 + \alpha_{i2}\xi_2 + \cdots + \alpha_{ii}\xi_i
\end{aligned} \tag{3.3}$$

Here ξ_i are independent and identically distributed (i.i.d.) standard normal random variables and α_{ij} are the components of the vector of hyper-parameters to be inferred. It is worth highlighting that for a fixed sample of the hyper-parameters, $\boldsymbol{\theta}$ is a stochastic vector characterized by the hyper-parameters and the random vector $\boldsymbol{\xi}$. Thus, the model discrepancy is characterized by a random variable.

The likelihood function $p(D|\boldsymbol{\alpha})$ connects the parameters and the data through the computer model. The construction of an appropriate likelihood is therefore a crucial component of the present approach [27]. The full likelihood, consistent with the observation, is computed by integrating $\boldsymbol{\theta}$,

$$p(D|\boldsymbol{\alpha}) = \int_{-\infty}^{+\infty} p(D|\boldsymbol{\theta})p(\boldsymbol{\theta}|\boldsymbol{\alpha})d\boldsymbol{\theta}. \tag{3.4}$$

The equation above is computationally demanding, even in the case in which $p(D|\boldsymbol{\theta})$ is a Dirac-function as the original model is deterministic, for the noiseless case ($\mathbf{e} = 0$) [49]. For each value of $\boldsymbol{\theta}$, there is a set of differential equations to be solved. Also, in the noiseless case, equation (3.4) tends to be degenerate [27]. Hence, the construction of a justifiable likelihood is perhaps the most critical step for obtaining the posterior probability distribution. In the present work, it is assumed an Approximate Bayesian Computation (ABC) method. This method is useful when a proper likelihood is not known or is prohibitively expensive to evaluate [27].

The ABC method a pseudo-likelihood PDF that have as a goal to minimize the distance between the computer model mean $\mu_i(\boldsymbol{\alpha})$ and the data D_i for each data point i, and requires that the standard deviation $\sigma_i(\boldsymbol{\alpha})$ of the model predictions f_i to be consistent with the data spread around the mean model prediction, implying

the likelihood form

$$\mathfrak{L}(D|\boldsymbol{\alpha}) = \frac{1}{\lambda\sqrt{2\pi}} \prod_{i=1}^{N} exp\left(\frac{(\mu_i(\boldsymbol{\alpha}) - D_i)^2 + (\sigma_i(\boldsymbol{\alpha}) - |\mu_i(\boldsymbol{\alpha}) - D_i|)^2}{2\lambda^2} \right). \tag{3.5}$$

Here, λ is the tolerance parameter, which controls the width the likelihood type [27]. The mean $\mu_i(\boldsymbol{\alpha})$ and standard deviation $\sigma_i(\boldsymbol{\alpha})$ have to be estimated at each data point i to compute the likelihood. To alleviate the computational burden in predict the statistics, polynomial chaos expansions are used to efficiently compute $\mu_i(\boldsymbol{\alpha})$ and $\sigma_i(\boldsymbol{\alpha})$.

The posterior $p(\boldsymbol{\alpha}|D)$ represents the degree of belief about model parameters after the data D is incorporated. The posterior distribution is complex, and we can not derive analytical expressions for it. Therefore, it is needed to resort to numerical schemes to generate samples that characterize the probabilistic structure of $\boldsymbol{\alpha}$ and, indirectly, of $\boldsymbol{\theta}$. Thus, the posterior distribution, conditioned on the data, of any quantities of interest (QoIs) q is formally obtained integrating out the hyper-parameters after the calibration through,

$$p(q|D) = \int_{\boldsymbol{\theta}(\boldsymbol{\alpha})} p(q|\boldsymbol{\alpha}) p(\boldsymbol{\alpha}|D) d\boldsymbol{\theta} \tag{3.6}$$

where $p(q|\boldsymbol{\alpha})$ is the multivariate PDF induced by the computer model $f(\hat{\mathbf{s}}, \boldsymbol{\theta}(\boldsymbol{\alpha}))$. The notation $\hat{\boldsymbol{s}}$ refers to the possibility of computing the QoIs for different scenarios. Indeed, the aims of calibration and validation are to enhance the predictability of the computer model scenarios where observed data is not available.

Here, the posterior distribution is characterized by sampling using Markov chain Monte Carlo (MCMC) methods [50–52]. Another common technique used to characterize the posterior is the maximum a posteriori (MAP) value, which can either be extracted from the full MCMC procedure, or computed via optimization techniques [53, 54], that is, taking

$$\alpha_{MAP} = \text{argmax } p(\boldsymbol{\alpha}|D). \tag{3.7}$$

3.1.2 A deterministic approach; neural network model discrepancy

The objective of this section is to propose an alternative for the embedded model discrepancy. The main idea is to combine the stochastic operator source term approach proposed by [13, 23] to represent model inadequacy with machine learning tools [2, 55–59, 59] to construct and train an embedded model discrepancy term.

In the model discrepancy approach [13], a stochastic operator representing the

model error is embedded as a source term in the model equations

$$\mathbf{z} = G(\mathbf{s}) + \mathbf{e} = f(\boldsymbol{\theta}, \mathbf{s}) + \boldsymbol{\epsilon}(\boldsymbol{\theta}, \mathbf{s}) + \mathbf{e} \tag{3.8}$$

where $\boldsymbol{\theta}$ is a vector containing the model parameters, and $\mathbf{s}$ is the vector of input variables defining a scenario S, and $\boldsymbol{\epsilon}(\boldsymbol{\theta}, \mathbf{s}))$ denotes the stochastic operator representing the model discrepancy.

This approach has been applied with reliable predictions in dynamic systems [13, 23]. However, this model error approach has some difficulties. Firstly, defining a mathematical structure, respecting physical constraints, for the stochastic operator can be extremely challenging. Moreover, the stochastic operator can be composed of a large number of parameters to be learned, which needs a large dataset in the calibration process. Also, constructing reliable priors for such parameters can be a challenge. As the model error is embedded within the model equations, it can be impracticable to extrapolate the model discrepancy for a different scenario, i.e., a scenario different from which it was learned.

Instead of dealing with the highlighted difficulties, it is proposed an alternative for the embedded model discrepancy [13]. Here, the model error is embedded as a source term in the flow field. More specifically, a source term is embedded as an additive function to model the temporal evolution of chemical species concentrations $\dot{\omega}_k$. These concentrations act as source terms in the benchmark combustion scenarios through the mass species conservation equations (2.20) and (2.24), as well as the energy balance equations (2.21) and (2.25). Hence, the model error is embedded as a source term as follows,

$$\mathbf{z} = f(\mathbf{s}, \boldsymbol{\theta}, \kappa(\boldsymbol{\epsilon})) + \mathbf{e}. \tag{3.9}$$

where κ represents the closure models.

In order to make the idea more clear, the 0D scenario is retrieved and a specific form of the above formal abstract mathematical representations is detailed. In such scenario, the state variables are reduced to $\mathbf{Y}(t)$ (a vector containing as components the fractional volumes of each species) and the temperature $T(t)$. The resulting nonlinear governing equations are replicated for the sake of clarity below,

$$\begin{aligned} \frac{d\mathbf{Y}}{dt} &= \frac{1}{\rho(T)} \overbrace{(\boldsymbol{\omega}(\mathbf{Y}, T) + \boldsymbol{\epsilon}(\mathbf{Y}, T; \mathbf{w}))}^{\underline{\boldsymbol{\omega}}(\mathbf{Y}, T; \mathbf{w})} \\ \frac{dT}{dt} &= \frac{-\mathbf{h}(T) \cdot \underline{\boldsymbol{\omega}}(\mathbf{Y}, T; \mathbf{w})}{\rho(T) c_p(T)} \end{aligned} \tag{3.10}$$

where the discrepancy is embedded to correct the energy released by the combustion

of species into the system. In that case, even if the amount of each species is not correct due to the use of a reduced kinetics, the calibrated model can make reliable predictions about the temperature in the 0D scenario.

Since the model discrepancy is embedded in the reduced kinetics model, such framework naturally allows consistency with the underlying model physics, even beyond the 0D scenario detailed below. Here, to better illustrate the extrapolation of such approach in a more complex scenario the chemical species conservation equation (2.24) for 1D scenario is shown:

$$\frac{\partial \rho \mathbf{Y}}{\partial t} + \frac{\partial}{\partial x}(\rho(v + \mathbf{V})\mathbf{Y}) = \underline{\boldsymbol{\omega}}(\mathbf{Y}, T; \mathbf{w}) \tag{3.11}$$

where $\underline{\boldsymbol{\omega}}$ is a vector containing the species enhanced production rates.

A critical issue involving modeling the discrepancy term relies on assuming its mathematical structure. In many complex dynamical systems, although data can be abundant a formal mathematical structure for the governing equations remain unrecognized. In recent years, machine learning has become an important research area that allows integrating principles from physics to discovery a mathematical structure of the governing equations [60–62]. It is noteworthy that, neural networks have been widely used to model closure relations in many practical problems arising from a variety of scientific and engineering applications [63–70]. Here, a fully connected neural network (FCNN) [59] is assumed to capture an appropriate functional form for the model correction. FCNNs have the ability, from given the data (provided by experiments or a high fidelity model), to decode and detect patterns and intrinsic correlations inherent to such term. Moreover, this approach avoids the difficulties relied on assuming a mathematical structure for the model error term.

Deep neural networks (DNNs) are simply networks with multiple intermediate hidden layers, and FCNNs are a particular form of a DNN [59]. The input-output relationship $\eta : \mathbf{x} \to \mathbf{y}$, vectors in $\mathbb{R}^n$, is approximated through a sequential hierarchy involving layers that are combinations of a set of neurons. The sizes of the input and output layers are fixed and determined by the dimensionality of the input and output. Figure 3.1a illustrates a neural network with two hidden layers. Each neuron accepts one or more inputs and produces an output by performing a nonlinear transformation. Figure 3.1b shows a schematic of a single neuron. Thus, the l-th layer output of the network is given as follows

$$\mathbf{x}^l = \sigma(\mathbf{W}^l \mathbf{x}^{l-1} + \mathbf{b}^l), \quad \forall\, l \in \{1, \ldots, L\} \tag{3.12}$$

where $\sigma(\cdot)$ is the activation function, usually nonlinear. $\mathbf{W}^l \in \mathbb{R}^{d_l d_{l-1}}$ is the weight matrix, where d_l is the number of neurons, in the l-th layer, $\mathbf{b}^l$ is the bias vector and

L is the number of layers in the network. Finally, $\mathbf{x}^0$ represents the network input.

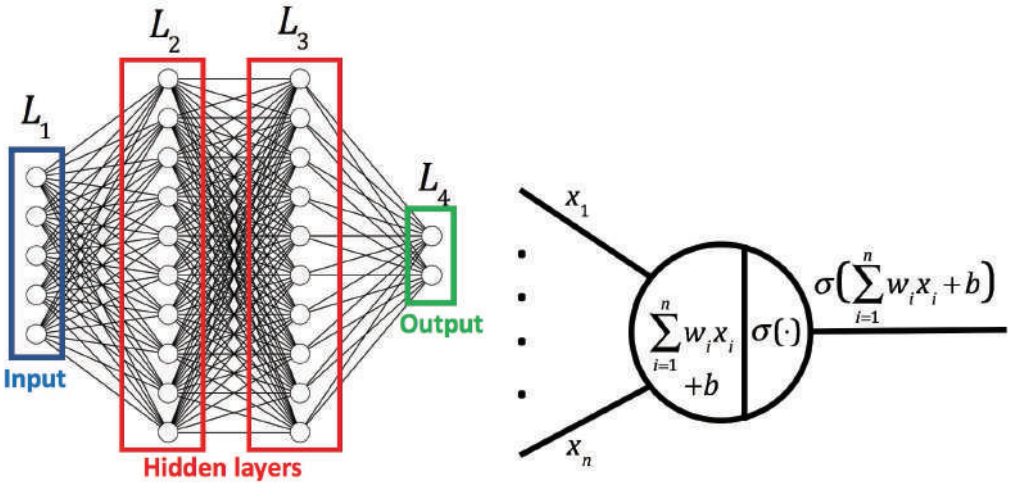

(a) (b)

Figure 3.1: (a) Neural network structure. (b) Schematic of a single neuron. [2]

Therefore, the discrepancy term can be written in a compact form as

$$\boldsymbol{\epsilon} = \mathbf{f}(\mathbf{Y}, T; \mathbf{w}) \tag{3.13}$$

where $\mathbf{f}(\mathbf{Y}, T; \mathbf{w})$ is the output of the neural network, and $\mathbf{w}$ is the vector of parameters of the fully connected neural network. Here, it is worth highlighting that all network parameters are constant in time. Hence, the time-dependence of the model discrepancy is only due to the state variables. Also, the neural network is implemented in the open source machine learning platform Tensorflow [71].

Since reliable data that represent values for the model error is extremely difficult to define, the available data for training are quantities of interest characterizing the combustion scenarios provided by numerical simulations of high-fidelity chemical models. Here, the Cantera software is employed to generate the training dataset.

Chapter 4

Results and Discussion

This chapter presents the main results of the thesis. Preliminary, section 4.1 provides a comparison between predictions carried out with detailed and reduced mechanisms, in the basic scenarios of Chapter 2. Section 4.2 describes the learning approach to calibrate the reduced mechanism that accounts for model discrepancy via probabilistic embedding. Also, it is presented in section 4.2.3 the results of the surrogate model for uncertainty quantification constructed using deep neural networks, extrapolating the analysis to broader operating conditions. Finally, the results of the embedded deep learning discrepancy model approach are shown in section 4.3.

In order to be more clear, here it is proposed different forms of embedding the model discrepancy. In section 4.2, a model in which the model discrepancy is embedded in the chemical kinetics parameters is proposed. Also, a second model similar to the previous one with a pre-exponential adjustment factor that redefines the reaction rates as a function of the equivalence ratio is proposed to recovery the flame characteristics in rich conditions. In section 4.3, a model in which the model discrepancy is embedded as an additive term in the temporal evolution of chemical species concentrations is proposed. Furthermore, it is proposed that the embedded discrepancy model is reformulated as a multiplying factor in the net production rates of species. Finally, it is constructed a embedded discrepancy that acts as a correction term in the chemical kinetics parameters similar to what is shown section 4.2. However, a neural network is built to capture an appropriate functional form of the model correction.

4.1 Comparison between detailed and reduced mechanisms

An accurate description of biogas-air combustion requires a detailed chemical mechanism accounting for all relevant elementary reaction steps and intermediates. A widely accepted model for the combustion of biogas is the detailed GRI3.0 mechanism [72], analysed in detail, with specific intent of proving its reasonability for this application in [19, 73]. It consists of 325 elementary reactions and encompasses 53 species which accounts for the mass balance of H_2, CO, CH_4, N_2 and includes C_1-C_2 hydrocarbons, being those species containing one and two carbon atoms, respectively.

Typically, to alleviate the high computational cost of the simulations, reduced reaction mechanisms are employed. The results in Appendix A suggest that the use of reduced schemes for methane/air oxidation would be a good starting point to develop optimized schemes for biogas, as the variations in fundamental flame parameters due to composition variations are relatively small and could be captured by the same schemes. That influence of composition variations in physicochemical properties of combustion is further confirmed in [74].

For the present purpose, it is employed a reduced mechanism based on 2-step chemistry that has been widely used in the literature, also referred to as 2S-CM2 [31, 34, 75, 76]. This reduced scheme serves as proxy of more detailed kinetic models and is calibrated against the mechanism GRI3.0. The 2-step 2S-CM2 mechanism consists of 6 species with 2 global reactions:

$$CH_4 + \frac{3}{2}O_2 \Rightarrow CO + 2H_2O \tag{4.1}$$

$$CO + \frac{1}{2}O_2 \iff CO_2. \tag{4.2}$$

These two mechanisms are employed in basic scenarios, which consists of a zero-dimensional reactor (section 2.3.1) and a laminar premixed flame (section 2.3.2).

Biogas is mainly composed of methane (CH_4) and carbon dioxide (CO_2), with smaller amounts of oxygen, nitrogen and volatile organic compounds. In the present work, the biogas mixtures are composed only by methane and carbon dioxide, as shown in Table 4.1. Note that the baseline fuel is simply methane, a well-known fuel whose utilization characteristics are well-studied [12, 34]. Therefore, biogas fuels can be compared directly to methane in combustion analyses.

Table 4.1: Biogas composition.

Biogas (Volume %)	CH_4	CO_2
Baseline	100	0
BG1	75	25
BG2	50	50

4.1.1 Ignition delay time

Here, the ignition delay time for the 0D scenario is estimated when a maximum temperature gradient occurs,

$$\tau = \text{MAX}\left(\frac{\partial T}{\partial t}\right). \tag{4.3}$$

The ignition delay is computed using the detailed and reduced mechanisms for biogas-air mixtures of Table 4.1 at different initial temperatures $T_0 \in [1000, 1300K]$ and equivalent ratios $\phi \in [0.6, 1.4]$. They are presented in Figure 4.1. The equivalent ratio is a central parameter in combustion process. Rich mixtures are characterized by $\phi > 1$ (fuel is in excess), while lean regimes are achieved for $\phi < 1$ (oxidizer is in excess).

During autoignition, there is a complex balance of chemical reactions that results in certain delay to achieve chemical equilibrium. This is fundamentally a chemical problem as convection and diffusion are not accounted for. In fact, considering this 2-step model for autoignition reveals an important disagreement, as shown in Fig. 4.1, when compared with the full GRI3.0 mechanism, for the prediction of the autoignition delay time. The results show the autoignition delay time at different initial temperatures and compositions for the considered fuel mixtures of Tab. 4.1.

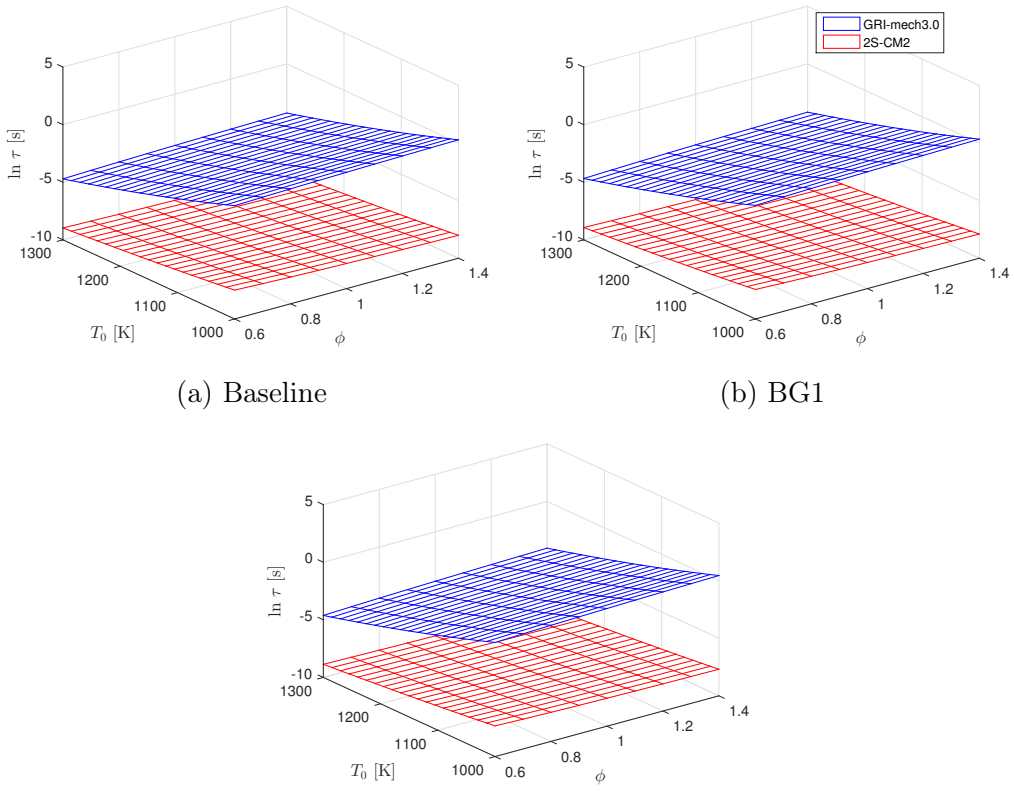

(a) Baseline

(b) BG1

(c) BG2

Figure 4.1: Ignition delay times over a range of T_0 and ϕ.

4.1.2 Laminar premixed flame

One-dimensional laminar premixed flames can be used for better understanding and advanced modeling of the combustion phenomena, such as the flamelet turbulent model [77, 78], in real applications. Thus, accurately predictions of the flame proprieties of biogas-air mixtures for various equivalent ratios are very important. Figures 4.2 and 4.3 show the difference between the flame physicochemical properties computed by GRI3.0 and 2S-CM2 mechanisms for the BG1-air mixture, over a range of stoichiometric conditions $\phi \in [0.6, 1.4]$ at $T_0 = 300$ K and $P = 1$ bar.

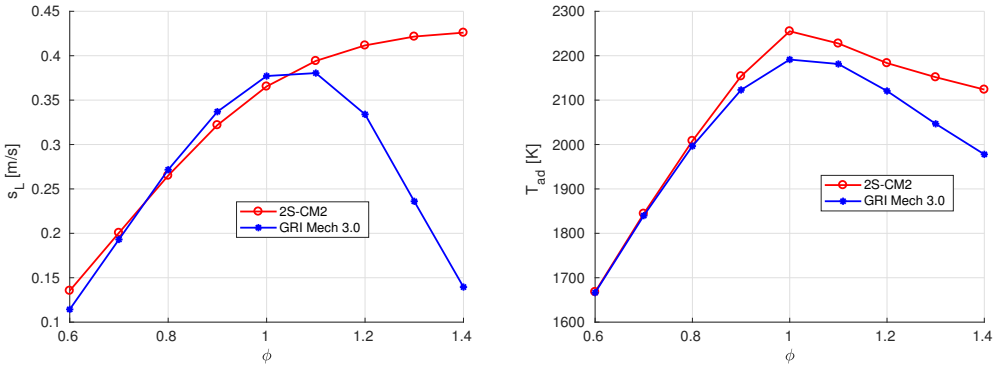

(a) Baseline flame speed

(b) Baseline adiabatic temperature

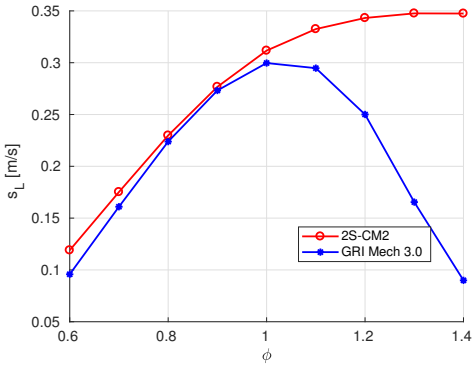

(c) BG1 flame speed

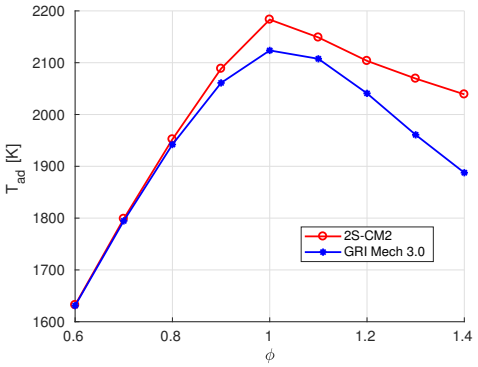

(d) BG1 adiabatic temperature

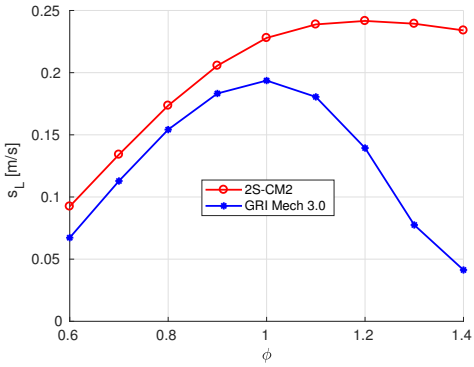

(e) BG2 flame speed

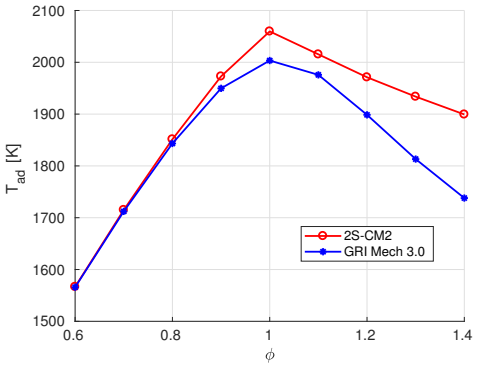

(f) BG2 adiabatic temperature

Figure 4.2: Flame speed and adiabatic temperature conditioned to the equivalence ratio at p = 1 bar and T_0 = 300 K.

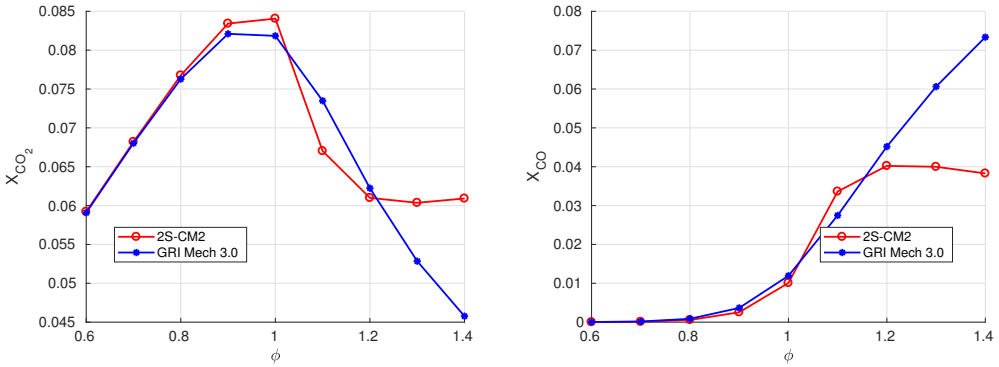

(a) Baseline CO_2 molar fraction

(b) Baseline CO molar fraction

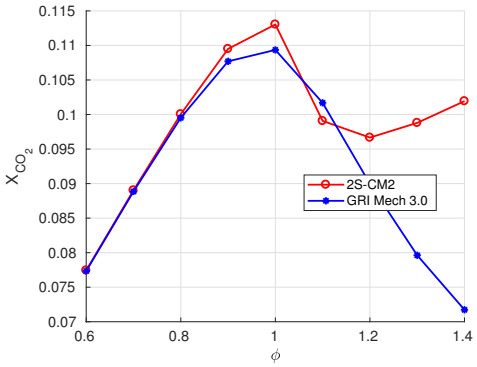

(c) BG1 CO_2 molar fraction

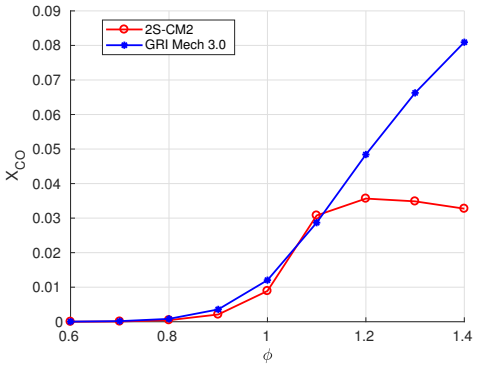

(d) BG1 CO molar fraction

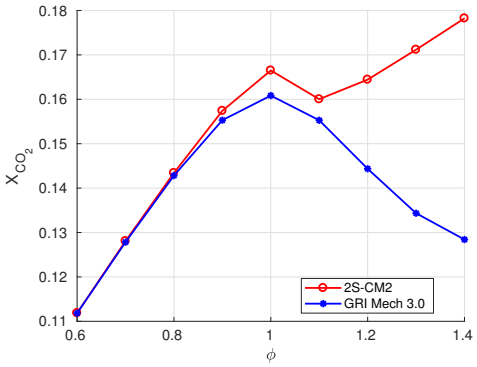

(e) BG2 CO_2 molar fraction

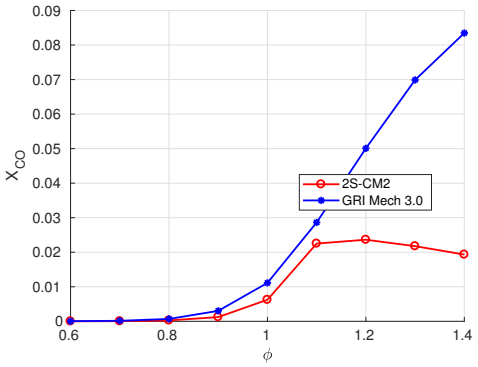

(f) BG2 CO molar fraction

Figure 4.3: Burned mole fractions dependence on the equivalent ratio for a premixed flame at p = 1 bar and T_0 = 300 K.

It is observed good predictions of the reduced scheme compared to the full GRI3.0 in lean conditions, while the performance in rich flames is far from satisfactory as the mechanism has not been designed to operate in this regime. This is consistent with other studies employing this reduced chemical kinetic mechanism for methane combustion, and corrections of the kinetics parameters using empirical adjustments are made to improve the predictions in this range [31, 34, 76]. Also, it can be noted that when the biogas composition has a large amount of CO_2, as in BG2, the discrepancy caused by the reduced mechanisms increases. These result suggests

that the reduced mechanism might be initially developed for lean conditions during stable burning and dilution.

In the next section, a Bayesian approach to understanding the limits of employing a reduced mechanism for methane/air in this renewable fuel is presented and also to improve the ability of the reduced model to predict key QoIs of the benchmark combustion scenarios.

4.2 A Bayesian Embedded Approach

From the results shown in section 4.1, it can be noted that the physicochemical properties predicted by the reduced mechanism presents an unsatisfactory agreement leading to a detectable inconsistency in biogas combustion. Therefore, the use of reduced mechanisms needs to be taken with care, as these mechanisms are usually calibrated to match certain properties for a given operation range, but they might lead to significant errors when used outside their application range. A possible approach to address this problem would be to either consider an extended mechanism with the increase in computational cost during CFD simulations, or to provide a calibration approach of the Arrhenius parameters to account for these effects.

In this context, enhancing the predictive ability of the computational models through UQ can be used to extend the applicability of reduced schemes to wider operating conditions as an robust alternative to empirical models. Here, the preliminary steps of statistical calibration [27, 47] assessing if the Arrhenius parameters are suitable for embedding the model discrepancy is followed. For modelling the combustion chemistry of renewable biogas, it is necessary to consider both the detailed model to provide data and a reference, that capture the key features of biogas chemical reactions [19, 73], and a simplified model. At this point, it is important to highlight that simplified methane models with standard Arrhenius parameters have been tested before for biogas/methane combustion with no success for certain conditions [31, 34, 76, 79]. Here, the intention is to achieve a better performance through the embedding formulation, at least for laminar flames. This approach is explored in the following sub-sections.

In order to investigate the impact of model discrepancies due to the use of a reduced mechanism to compute the combustion properties, it is applied a Bayesian calibration to handle the model discrepancy. To make sure that the mismatch of predictions with the calibrated model is due to the use of reduced chemistry, instead of using experimental data, high-fidelity computational simulations with the GRI3.0 detailed mechanism are employed. Besides, that provides more flexibility in the analysis. As it becomes a model-to-model calibration, it is assumed that the data represent the "truth" without any additive noise. The reference data for calibration

are data taken from the oxidation process of constant pressure reactors to conduct autoignition delay tests. The reduced mechanism is supposed to provide satisfactory rates for lean premixed combustion, but not for autoignition. As shown in Fig. 4.1, the autoignition delay times of the mixtures of the Table 4.1 have small deviations between them. Thus, it is chosen as data the autoignition delay time for the BG1 mixture at atmospheric pressure, over a range of equivalent ratio $\phi \in [0.6, 1.4]$ and a range of initial temperature $T_0 \in [1000, 1300K]$ varying by 0.1 and 15K, respectively. Therefore, the reference data for calibration are composed by 189 autoignition delay times of biogas/air.

4.2.1 First Calibration Experiment

To investigate the limits of the 2S-CM2 mechanism, the probabilistic embedding approach [27] is employed. The irreversible reaction in the 2S-CM2 scheme is the most relevant regarding the autoignition delay time and flame speed [80]. Thus, it is taken the pre-exponential factor and activation energy of this reaction as the uncertainty (to be identified). Here, the following models for the activation energy and logarithm of the pre-exponential factor are chosen

$$\begin{aligned} E &= \theta_0 \\ lnA &= \theta_1 \end{aligned} \tag{4.4}$$

where θ_i are the model parameters that we want to learn using Bayesian Inference.

Here, $\boldsymbol{\theta}$ is adopted as in equation (3.3). For the prior, recall that the α_{ij} are i.i.d uniform priors with large boundaries, i.e. noninformative priors, where the starting points of α_{00} and α_{10} are the nominal values of the activation energy and the pre-exponential factor, respectively [34]. Lastly, $\alpha_{1j} \geqslant 0$, for $1 \leqslant j \leqslant 2$, in order to avoid the sign-flip invariance [27].

In the calibration process, it is adopted the ABC likelihood (3.5). The tolerance parameter ϵ, which acts as a penalty parameter of the likelihood, is assumed equal to 0.1 [27]. The Chaospy toolbox [81] is used for performing uncertainty quantification using polynomial chaos expansions, leading to efficient computation of $\mu_i(\alpha)$ and $\sigma_i(\alpha)$ at each data point i. Also, the algorithm used here to sample from the posterior distribution (3.2) is Metropolis-Hastings MCMC algorithm [53].

A total of 20,000 parameter samples are obtained using MCMC in this study. Figure 4.4 illustrates the structure of 1D and 2D marginal PDFs of the parameters α_{ij}. It can be noted that the parameters exhibit stronger non-Gaussian trends. Observe the strong correlation between the parameters α_{00} and α_{10}. These parameters can be view as the expected values of the activation energy and the

pre-exponential factor, respectively. Furthermore, it is verified that the PDFs of such parameters present values higher than the nominal values [34]. Hence, the rate in which the irreversible reaction occurs and the amount of CO and H_2O formed in the combustion process increase.

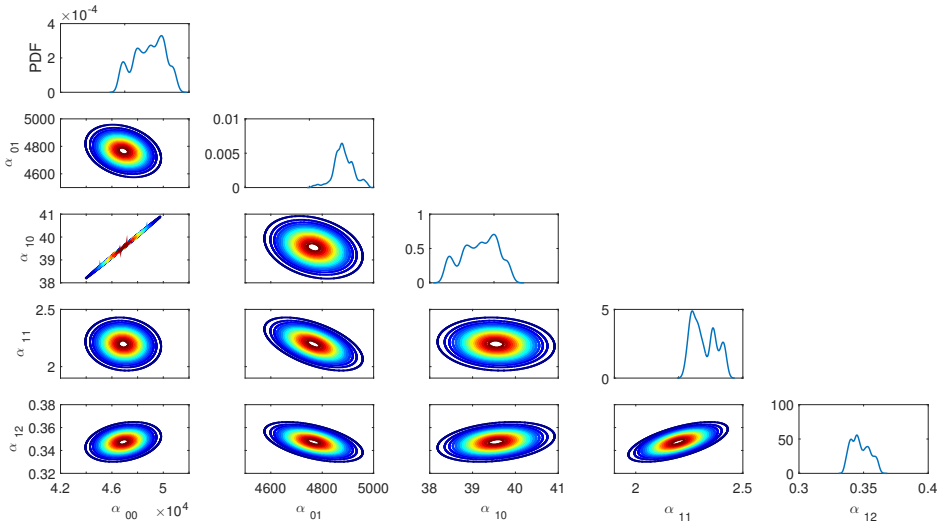

Figure 4.4: 1D and 2D marginal PDFs of the parameters α_{ij}.

Using the PDF of vector $\boldsymbol{\alpha}$, it can be computed the realizations of lnA and E, i.e. the push-forward of $p(\boldsymbol{\alpha}|D)$ through the model. Here, it is taken 10,000 samples of $\boldsymbol{\alpha}$ and, for each of them, 1,000 samples of $\boldsymbol{\xi}$ and compute samples of the reaction parameters using the PCE (3.3). A strong correlation between the Arrhenius parameters can be noted which is consistent with other studies employed Bayesian approach [27, 47, 82], as shown in Fig. 4.5.

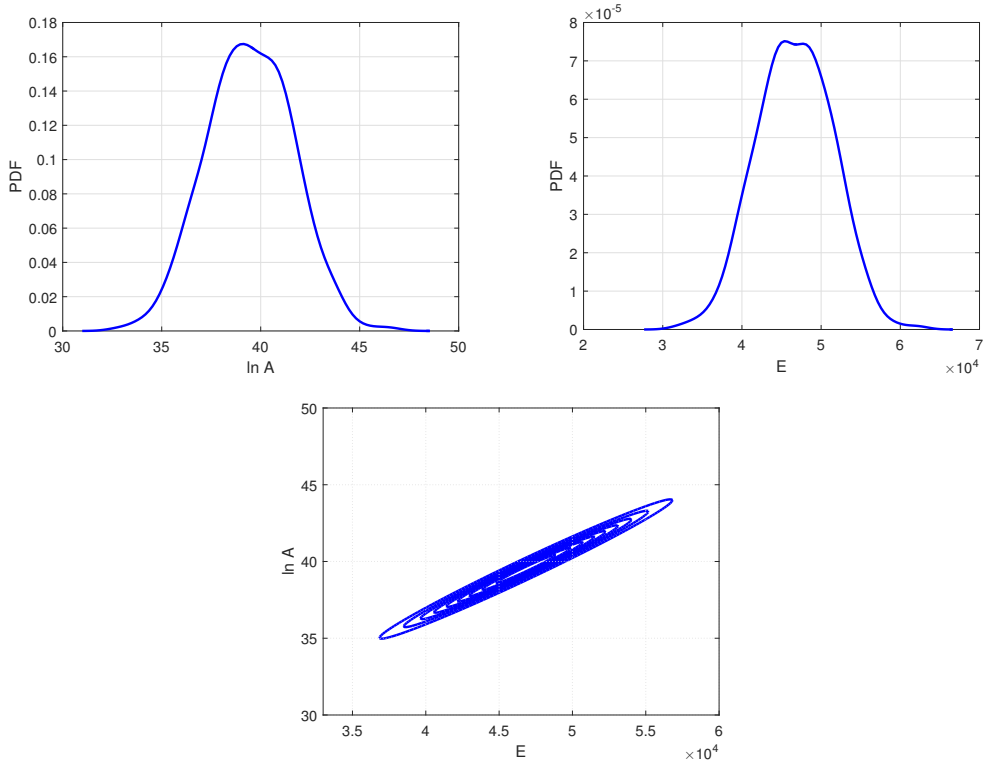

Figure 4.5: Posterior predictive marginal and joint distributions of the Arrhenius rate parameters.

The associated prediction uncertainties are shown in Fig. 4.6, where the posterior predictions are illustrated for different equivalent ratios. The figures show that the enhanced reduced model has predictive error bars that capture the GRI3.0 data sufficiently well, given the present calibration procedure.

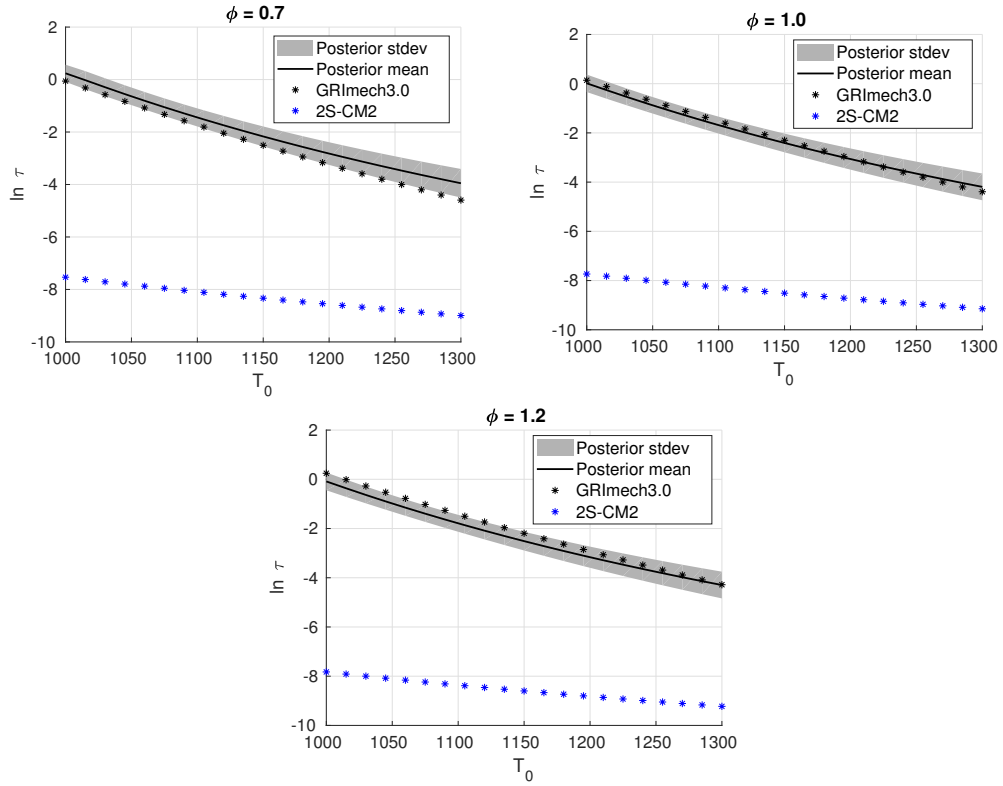

Figure 4.6: The results of calibration 2S-CM2 model using the GRI3.0 detailed model data, for various values of the equivalent ratio ϕ.

The calibration process is validated by predicting the autoignition delay time in different scenarios, i.e., the Baseline and BG2 compositions. Figures 4.7 and 4.8 show the autoignition delay time of the calibrated mechanism compared to the two-step mechanism and the full GRI3.0. The results indicate a good agreement between the calibrated model and the reference mechanism. The autoignition delay is a chemical process that depends on the radical pool and requires to account for species associated with the fuel decomposition process like formaldehyde or hydroxide [34]. It is therefore a chemical process difficult to capture by reduced chemical schemes. These results show the ability of the probabilistic embedded approach to extend the application range of the reduced model to predict autoignition without increasing the number of reacting species in the CFD solver and at a reduced computational cost.

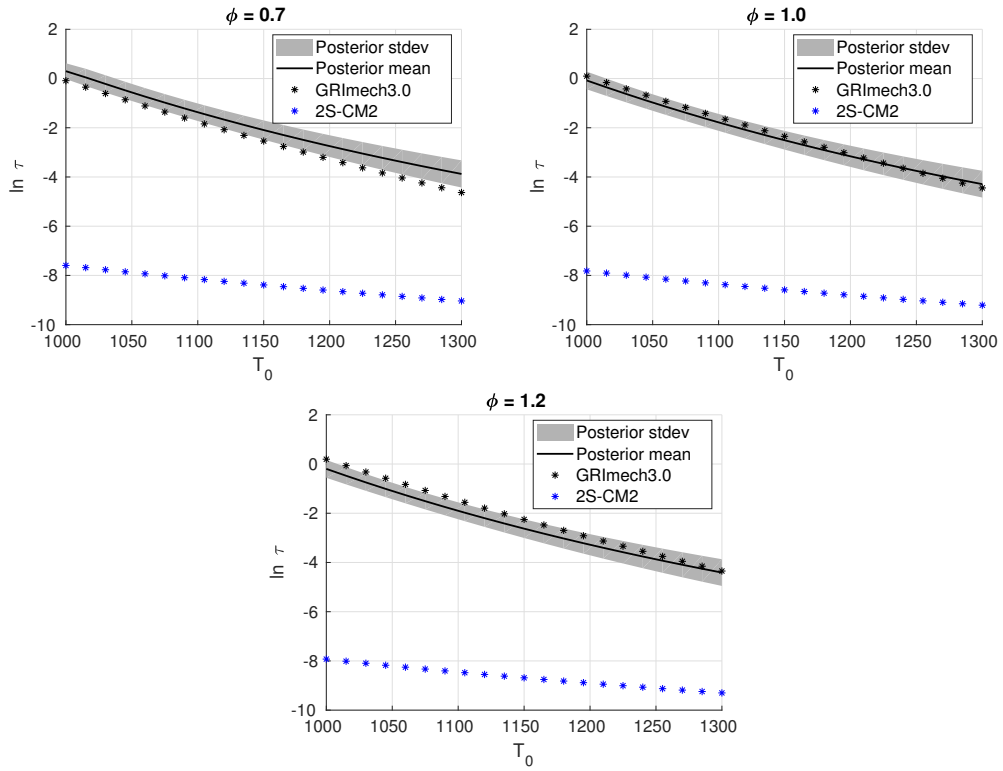

Figure 4.7: Autoignition delay time model predictions compared to GRI3.0: Baseline composition.

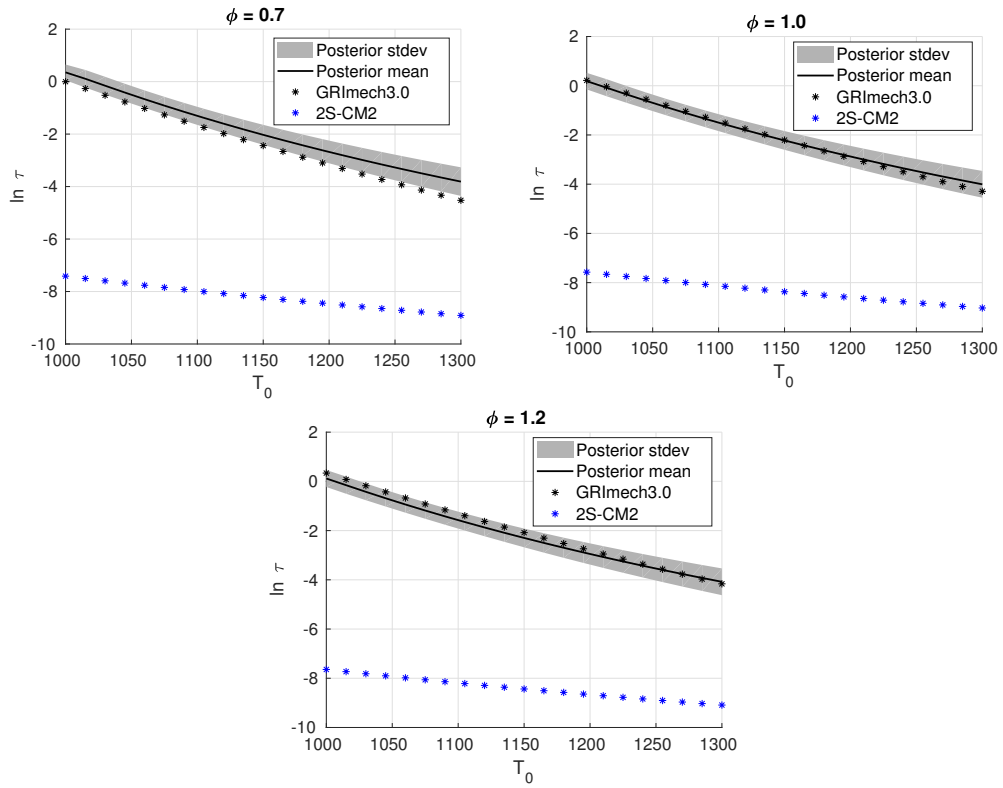

Figure 4.8: Autoignition delay time model predictions compared to GRI3.0: BG2 composition.

The extrapolation of the calibration process is now extended to the flame scenario, wherein the aim is to recover the flame properties (flame speed, flame thickness, adiabatic temperature and burned molar fractions of CO and CO_2) using the enhanced calibrated model. Here, the flame thickness is computed by using the temperature profile and estimated as follows

$$\delta = \frac{T_b - T_u}{\mathrm{MAX}\left(\frac{\partial T}{\partial x}\right)} \tag{4.5}$$

where T_b and T_u are burnt and unburnt gases temperature, respectively.

The predicted values of the flame properties for the freely propagating laminar premixed flames of methane and biogas are shown in Figs. 4.10, 4.9 and 4.11. The results indicate that after calibration process for autoignition calibration process, the updated 2S-CM2 model can still capture the flame speed and adiabatic flame temperatures in lean and stoichiometric conditions as the original mechanism. The flame speed is slightly overestimated, but the burnt gas temperature and the major combustion products are in good agreement with the original model. The model has been successfully extended to describe flame propagation and autoignition.

However, in rich conditions, no reliable solutions of the flame properties are predicted using the reduced model. Furthermore, it is shown that the variability of model parameters slightly influences the adiabatic flame temperature and only in rich conditions the molar fractions of the combustion products are influenced by the variability of the mechanism. As can be noted in Fig. 4.11 with the increase of the CO_2 in the biogas composition, the molar fraction predictions for rich conditions are unsatisfactory and require further investigation.

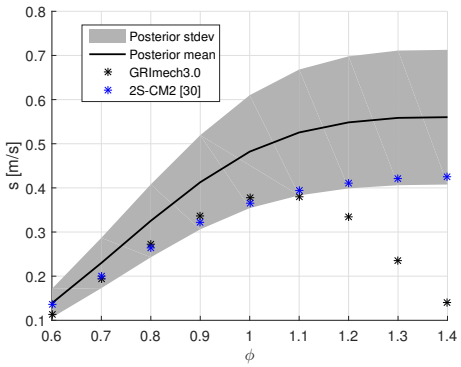

(a) Baseline flame speed

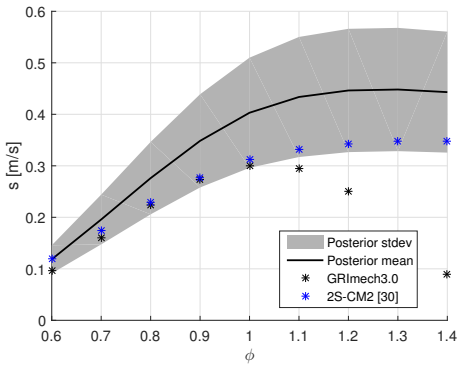

(b) BG1 flame speed

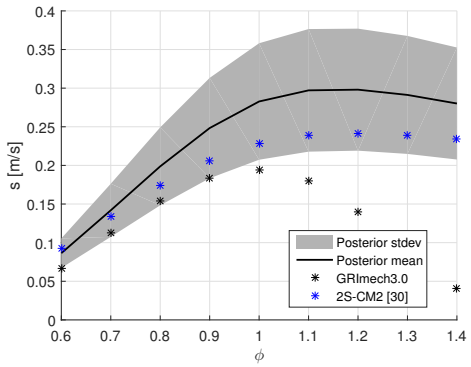

(c) BG2 flame speed

Figure 4.9: Flame speed predictions for the biogas-air premixed flame of the Tab. 4.1 at $p = 1$ bar and $T_0 = 300K$.

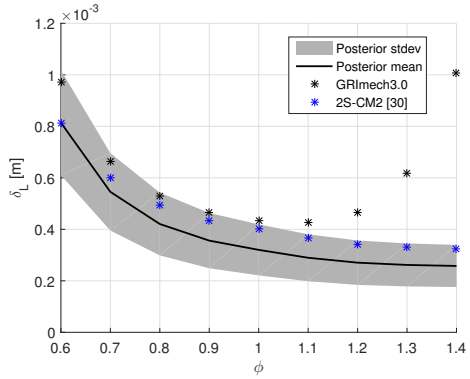

(a) Baseline flame thickness

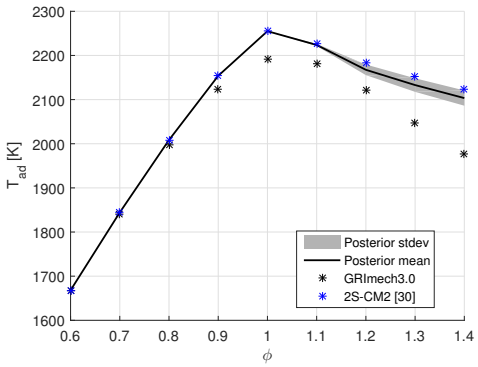

(b) Baseline adiabatic flame temperature

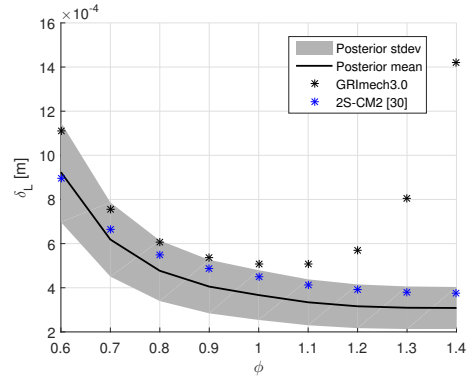

(c) BG1 flame thickness

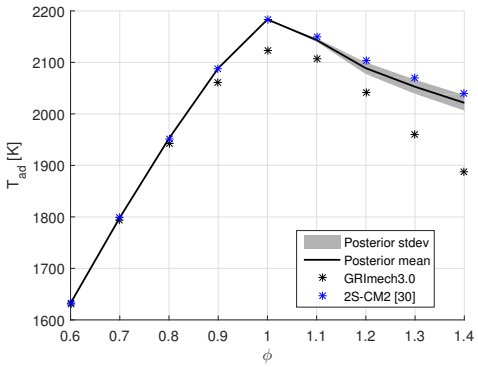

(d) BG1 adiabatic flame temperature

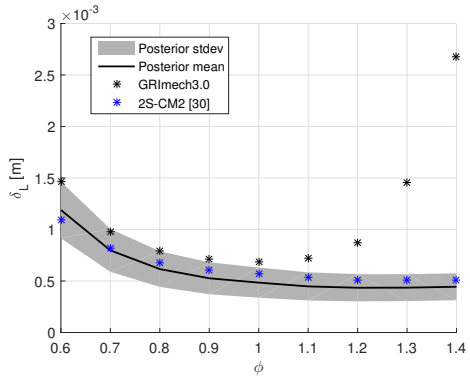

(e) BG2 flame thickness

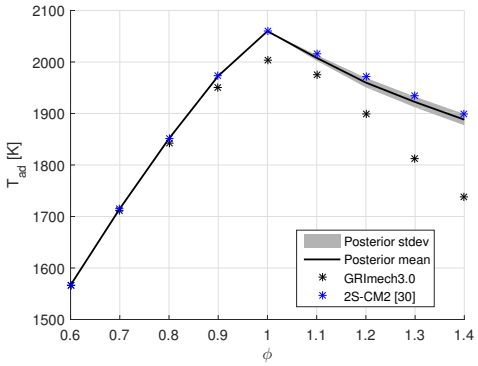

(f) BG2 adiabatic flame temperature

Figure 4.10: Flame thickness and adiabatic temperature predictions for the biogas-air premixed flame of the Tab. 4.1 at $p = 1$ bar and $T_0 = 300K$.

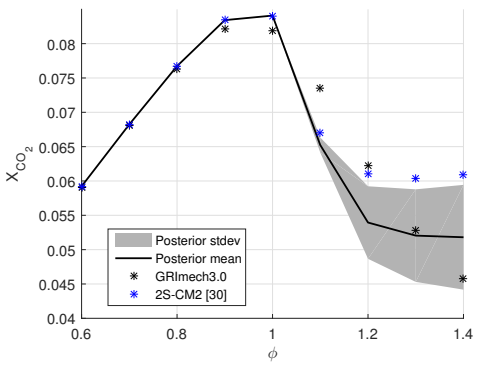

(a) Baseline CO_2 burned molar fraction

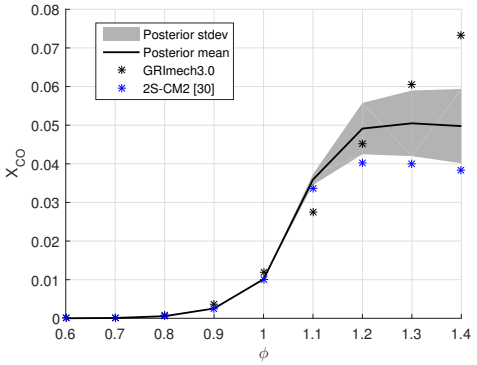

(b) Baseline CO burned molar fraction

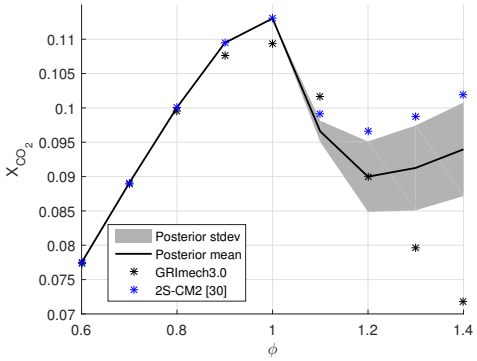

(c) BG1 CO_2 burned molar fraction

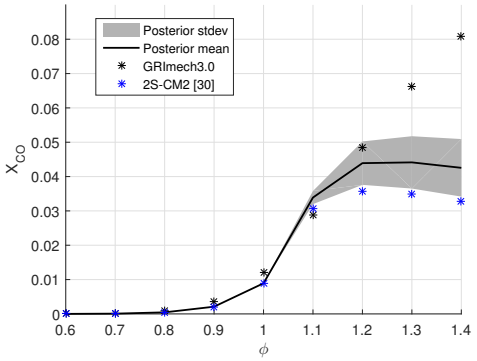

(d) BG1 CO burned molar fraction

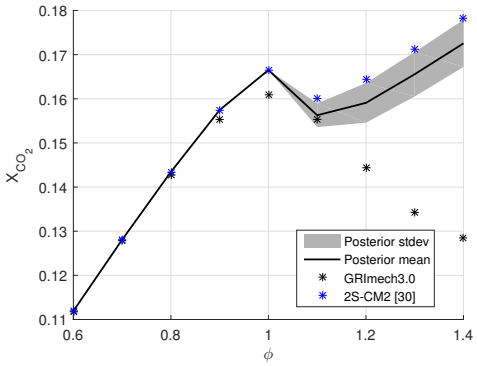

(e) BG2 CO_2 burned molar fraction

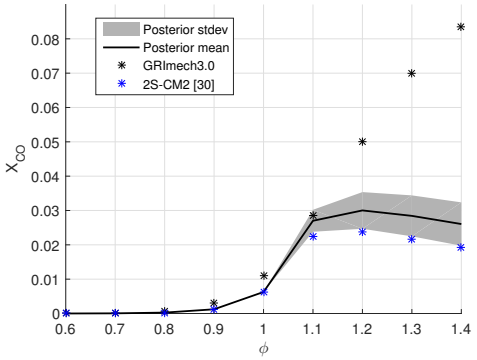

(f) BG2 CO burned molar fraction

Figure 4.11: Burned molar fractions predictions for the biogas-air premixed flame of the Tab. 4.1 at $p = 1$ bar and $T_0 = 300K$.

4.2.2 Second Calibration Experiment

As it has been shown in calibration experiment 4.2.1, the flame propagation and the species involved in premixed combustion can not be reproduced using the enhanced reduced mechanism at rich conditions. As proposed by Bibrzycki and Poinsot [34], an empirical correlation based on a pre-exponential factor adjustment (PEA) that redefines the constant rates as a function of the equivalence ratio ϕ can be used as an attempt to reproduce the correct behaviour in rich conditions. In this section, it

is applied a Bayesian calibration to the calibrated reduced model of the section 4.2.1 as an alternative to PEA in order to extend the applicability range of the reduced scheme to rich conditions and autoignition problems. The corresponding values for activation energy and logarithm of pre-exponential factor follow

$$
\begin{aligned}
E = \theta_0 &= \alpha_0 + \alpha_1 \xi_1, \\
A = exp(lnA) * F, \quad lnA &= (\alpha_{10} + \alpha_{11}\xi_1 + \alpha_{12}\xi_2)\,,
\end{aligned} \tag{4.6}
$$

where $F = \beta_0\phi^2 + \beta_1\phi + \beta_2$ is the pre-exponetial factor adjustment function. Here, the β_j values used in the original model [34] for the adjustment function are adopted. For the prior, the same priors of the case 4.2.1 are used, but we limited the α_{10} prior by 5%, i.e., $\alpha_{10} = \overline{\alpha}_{10}(1 + 0.05\eta)$, where $\overline{\alpha}_{10}$ is the nominal value of the pre-exponential factor [34] and η is an independent random variable with uniform distribution in the interval $[-1, 1]$.

A total of 20,000 parameter samples are obtained using MCMC. As in case 4.2.1, we take 10,000 samples of $\boldsymbol{\alpha}$ and, for each of them, 1000 samples of $\boldsymbol{\xi}$, and compute samples of the reaction parameters using the PCE (4.6). Figure 4.12 shows that there is a strong correlation between the lnA and E, as expected. Despite the structural deficiencies of the new enhanced reduced mechanism, it has predictive error bars that capture GRI3.0 data sufficiently well, as shown in Fig. 4.13.

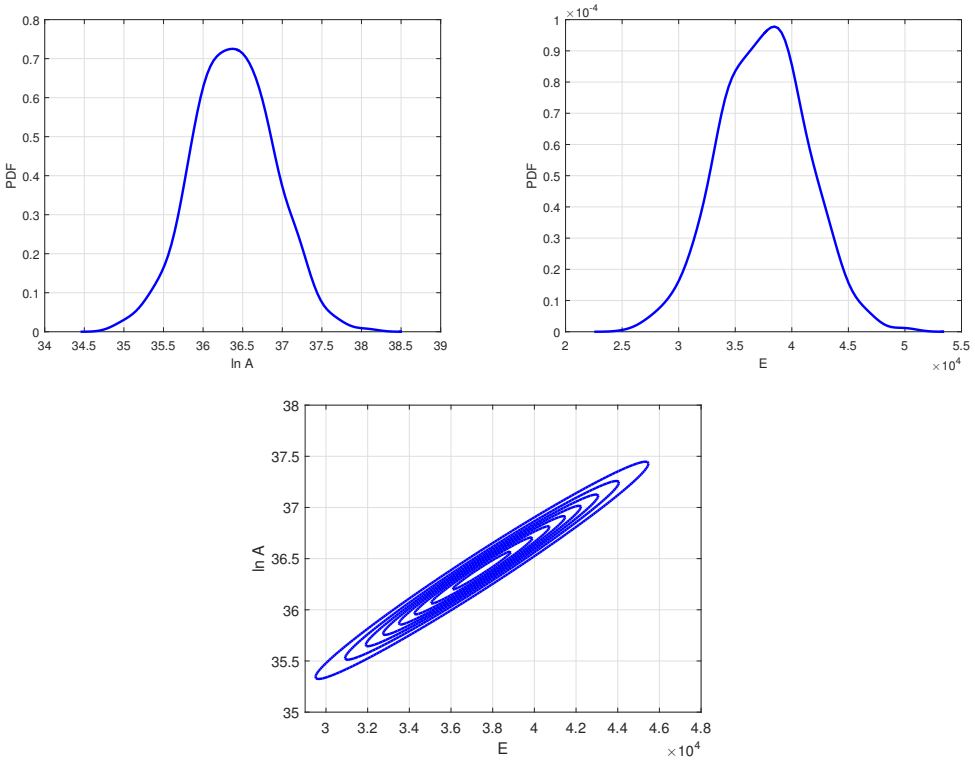

Figure 4.12: Posterior predictive and MAP marginal and joint distributions of the Arrhenius rate parameters for $\phi = 1.0$.

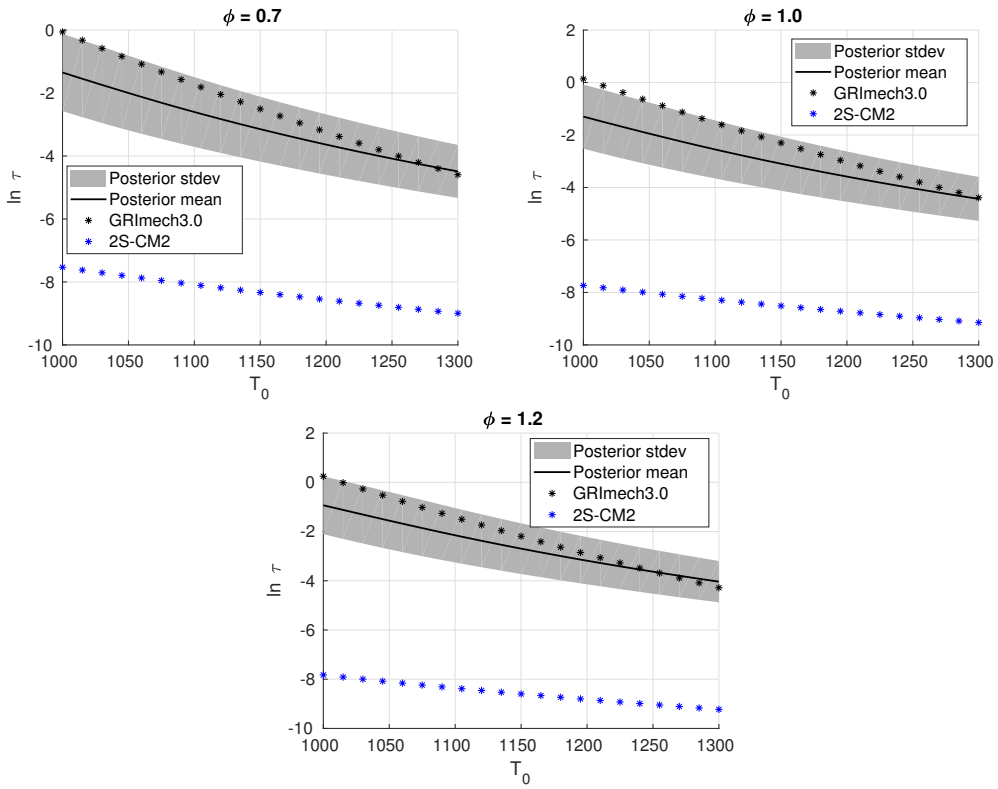

Figure 4.13: The results of calibration 2S-CM2-PEA model using the GRI3.0 detailed model data, for various values of the equivalent ratio ϕ.

As in the experiment 4.2.1, the calibration process is validated predicting the autoignition delay time for Baseline and BG2 compositions. Figures 4.14 and 4.15 illustrate the predictions of the calibrated mechanism for these mixtures. We can note that the new enhanced reduced model has predictive error bars that capture the data sufficiently well, given the present calibration procedure.

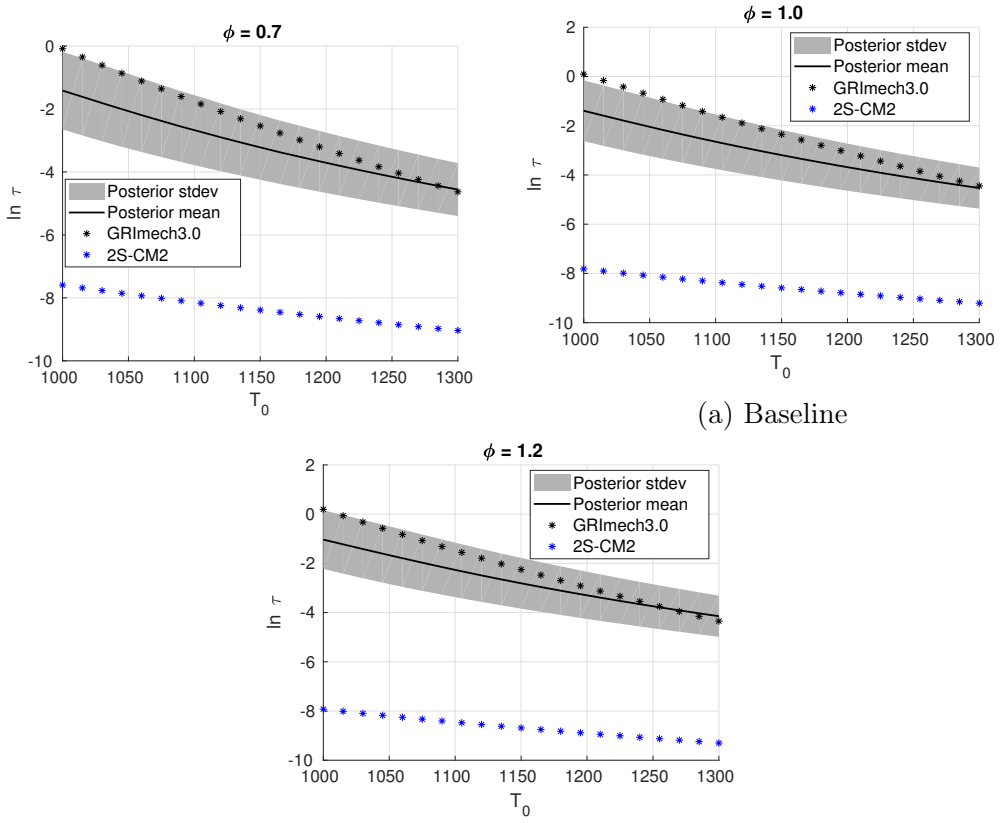

(a) Baseline

Figure 4.14: Autoignition delay time model predictions compared to GRI3.0: Baseline composition.

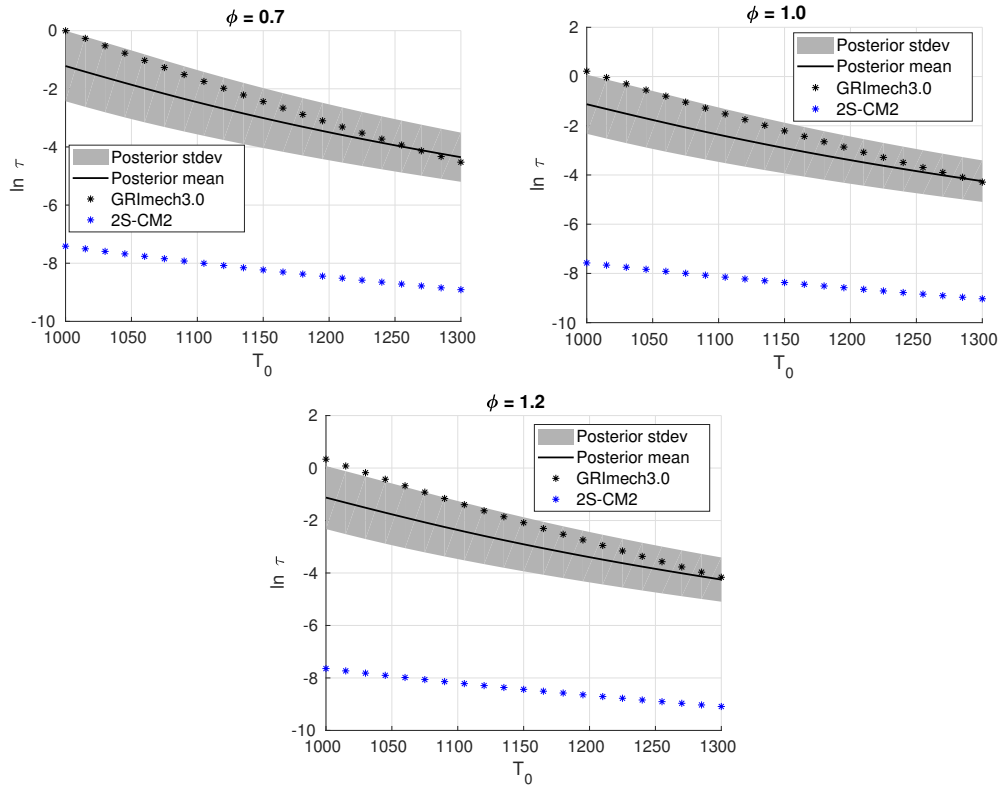

Figure 4.15: Autoignition delay time model predictions compared to GRI3.0: BG2 composition.

The prediction of properties of the laminar premixed flames for the conditions of the study (see Table 4.1), is shown in Figs. 4.16, 4.17 and 4.18. The plots show that the new enhanced reduced model can capture well the flame proprieties in lean and stoichiometric conditions. In addition, unlike the case 4.2.1, in rich conditions the reduced model can predict very well the laminar flame speed. Furthermore, the calibrated model can recovery the flame thickness tendency in rich conditions. However, the reduced mechanism calibrated has structural deficiencies that prevent the model from correctly reproducing the adiabatic flame temperature and combustion products in rich conditions. It can be noted that the variability of model parameters slightly influences the adiabatic temperature and the burned gas compositions. This is further discussed in the next sub-section.

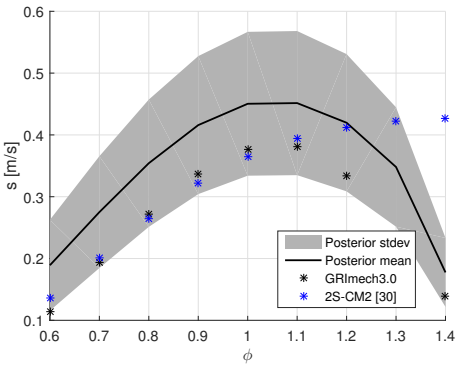

(a) Baseline flame speed

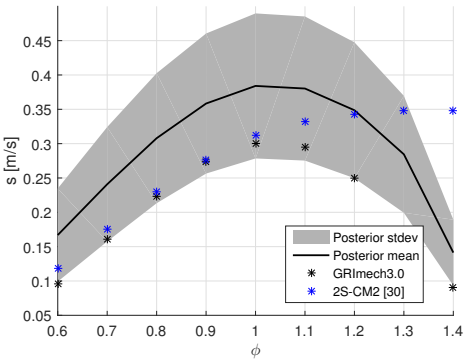

(b) BG1 flame speed

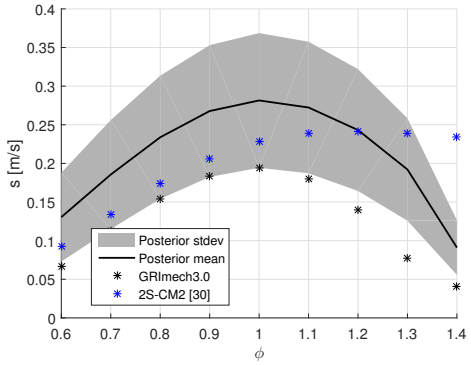

(c) BG2 flame speed

Figure 4.16: Flame speed predictions for the biogas-air premixed flame of the Tab. 4.1 at $p = 1$ bar and $T_0 = 300K$.

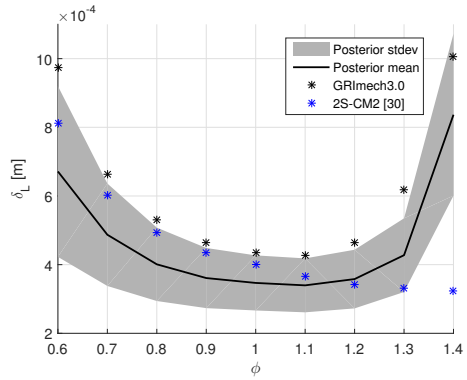

(a) Baseline flame thickness

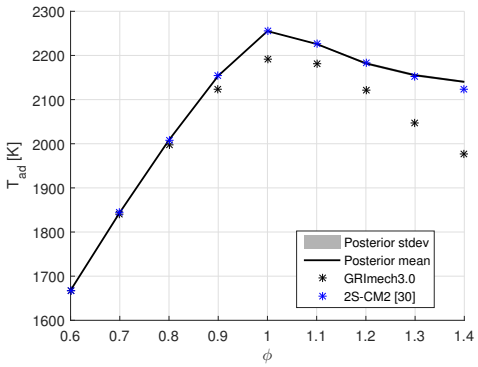

(b) Baseline adiabatic flame temperature

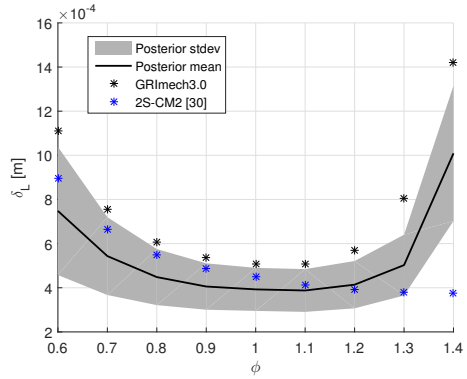

(c) BG1 flame thickness

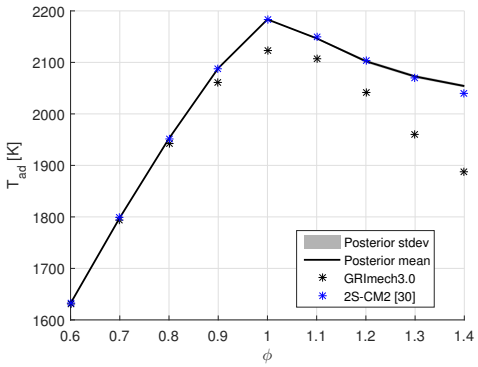

(d) BG1 adiabatic flame temperature

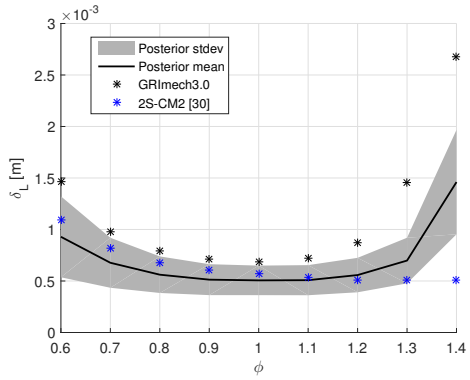

(e) BG2 flame thickness

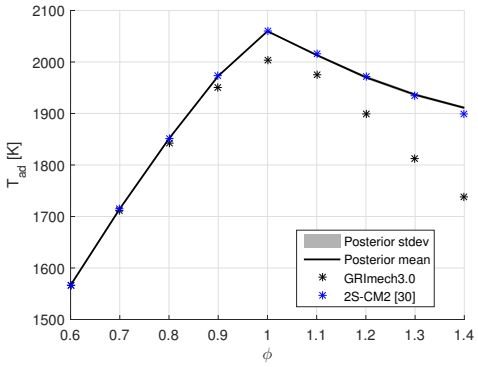

(f) BG2 adiabatic flame temperature

Figure 4.17: Flame thickness and adiabatic temperature predictions for the biogas-air premixed flame of the Tab. 4.1 at $p = 1$ bar and $T_0 = 300K$.

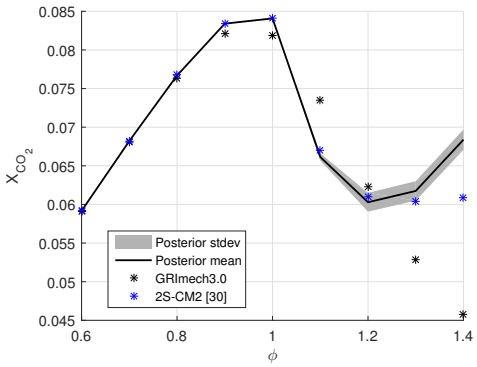

(a) Baseline CO_2 burned molar fraction

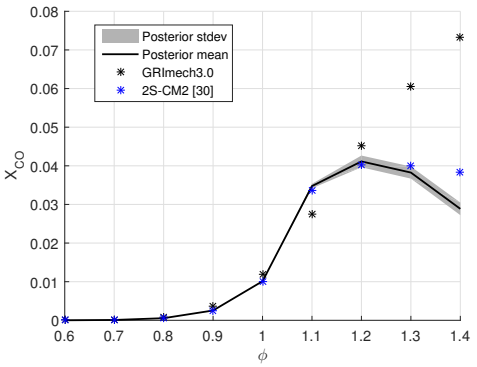

(b) Baseline CO burned molar fraction

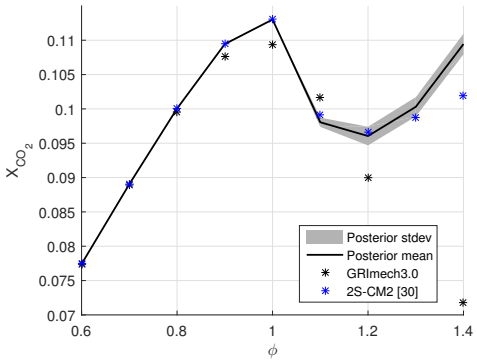

(c) BG1 CO_2 burned molar fraction

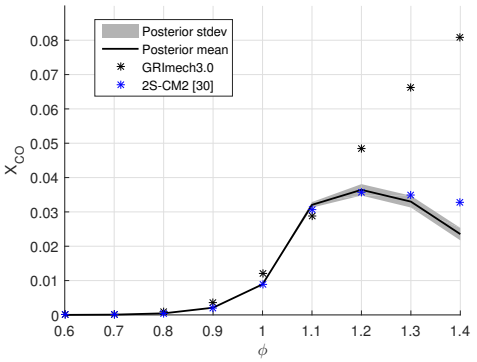

(d) BG1 CO burned molar fraction

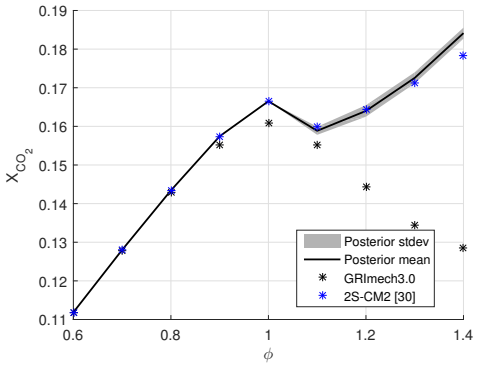

(e) BG2 CO_2 burned molar fraction

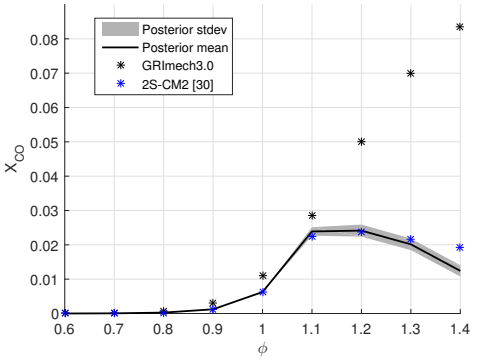

(f) BG2 CO burned molar fraction

Figure 4.18: Burned molar fractions predictions for the biogas-air premixed flame of the Tab. 4.1 at $p = 1$ bar and $T_0 = 300K$.

4.2.3 Extrapolating to broader operating conditions

Now, the aim is to investigate, through a UQ perspective, the sensitivities of the flame speed [83] and flame thickness, key QoIs in this context, for the operating condition variables: pressure p, inlet temperature T_0, and equivalence ratio of the mixture. This computational analysis might serve different purposes, like optimizing the design of physical experiments under uncertainties [84, 85], to validate models, or to enhance the understanding of the underlying phenomenology [83].

In order to make this analysis feasible, it is introduced a machine-learning model to alleviate the computational burden of providing flame speed and thickness predictions with quantified uncertainty to broader operating conditions. We developed a cheap-to-compute surrogate model to compute the premixed laminar flames.

In the recent years, DNNs are becoming a popular tool in producing surrogates in different domains involving physics-based models [2, 55–58, 61, 86] due to their robustness and generalization property, i.e., covering scenarios that have not been explored in the training process. The main idea of neural network surrogate models is to approximate the multivariate input/output behaviour of complex systems trough network architectures with hidden layers.

Here, the idea of densely connected convolutional networks (Dense-blocks) [87] used for visual recognition and object characterization is extended for a fully densely connected network regression strategy. Dense-block networks connect all layers directly to each other, thereby helping the training process with the improvement of information flow and gradients across the network [87]. Thus, given an input $\mathbf{x}^0$, the output of l-th layer is

$$\mathbf{x}^l = H^l([\mathbf{x}^0, \mathbf{x}^1, \ldots, \mathbf{x}^{l-1}]) \tag{4.7}$$

where $[\mathbf{x}^0, \mathbf{x}^1, \ldots, \mathbf{x}^{l-1}]$ refers to the concatenation of the predictions of the previous layers, $[0, \ldots, l-1]$. H^l is a non-linear transformation, which can be a composition of operations. In the present context, H^l is a composition of two consecutive functions, batch normalization [88] followed by a rectified linear unit (ReLU) [89]. Finally, the dense-block presents two design parameters, the number of the layers L and the growth rate K, which is the number of output features of each single layer.

Thus, to improve the computational efficiency, a surrogate model for uncertainty quantification using deep densely connected networks is developed. The surrogate model is expressed formally in a compact notation as:

$$\mathbf{y} = f(p, T_0, \phi, E, lnA; \mathbf{w}), \tag{4.8}$$

where the output $\mathbf{y}$ represents the flame physicochemical properties (flame speed and flame thickness), and $\mathbf{w}$ refers to network parameters to be identified along the training. The randomness of the flame speed is induced by the calibrated parameters.

Training the neural network means learning about parameters $\mathbf{w}$, using data from the physics-based model, with respect to a certain loss function. The mean squared error (MSE) is a loss function widely used for regression problems [90]. In

the present work, the L_2 regularized MSE training loss function is considered

$$L_{MSE} = \frac{1}{N}\sum_{i=1}^{N} \|\mathbf{f}_i - \mathbf{y}_i\|_2^2 + \alpha\Omega(\mathbf{w}) \tag{4.9}$$

where N is the number of samples in the training, $\mathbf{f}_i$ and $\mathbf{y}_i$ are the outputs predicted by the neural network and the physics-based model, respectively. Here the penalty function is given by $\Omega(\mathbf{w}) = \frac{1}{2}\mathbf{w}^T\mathbf{w}$.

The Stochastic Gradient Descent (SGD) algorithm [59] is used as the optimizer for parameter learning in network training. The gradient descent algorithms attempt to optimize the objective function by following the steepest descent direction given by the negative of the gradient. Following this negative gradient for each new sample or batch of samples chosen from the data set gives a local estimate of which direction minimizes the cost and is referred to as stochastic gradient descent [91].

Taking a MSE loss function, the gradient of the loss $g(\mathbf{w})$ with respect to $\mathbf{w}$ is given as follows

$$g(\mathbf{w}) = \frac{1}{M}\sum_{i=1}^{M} \nabla_{\mathbf{w}} L_{MSE} \tag{4.10}$$

where M is the size of the batch. Then, the SGD follows the estimated gradient as

$$\mathbf{w} \leftarrow \mathbf{w} - \beta g \tag{4.11}$$

where β is the learning rate which controls how large a step to take in the direction of the negative gradient. Several SGD algorithms are available [59]. Algorithm 1 presents a summary of the training strategy.

Algorithm 1 Network training strategy to optimize the networks parameters $\mathbf{w}$

Require: Dense block network configurations, learning rate β, mini-batch size M, Adam hyperparameters.

$\mathbf{w} \leftarrow \mathbf{w}_0$
for number of epochs **do**
  for each minibatch $(\mathbf{x}^m, \mathbf{y}^m)_{m=1}^{M}$ of the training sample set **do**
    $g \leftarrow \frac{1}{M}\sum_{i=1}^{M} \nabla_{\mathbf{w}} L_{MSE}$
    $\mathbf{w} \leftarrow \mathrm{SGD}(\mathbf{w}, g, \beta)$
  end for
end for
return w

In the training process, the root mean squared error (RMSE) is used for

monitoring the convergence of the training and test errors. It is defined as

$$RMSE = \sqrt{\frac{1}{N_{train}} \sum_{i=1}^{N_{train}} \|\mathbf{y}_i - \hat{\mathbf{y}}_i\|_2^2} \tag{4.12}$$

where N_{train} is the number of samples for training the surrogate model, and $\hat{\mathbf{y}}_i$ is the neural network output. Note that the number of samples in the training phase can be different from the number of samples in the test phase.

The performance analysis adopted in the present context aims to evaluate the accuracy and efficiency of the neural network architecture in constructing a surrogate model. Here, accuracy is measured from a distance criterion between the prediction of the surrogate model and that predicted by the original model. To evaluate the quality of the surrogate model two metrics are considered, which are the coefficient of determination (R^2-score) [92] and L_2 relative error. The coefficient of determination is defined as

$$R^2 = 1 - \frac{\sum_{i=1}^{N_{test}} \|\mathbf{y}_i - \hat{\mathbf{y}}_i\|_2^2}{\sum_{i=1}^{N_{test}} \|\mathbf{y}_i - \overline{\mathbf{y}}\|_2^2} \tag{4.13}$$

where $\overline{\mathbf{y}} = \frac{1}{N_{test}} \sum_{i=1}^{N_{test}} \mathbf{y}_i$ is the mean of test samples. Finally, the L_2 relative error metric is defined as

$$\epsilon^2 = \frac{1}{N_{test}} \sum_{i=1}^{N_{test}} \left(\frac{\mathbf{y}_i - \hat{\mathbf{y}}_i}{\mathbf{y}_i} \right)^2 . \tag{4.14}$$

where N_{test} is the number of samples in the test dataset.

The R^2-score metric represents the normalized error, allowing the comparison between surrogate models trained by different datasets, with values close to 1 corresponding to the best accuracy of the surrogate models.

The neural network is constructed using the open platform Tensorflow [71]. Here, it is considered a dense block with $L = 9$ and $K = 20$. The total number of parameters in the network is 18,912. Training the network means learning the network parameters $\mathbf{w}$ using training data with respect to certain loss function. It is adopted a supervised learning strategy, wherein the data set for the training process is provided by simulations of 1D laminar flame using the Cantera software. Also, it is used the MSE (4.9) for this purpose. The Adam optimizer algorithm is used for parameter learning [93] considering a weight decay of 1×10^{-5} and an initial learning rate of 1×10^{-3}, where a learning rate scheduler is used dropping 5 times on plateau of the rooted mean squared error (4.12). Finally, it is used 100 epochs in the training process.

In general, combustion systems are operated with leaner mixtures to increase the efficiency and reduce the formation of pollutants [94, 95]. Accordingly, the surrogate is constructed bearing that in mind by choosing the surrogate input space

of operating conditions: $\phi \in [0.6, 1.0]$, $T_0 \in [300, 450]K$, and $p \in [1.0, 2.0]$bar. For the training, this subdomain of the input space is divided in regular partitions defined by 0.2, 50 K and 0.5 bar, respectively. The calibrated parameters E and lnA, are chosen those from the enhanced model of Case 4.2.2. So, the training set is built by randomly selecting 1000 samples of those parameters and combine them with the operating inputs of the regular grid to obtain 36,000 input points, having the corresponding outputs computed using the original flame speed model. Moreover, 80% is used for training and the remaining 20% is used for the accuracy assessment of the resulting surrogate model.

The network is trained on a Xeon E5-2630 2.30 GHz CPU which requires about 180 seconds for training 100 epochs. Figure 4.19 a shows the RMSE decay with the number of epochs during the training process. It is noted that the RMSE decay stabilizes after 60 epochs. Also, the accuracy is verified with the L^2 relative error that achieves values lower than 0.6% and the coefficient of determination of 0.997.

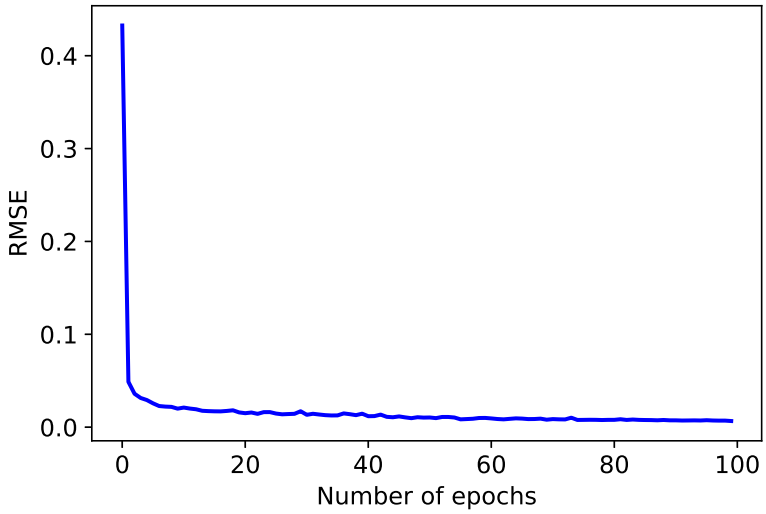

Figure 4.19: (a) RMSE decay with the number of epochs in the training process.

For further illustrated the performance of the surrogate model to predict the properties of a premixed laminar flame, Fig. 4.20 plots a comparison between the flame speed and flame thickness obtained from Cantera and the surrogate model for $T_0 = 330K$ and $p = 1.2bar$, where this condition is not considered when training the network. It is shown that the neural network surrogate can accurately predict the laminar flame properties even for operation conditions outside the training set, predicting the flame speed and flame thickness with L^2 relative errors lower than 1% and coefficient of determination equals 0.98. In terms of computational cost, the surrogate model required around 3 seconds to compute the flame physicochemical properties for all pre-exponential factors, activation energies, and equivalent ratios, while in the Cantera software the time required to compute the flame properties

is around 2 hours. This shows the computational efficiency of the surrogate model to predict flame properties. The efficiency of the surrogate model is more explored further ahead.

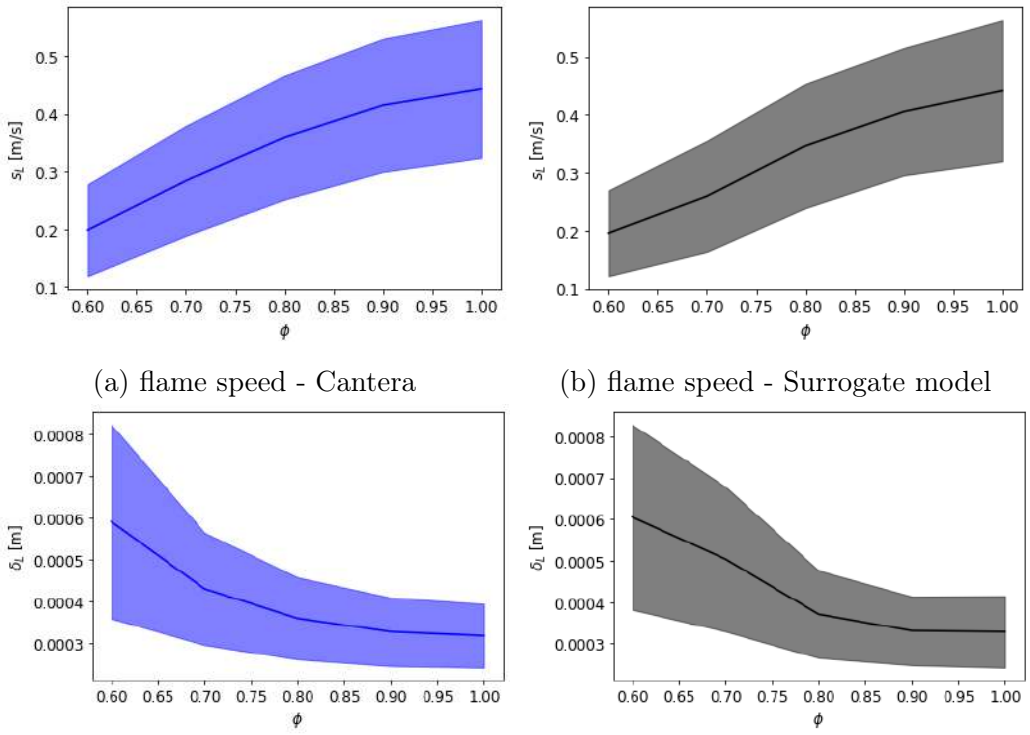

(a) flame speed - Cantera

(b) flame speed - Surrogate model

(c) flame thickness - Cantera

(d) flame thickness - Surrogate model

Figure 4.20: The flame physicochemical properties predicted by the original and surrogate models.

After building the surrogate, now it is used the standard MC method to propagate uncertainties arising from the calibration of the Arrhenius parameters into the flame speed. Next, it is measured the degree of uncertainty of the predictions using the coefficient of variation, defined as the ratio between the standard deviation σ_y and the mean μ_y of the flame speed

$$\mathrm{cv}(\mathbf{r}) = \frac{\sigma_{\mathbf{y}}(\mathbf{r})}{\mu_{\mathbf{y}}(\mathbf{r})} \tag{4.15}$$

where vector $r = (p, T_0, \phi)$ contains the operating condition.

Figures 4.21 and 4.22 give an overall picture by displaying a mapping between the operating conditions and the uncertainty on flame properties expressed by the coefficient of variation, after marginalizing out lnA and E with the use of MC method. It is presented an explicit quantification of the induced uncertainty resulting from the calibration into the predictions, that helps to understand the limits of the calibrated model when leveraged to a more elaborate setting. More specifically, to make more accessible the visualization of the results, it is depicted

this mapping for six fixed pressures levels, allowing to make explicit the strong dependence of the output uncertainties regarding different levels of such operating input. A critical aspect to highlight in the very beginning is the high values of cv in particular regions of the operating conditions, especially those near the low bound for leaner mixtures. That might be, partially, explained by the burning conditions near flammability limits [96], which bears the potential to amplify the propagated uncertainties. However, it could also be attributed to the calibrated model's use beyond its intrinsic prediction limits. It is not possible to make a definitive judgment without resorting to more data for the calibration process covering such operating conditions, which falls outside this particular study. Also, note that variabilities of flame properties are less pronounced at regions near the stoichiometric condition, while the inlet temperature and pressure level significantly impact the flame speed variability, especially at leaner conditions. Furthermore, it is verified lower variabilities of flame thickness at higher inlet temperatures, which can be explained by the simpler chemical pathways occurring as the mixture is preheated and it is operated at higher temperatures. All these considerations convey critical information to understand the limitations of the modeling. However, they can also be employed, as mentioned before, in the design of physical experiments, allowing the choice of optimal operating conditions less sensitive to uncertainties contaminating the interpretation of the results.

Also, it is worth highlighting that such UQ analysis would need about 210,000 computer runs of the original model. The construction of the surrogate model required 36,000 samples, which generates a significant computational gain. Such efficiency can be computed as a function of the number of samples, as follows

$$G = \left(1 - \frac{N_S}{N_{MC}}\right) \times 100 \tag{4.16}$$

where N_S is the number of samples for surrogate model construction and N_{MC} is the number of samples needed to perform a UQ analysis similar to that performed here. Thus, we achieve an efficiency of about 83% in the UQ analysis. This demonstrates the ability of DNNs for surrogate model developments and optimization.

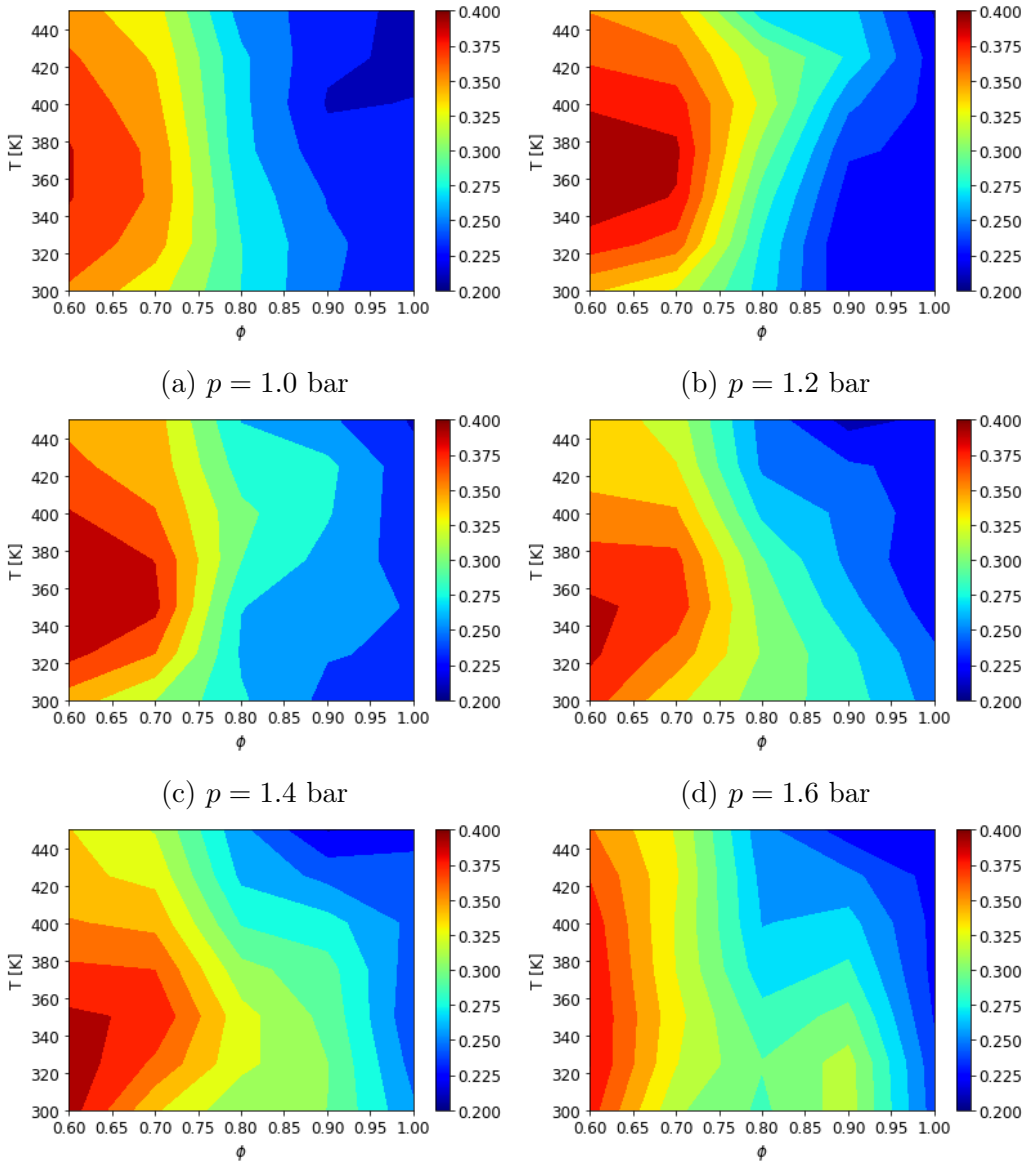

(a) $p = 1.0$ bar

(b) $p = 1.2$ bar

(c) $p = 1.4$ bar

(d) $p = 1.6$ bar

(e) $p = 1.8$ bar

(f) $p = 2.0$ bar

Figure 4.21: Flame speed variability at different operation conditions.

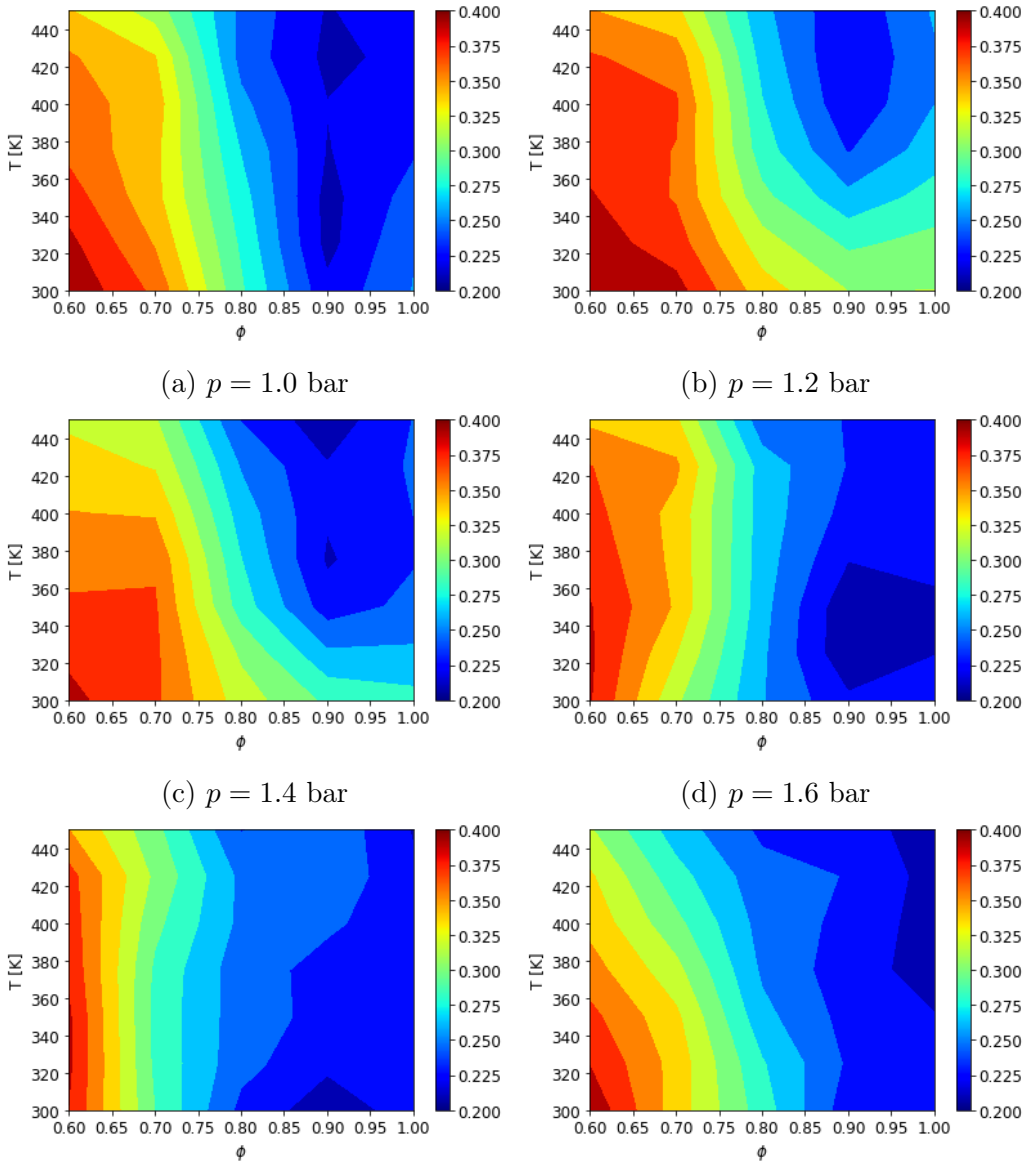

(a) $p = 1.0$ bar (b) $p = 1.2$ bar

(c) $p = 1.4$ bar (d) $p = 1.6$ bar

(e) $p = 1.8$ bar (f) $p = 2.0$ bar

Figure 4.22: Flame thickness variability at different operation conditions.

4.3 Neural network model discrepancy

This section illustrates the development of alternatives for the model discrepancy embedding presented before. Here, it is presented an approach which the model discrepancy is embedded in the temporal evolution of chemical species concentrations. Such an approach aims to improve the predictability of physicochemical properties of the benchmark combustion scenarios using the reduced chemical model correcting the chemical concentrations in each time-step. Also, a DNN is used to capture an appropriate functional form for the model correction. The proposed method is evaluated in a 0D reactor.

In this context, the discrepancy term is incorporated at each time-step in the net production rates of species. Then, the inputs of the neural network are the states in the previous time of the homogeneous combustion process. The time-discretized form of the 0-D reactor is given as follows

$$\mathbf{Y}(t+\Delta t) - \mathbf{Y}(t) = \Delta t \left[\frac{\boldsymbol{\omega}_e(\mathbf{Y}(t), T(t))}{\rho(t)} \right] \tag{4.17}$$

$$T(t+\Delta t) - T(t) = \Delta t \left[\frac{\boldsymbol{h}(\boldsymbol{Y}(\boldsymbol{t}), T(t)) \cdot \boldsymbol{\omega}_e(\boldsymbol{Y}(t), T(t))}{\rho(t) c_p(t)} \right] \tag{4.18}$$

where $\boldsymbol{\omega}_e$ are the enhanced net production rates of species. The enhanced net production rates in compact form is given as

$$\boldsymbol{\omega}_e = \boldsymbol{\omega}(\mathbf{Y}(t), T(t), \boldsymbol{\epsilon}) + \boldsymbol{\epsilon}(\mathbf{Y}(t), T(t); \mathbf{w}) \tag{4.19}$$

where $\mathbf{Y}(t)$ is the vector of mass fractions and $\boldsymbol{\theta}$ is vector that represents the kinetic parameters. Here, the discrepancy term ϵ_k is modeled as a FCNN, where $\mathbf{w}$ is a vector of parameters defining the FCNN.

The neural network is constructed using the open platform Tensorflow. Here, the architecture of the network is inspired in [60]. In their work, several tests for different numbers of hidden layers and different numbers of neurons per layer are performed analyzing the FCNN accuracy acting as a surrogate model. After try-and-error tests, it is fixed an architecture composed of four hidden layers with 20 neurons each. Here, a ReLU activation function is used in the outputs of the hidden layers. That activation function imposes that the outputs of the hidden layers are strictly positive. Also, a linear activation is imposed in the output layer allowing both positive and negative values to the discrepancy term. The total number of parameters of FCNN is 1440. Figure 4.23 depicts a schematic view of the FCNN architecture. More specifically, it shows the model discrepancy construction, wherein the input dimensionality depends on the number of species in the reduced mechanism and temperature. The same is valid for the output dimensionality.

Also, the model discrepancy is trained with data produced by numerical simulation of GRI3.0 detailed mechanisms available in Cantera software, in a model-to-model calibration. More specifically, we adopt a supervised learning strategy, wherein the the training dataset are physicochemical properties predicted by numerical simulations of the 0-D homogeneous reactor using the GRI3.0 detailed mechanism. As in section 4.2, it is chosen as training data the autoignition delay time for the BG1 mixture at atmospheric pressure, over a range of equivalent ratio $\phi \in [0.6, 1.4]$ and a range of initial temperature $T_0 \in [1000, 1300K]$ varying by 0.2 and 30K, respectively. Therefore, the training dataset is composed by 55 autoignition delay times of biogas/air combustion.

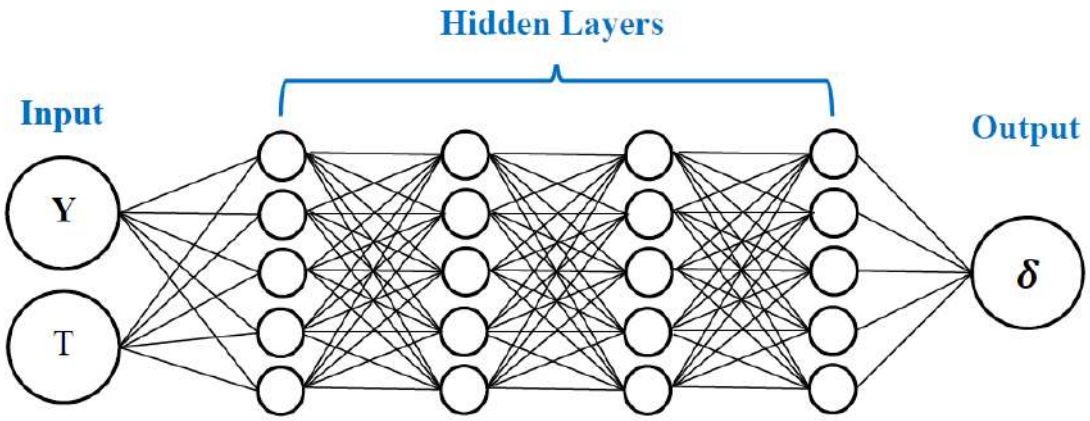

Figure 4.23: An overview of neural network architecture.

In the training process, it is adopted the L_2 regularized MSE training loss function equation (4.9). Since the loss function is dependent of the model outputs and their derivatives in relation to the network parameters, providing derivatives information can be a difficult task. To overcome this difficult, the PSO method [97, 98] is used in the present study to train the model discrepancy. An overview of this method is shown in appendix B.0.2. The PSO optimization scheme is implemented using PySwarms [99], an extensible research toolkit for particle swarm optimization in Python. Algorithm 2 details the optimization scheme, where it allows integrating the machine learning tools within the Cantera package. The number of particles, $N_{particles}$, and the number of iterations, N_{iter}, of the PSO scheme are given as inputs. Here, after initial tests with the PSO scheme, we adopt the number of particles and the number of iterations equals 20 and 10, respectively. Such values are in good agreement with the literature [100]. Also, we follow [101] and assume the PSO parameters as $\omega_v = 0.9$, $c_1 = 2.8$ and $c_2 = 1.3$. Here, for each time-iteration, the model discrepancy term is updated receiving as input the vector containing the chemical species and the temperature. After, using Cantera software, the enhanced net production rate is computed and embedded in the equations of the 0D scenario, correcting the chemical concentrations and the heat release in each time-step. At the end of Algorithm 2, it is returned the trained parameters of the neural network $\mathbf{w}$. More specifically, the algorithm returns the particle that minimizes the loss function (4.9). Also, the convergence of the training process is monitored by observing the loss function decay.

Algorithm 2 Optimization scheme of the neural network parameters.

Require: Training data, $N_{particles}$, N_{iter}, inertial weight ω_v, cognitive learning factor c_1 and social learning factor c_2

Initialize the swarm: position vector $\mathbf{x_p}$ (randomly) and velocity vector $\mathbf{v_p}$ (randomly)

Architecture: Construct the neural network ▷ Call Tensorflow

for $iter = 1$ to N_{iter} **do**

  for $p = 1$ to $N_{particles}$ **do**

    Set $\mathbf{w} = \mathbf{x}_p$

    Initialize $t = 0$

    for $i_t = 1$ to N_t **do**

      Update the model discrepancy term: $\boldsymbol{\epsilon}(\mathbf{Y}(t), T(t); \mathbf{w})$

      Compute $\boldsymbol{\omega}_e = \boldsymbol{\omega}(\mathbf{Y}(t), T(t), \boldsymbol{\theta}) + \boldsymbol{\epsilon}(\mathbf{Y}(t), T(t); \mathbf{w})$ ▷ Call Cantera

      Solve the 0D problem:

      $$\frac{d\mathbf{Y}}{dt} = \Delta t \left[\frac{\boldsymbol{\omega}_e(\mathbf{Y}(t), T(t))}{\rho(t)} \right]$$

      $$\frac{dT}{dt} = \Delta t \left[\frac{\boldsymbol{h}(\boldsymbol{Y}(\boldsymbol{t}), T(t)) \cdot \boldsymbol{\omega}_e(\boldsymbol{Y}(t), T(t))}{\rho(t) c_p(t)} \right]$$

      $t = t + i_t \times \Delta t$

    end for

    Assess the individual optimal position (B.1)

    Assess the global optimal position (B.2)

    Update the position and velocity: (B.4) and (B.3)

  end for

end for

return $\mathbf{w} = \arg\min_{\mathbf{x_p}} L_{MSE}(\mathbf{x_p})$

Figure 4.24 shows the enhanced predictions associated with the machine learning discrepancy source term. It can be seen that the enhanced reduced mechanism can not recovery the autoignition delay time. That might be explained due to the large discrepancy of the ignition process provides by the reduced model compared with the detailed one. More specifically, the ignition process predicted using the reduced model occurs in 10^{-4}s, while for the detailed model this process occurs on the second's scale. Thus, embedding the discrepancy model as an additive source term can not mitigate that large time scale error of the ignition process.

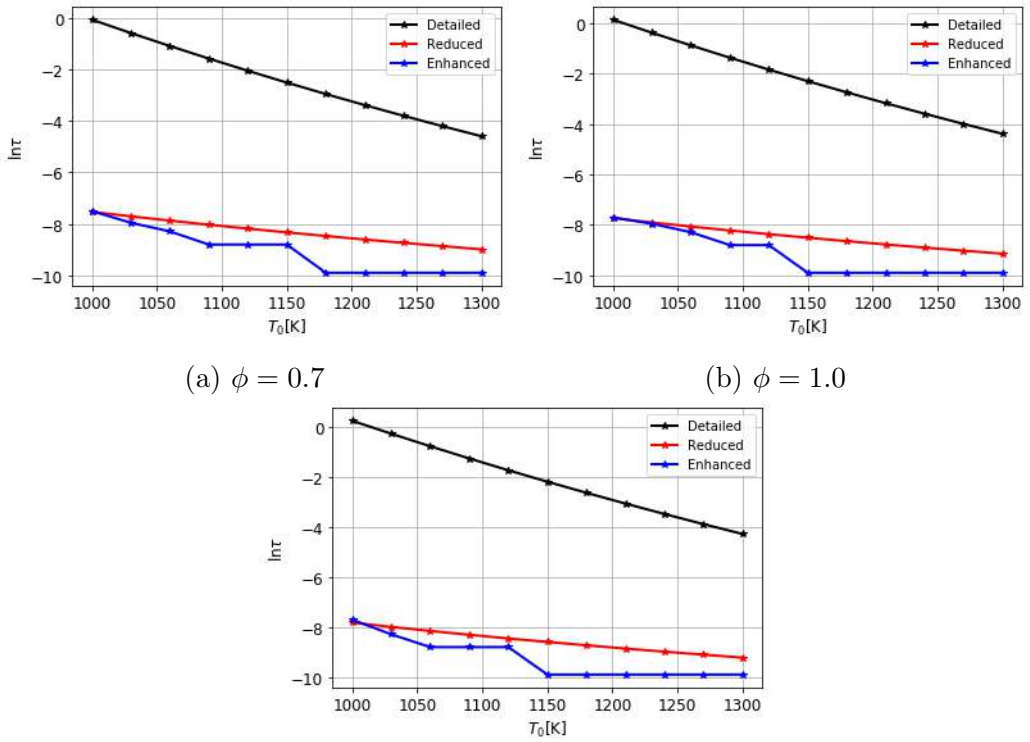

(a) $\phi = 0.7$ (b) $\phi = 1.0$

(c) $\phi = 1.2$

Figure 4.24: Autoignition delay time model predictions compared to GRI3.0: BG1 composition.

It is well-known that the chemical kinetic parameters might have a pronounced effect on the predicted ignition delay time. Sensitivity analysis of combustion processes to the rate constants can reveal the rate-limiting steps controlling the ignition process and provide valuable insights into the mechanism calibration, (see appendix A). Several works [1, 15, 25, 26], try to optimize reduced mechanisms searching best values (Bayesian Inference) of the kinetic parameters of the most sensitive reactions. Also, such parameters are used to calculate the reaction rates, from Arrhenius law, and act as multiplying factors in the net production rates of the species. Here, to try enhance the predictability of our approach, the embedded discrepancy model is reformulated as a multiplying factor in the net production rates of species. More specifically, a selective choice is proposed embedding a multiplying discrepancy term only in the species of the irreversible reaction, the most sensitive reaction, in the 2S-CM2 reduced mechanism. Being more clear, the discrepancy terms are embedded in the net production rates of CH_4, O_2, CO, and H_2O. Thus, the the proposed net production model is given as follows

$$\omega_{k_e} = \omega_k(\mathbf{Y}(t), T(t), \boldsymbol{\theta}) \times \epsilon_k(\mathbf{Y}(t), T(t); \mathbf{w}). \tag{4.20}$$

Without loss of generality, the same architecture with 4 hidden layers and 20 neurons is used to construct the multiplying discrepancy terms. Figure 4.25 depicts

the autoignition delay times for BG1 composition. Note that the multiplicative enhanced reduced model returns better predictions of the autoignition times mainly in lower temperatures. Also, it is verified that this new enhanced model can predict very well the delay times even for $\phi = 0.7$, wherein this equivalence ratio is not used in the training process. Here, it is worth highlighting that the only difficulty of this strategy falls on the integration of machine learning tools to the black-box software. However, the training process is relatively cheap taking around 10 minutes to train the network parameters.

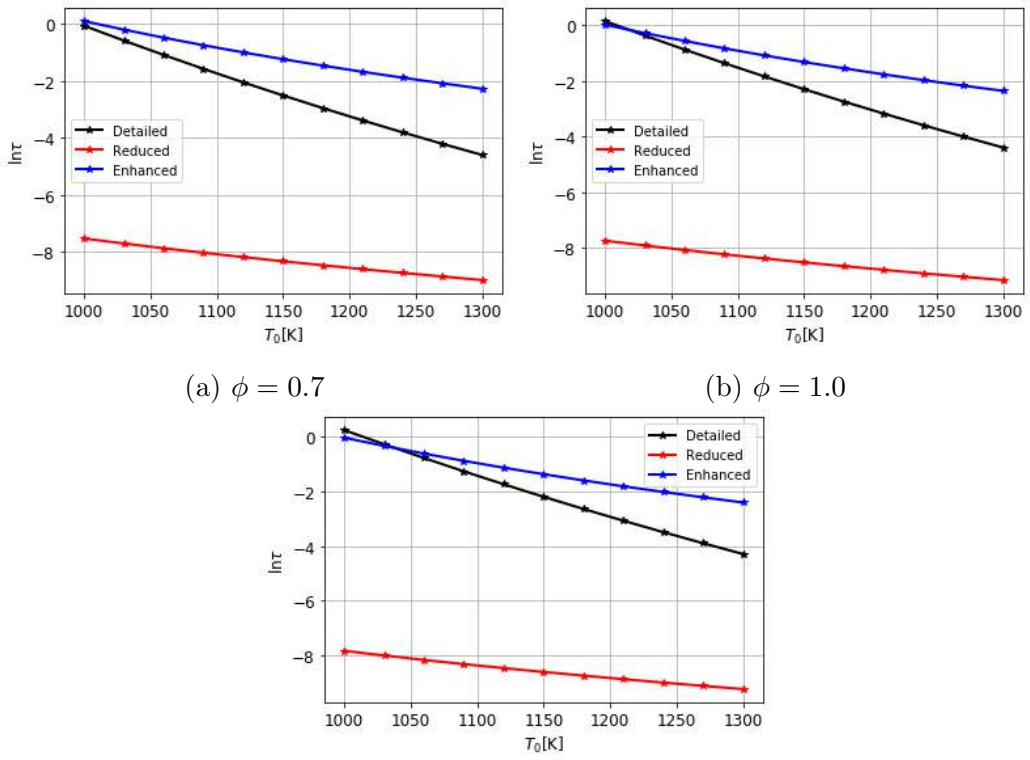

(a) $\phi = 0.7$ (b) $\phi = 1.0$

(c) $\phi = 1.2$

Figure 4.25: Autoignition delay time model predictions compared to GRI3.0: BG1 composition.

Also, the DNN discrepancy model is validated by predicting the autoignition delay time in different mixtures in which the fuels are the Baseline and the BG2 composition. Figures 4.26 and 4.27 show the predicted autoignition delay time using the multiplicative enhanced mechanism compared to the two-step mechanism and the full GRI3.0. The results indicate a good agreement between the enhanced model and the reference mechanism for different fuels at different equivalence ratios and a range of initial temperatures.

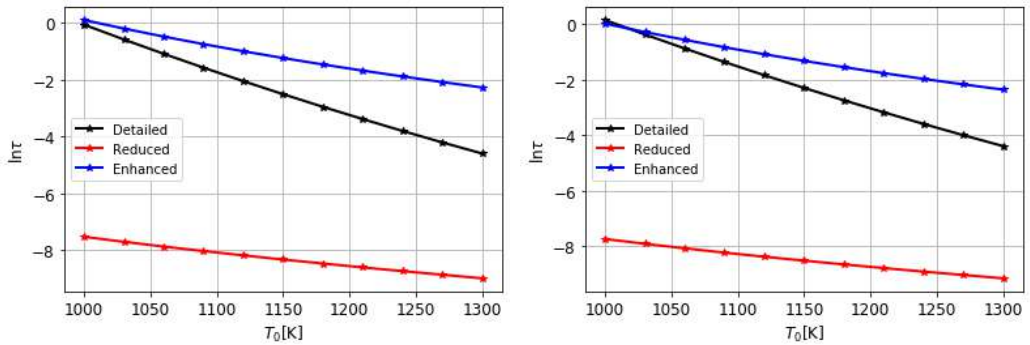

(a) $\phi = 0.7$ (b) $\phi = 1.0$

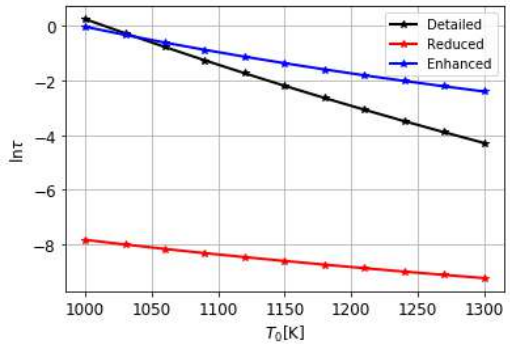

(c) $\phi = 1.2$

Figure 4.26: Autoignition delay time model predictions compared to GRI3.0: Baseline composition.

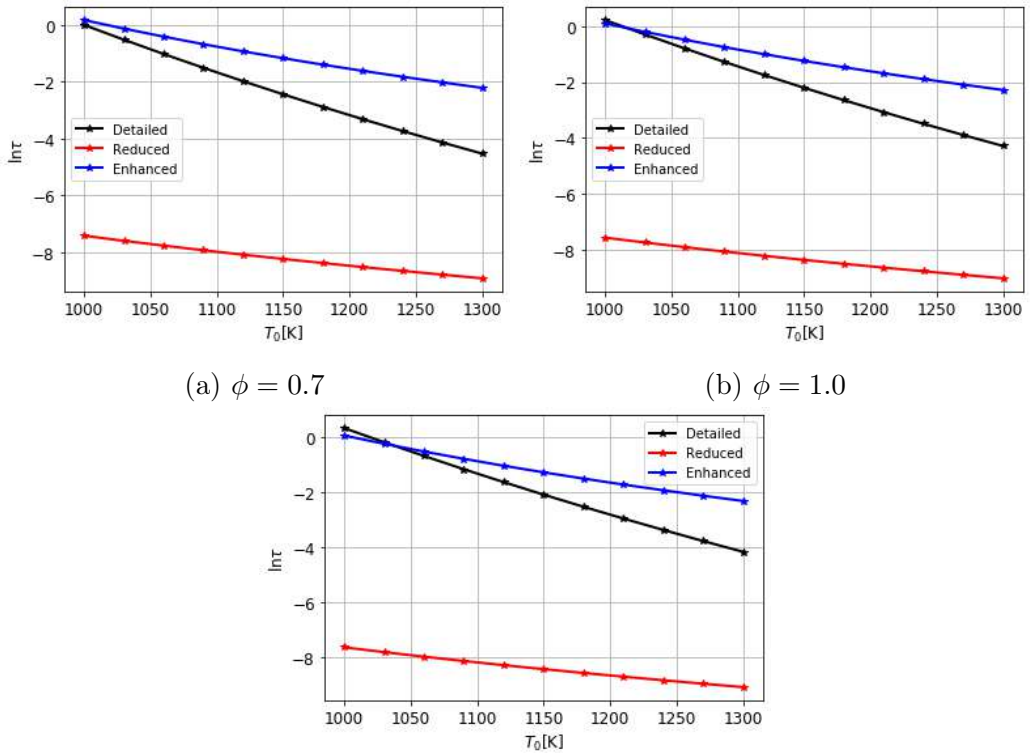

(a) $\phi = 0.7$ (b) $\phi = 1.0$

(c) $\phi = 1.2$

Figure 4.27: Autoignition delay time model predictions compared to GRI3.0: BG2 composition.

Next, the validation of the calibrated model is stressed showing the time evolution of methane mass fraction and temperature for mixtures in Table 4.1 at the stoichiometric condition and initial temperature equals 1050K. Figure 4.28 shows that embedding the model discrepancy as a multiplying factor predicts reliable results of the temperature distribution. Also, it is worth highlighting that the enhanced model predicts the autoignition delay times for the Baseline, BG1, and BG2 compositions with L_2 relative errors equal to 0.0739, 0.0743, and 0.0755, respectively. However, after the ignition process, the enhanced model returns unsatisfactory predictions of the burnt methane mass fractions. These results might be, partially, attributed to the lack of data covering the temporal evolution of the physicochemical properties in the learning process that uses only autoignition delay times as data.

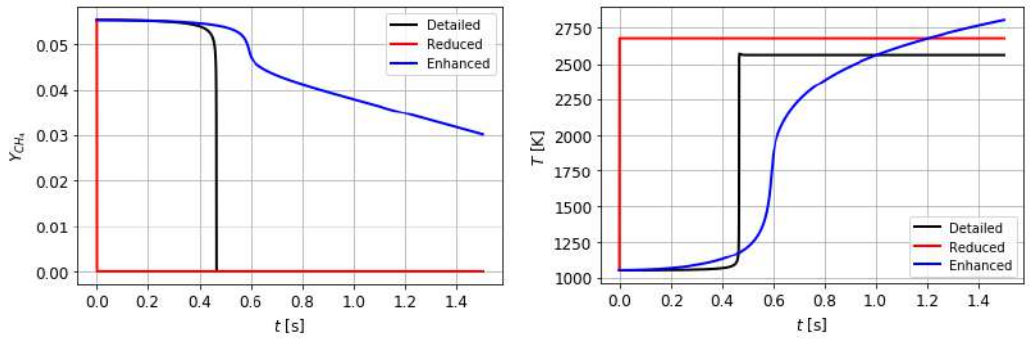

(a) Baseline - CH_4 mass fraction

(b) Baseline - Temperature

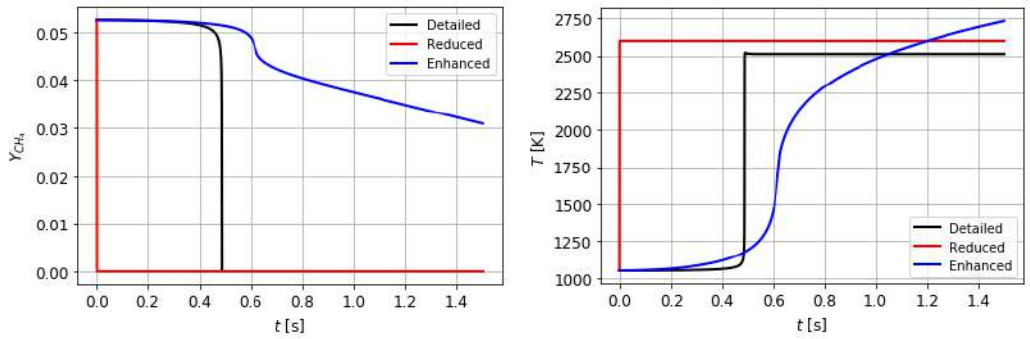

(c) BG1 - CH_4 mass fraction

(d) BG1 - Temperature

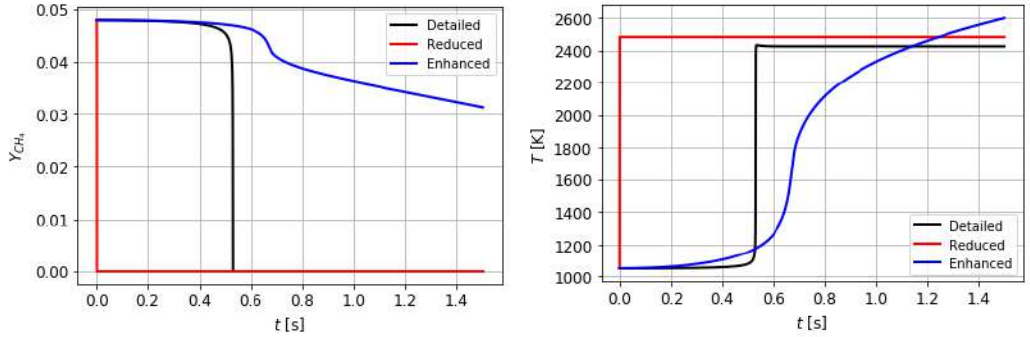

(e) BG2 - CH_4 mass fraction

(f) BG2 - Temperature

Figure 4.28: Temporal distributions of methane mass fraction and temperature predictions of the cases in Table 4.1.

Now, in an attempt to improve the ability of the enhanced model to predict the temporal evolution of physicochemical properties, more data is added for the learning process including the temporal evolution. More specifically, it is added to the training set fifty equally time-spaced points of the temporal evolution of the methane mass fraction and temperature for each operating condition. Also, it is important to point out that from the point of view of producing these data, there are no additional costs since they were produced previously during the autoignition delay times computation. However, it is expected that the training cost slightly increases. Then, the size of the training dataset is 5,555 evaluation points. Here, it is considered the solutions of the temporal evolutions for BG1 composition to build the training set. To better illustrate the new training dataset, Fig. 4.29 shows

the new training points for a specific operating condition given by $\phi = 1.0$ and $T_0 = 1030K$.

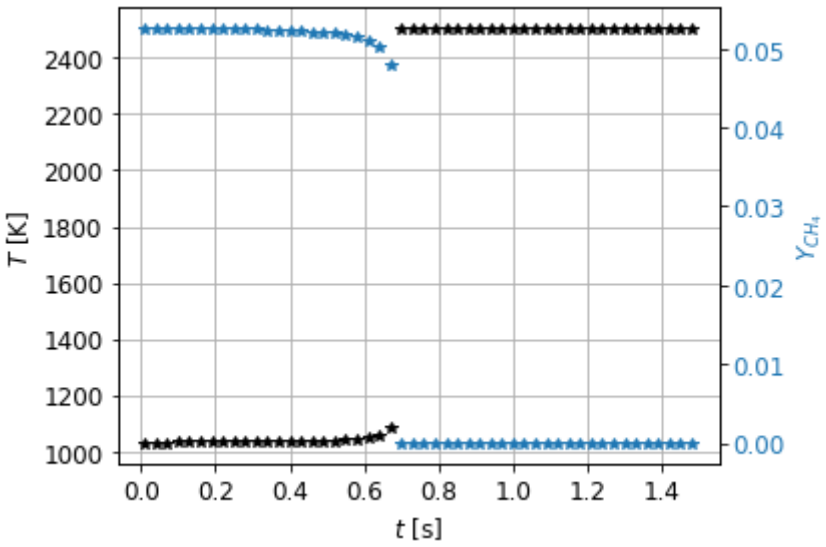

Figure 4.29: Training points for operating condition given by $\phi = 1.0$ and $T_0 = 1030K$: BG1 composition.

Figure 4.30 shows an improvement in the final calibrated model when compared to the previous calibrated model that uses only autoignition delay times as data for the training process. Also, the enhanced model computes the ignition process for Baseline, BG1, and BG2 compositions with L_2 relative errors of 0.0022, 0.0023 and 0.0025, respectively. Note that the final enhanced model can predict well the burnt methane mass fractions after the ignition process, i.e, full consumption of methane at the stoichiometric condition. However, it is verified a smooth transition between the unburnt and burnt mixtures. Furthermore, note much better predictions of the temporal evolutions of the temperature of all fuels using the final enhanced model.

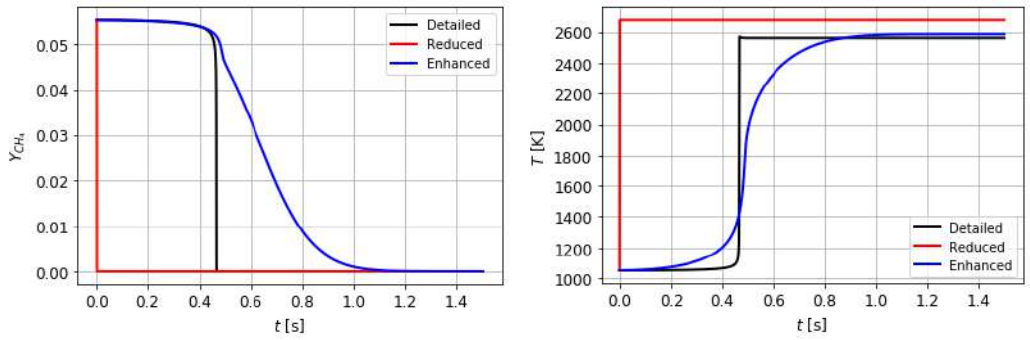

(a) Baseline - CH_4 mass fraction

(b) Baseline - Temperature

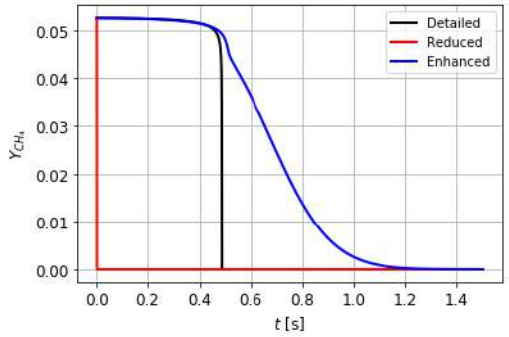

(c) BG1 - CH_4 mass fraction

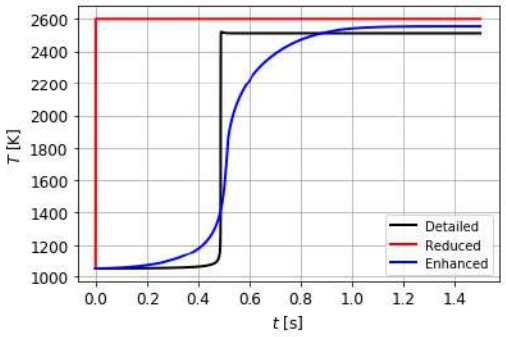

(d) BG1 - Temperature

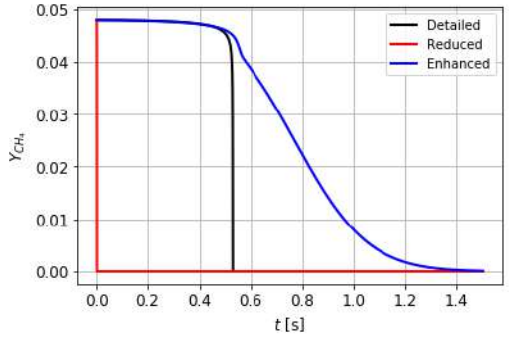

(e) BG2 - CH_4 mass fraction

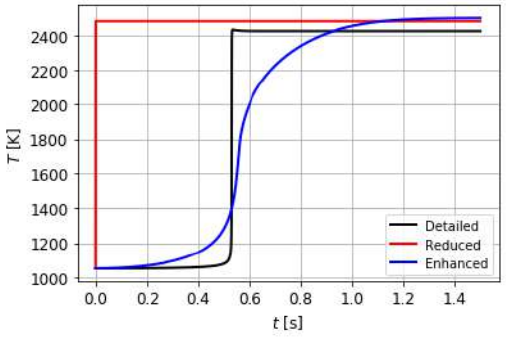

(f) BG2 - Temperature

Figure 4.30: Temporal distributions of methane mass fraction and temperature predictions of the cases in Table 4.1.

4.3.1 Embedding the neural network model discrepancy in the chemical kinetics parameters

Here, due to the intrusive nature of the embedded discrepancy approach, extrapolating the present approach to the 1D scenario falls on an implementation challenge, since the black-box, more specifically the Cantera software, have to be modified. To avoid the challenge of being intrusive in Cantera software, now it is proposed a calibration process similar to that done in the section 4.2, where the model discrepancy is embedded in the chemical kinetics parameters. However, instead of assuming a functional form for the model discrepancy as was done in 4.2, a neural network is built to capture an appropriate functional form for the model

correction.

More specifically, it is constructed a model discrepancy that acts as a correction term in the chemical kinetics parameters,

$$\mathbf{g} = \mathbf{g} \times (1 + \boldsymbol{\epsilon}) \tag{4.21}$$

where $\mathbf{g}$ represents the chemical kinetics parameter vector to be calibrated. The model discrepancy $\boldsymbol{\epsilon}$ is constructed using a neural network with the same architecture of the section 4.3. However, the neural network inputs are now the operating conditions given by the equivalence ratio and initial temperature. Furthermore, a tangent hyperbolic activation function (tanh) is employed [59] in all layers of the neural network. The tanh activation function imposes that the outputs of the neural network be in the range, $\boldsymbol{\epsilon} \in [-1, 1]$. So, for $\boldsymbol{\epsilon} = 0$, $\mathbf{g}$ represents the chemical kinetics parameters vector of the original reduced mechanism. Also, such imposition ensures physical constraints that the pre-exponential factor in the Arrhenius law is strictly positive. Moreover, for $\boldsymbol{\epsilon} = -1$, the reaction is suppressed in the reduced mechanism.

As was done in section 4.2, the pre-exponential factor and the activation energy of the irreversible reaction in the 2S-CM2 scheme are calibrated. Also, in the learning process, the same optimization steps done in the previous section are followed, as well as the same training dataset composed by the autoignition delay times and temporal evolution of key quantities. Figure 4.31 shows that the enhanced model improves the capacity of the reduced model to predict the autoignition process. The enhanced model computes the autoignition process for Baseline, BG1, and BG2 compositions with L_2 relative errors of 0.2230, 0.1960, and 0.1453, respectively.

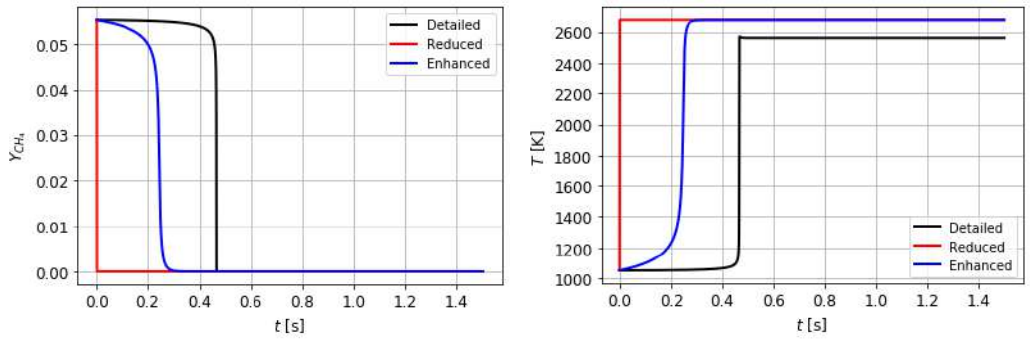

(a) Baseline - CH_4 mass fraction

(b) Baseline - Temperature

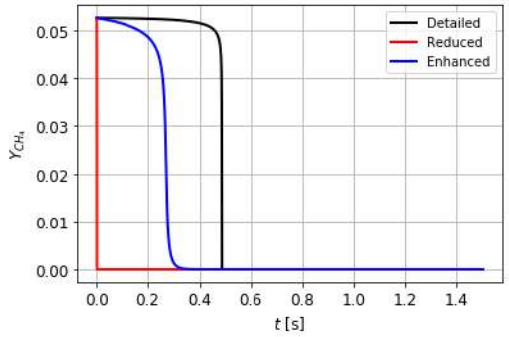

(c) BG1 - CH_4 mass fraction

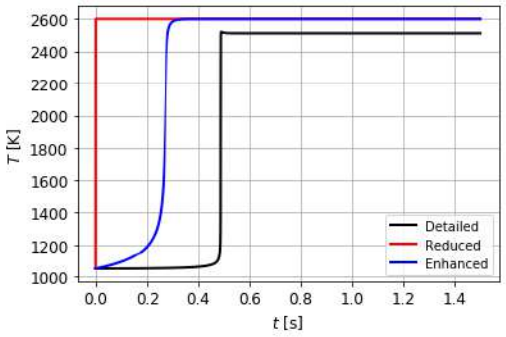

(d) BG1 - Temperature

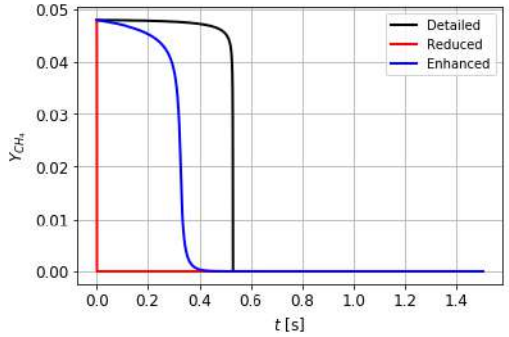

(e) BG2 - CH_4 mass fraction

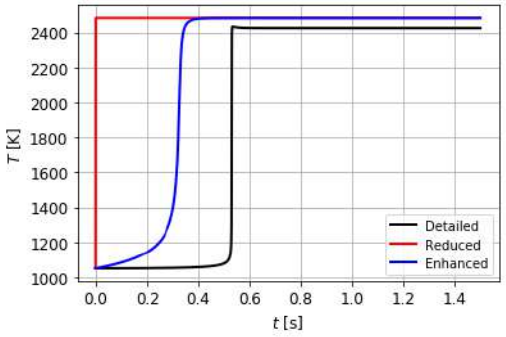

(f) BG2 - Temperature

Figure 4.31: Temporal distributions of methane mass fraction and temperature predictions of the cases in Table 4.1.

After the validation process, the learning process is extrapolated to the 1-D scenario involving steady-state laminar flames. Here, the aim is to assess how well the enhanced model recovers the flame properties, such as flame speed, flame thickness, adiabatic temperature, and burned molar fractions of CO and CO_2. The flame properties for the Baseline, BG1 and BG2 compositions predicted by the enhanced model are shown in Figs. 4.32, 4.33 and 4.34. These results indicate that after calibration for the 0D reactor problem, the enhanced 2S-CM2 model can still capture the major combustion products and adiabatic flame temperatures in good agreement with the original mechanism. However, the flame speed is underestimated while the flame thickness is overestimated, mainly in lean and stoichiometric conditions.

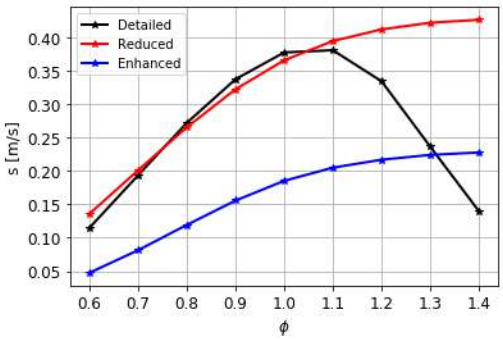

(a) Baseline flame speed

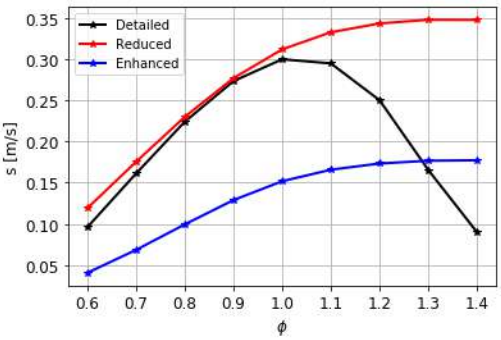

(b) BG1 flame speed

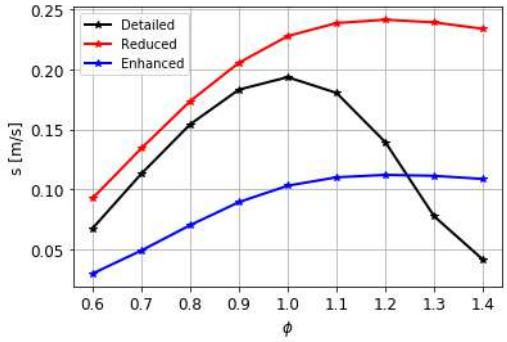

(c) BG2 flame speed

Figure 4.32: Flame speed predictions for the biogas-air premixed flame of the Tab. 4.1 at $p = 1$ bar and $T_0 = 300K$.

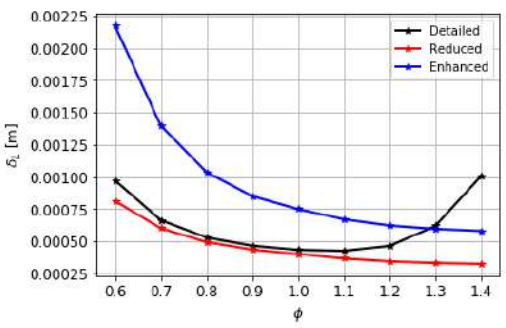

(a) Baseline flame thickness

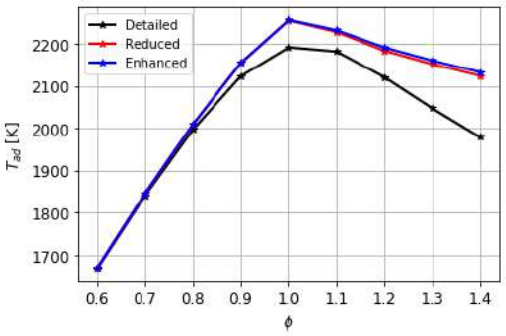

(b) Baseline adiabatic flame temperature

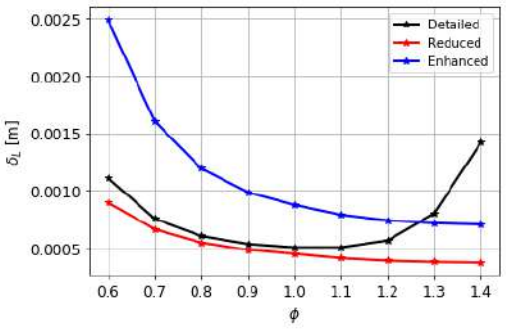

(c) BG1 flame thickness

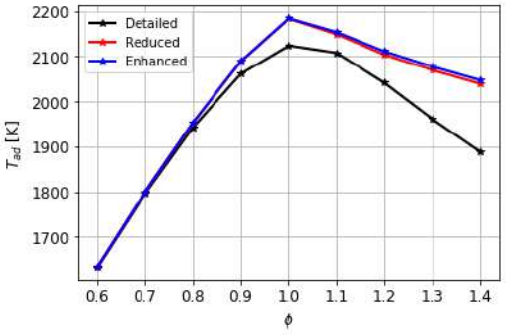

(d) BG1 adiabatic flame temperature

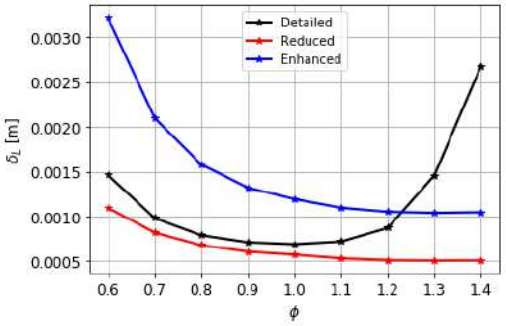

(e) BG2 flame thickness

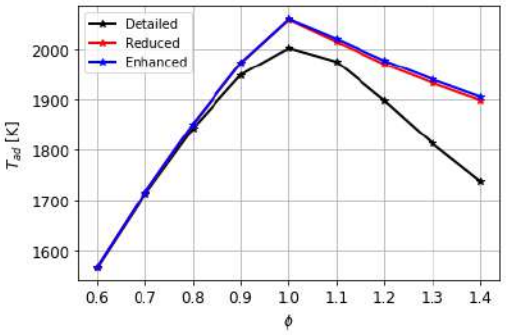

(f) BG2 adiabatic flame temperature

Figure 4.33: Flame thickness and adiabatic temperature predictions for the biogas-air premixed flame of the Tab. 4.1 at $p = 1$ bar and $T_0 = 300K$.

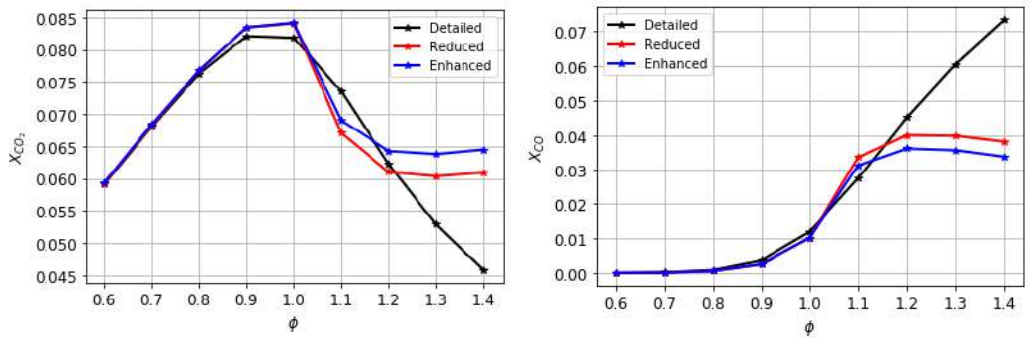

(a) Baseline CO_2 burned molar fraction (b) Baseline CO burned molar fraction

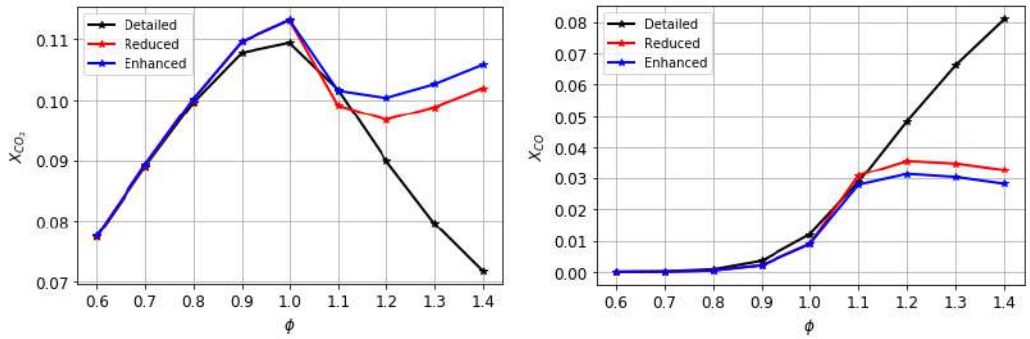

(c) BG1 CO_2 burned molar fraction (d) BG1 CO burned molar fraction

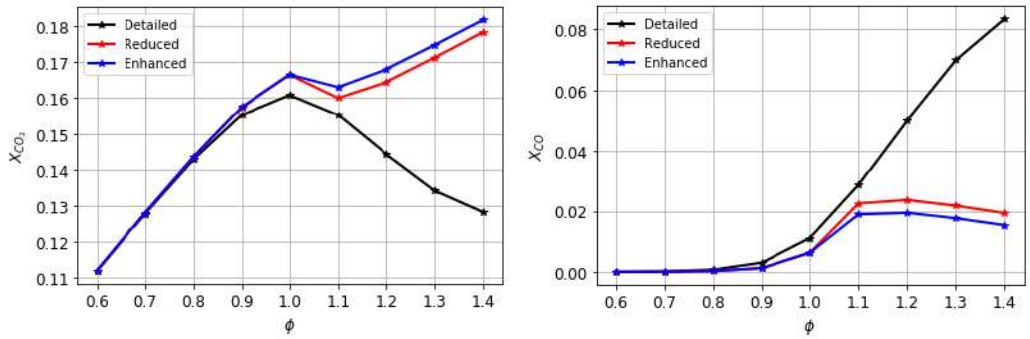

(e) BG2 CO_2 burned molar fraction (f) BG2 CO burned molar fraction

Figure 4.34: Burned molar fractions predictions for the biogas-air premixed flame of the Tab. 4.1 at $p = 1$ bar and $T_0 = 300K$.

Aiming to recover the correct behavior of the flame properties, now is followed the studies carried out in the section 4.2.2, where an empirical pre-exponential factor adjustment is employed. More specifically, it is constructed the model discrepancy term taking into account of the PEA to improve the predictability of the reduced mechanism to 0D and 1D problems. Also, the same pre-exponential factor adjustment function used previously is employed here, see section 4.2.2.

The predictions associated with the enhanced model are shown in Fig. 4.35. The results show that that the enhanced model can predict satisfactorily well the temporal evolutions of the methane mass fraction, and temperature for different composition scenarios compared to the full GRI3.0 mechanism. Also, it is computed the L_2 relative errors of the ignition process and verified that the enhanced model

returns the ignition predictions for the Baseline, BG1 and BG2 compositions with an accuracy of 0.0679, 0.0481, 0.0178, respectively.

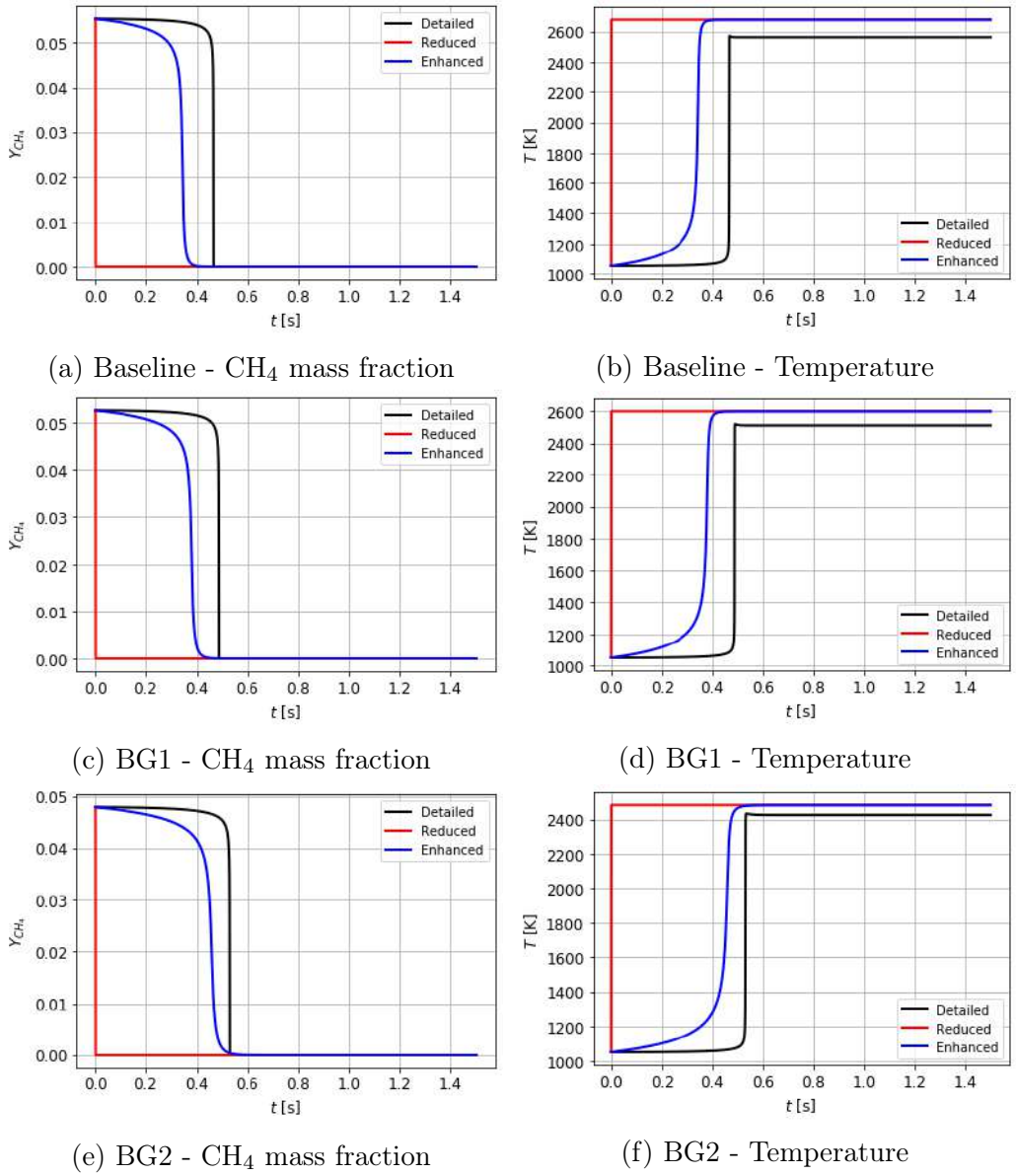

(a) Baseline - CH_4 mass fraction

(b) Baseline - Temperature

(c) BG1 - CH_4 mass fraction

(d) BG1 - Temperature

(e) BG2 - CH_4 mass fraction

(f) BG2 - Temperature

Figure 4.35: Temporal distributions of methane mass fraction and temperature predictions of the cases in Table 4.1.

Now, the enhanced model with the pre-adjustment factor is extrapolated to the 1-D scenario. The flame properties for the freely propagating laminar premixed flames of methane and biogas are shown in Figs. 4.36, 4.37 and 4.38. It can be seen that the flame speed and flame thickness are in good agreement with the full GRI3.0 model, but the flame speed is slightly underestimated near stoichiometric regions for Baseline and BG1 compositions, while it is slightly overestimated in rich regions for BG2 composition. Also, the burnt gas temperature and the major combustion products are in good agreement with the original reduced model. These results

suggest that the enhanced model has been successfully extended to describe flame propagation and autoignition scenarios. Furthermore, it is worth highlighting that the training process is relatively cheap, much cheaper than the previous probabilistic calibration approach. More specifically, the present approach is on the minute scale while the probabilistic approach takes hours.

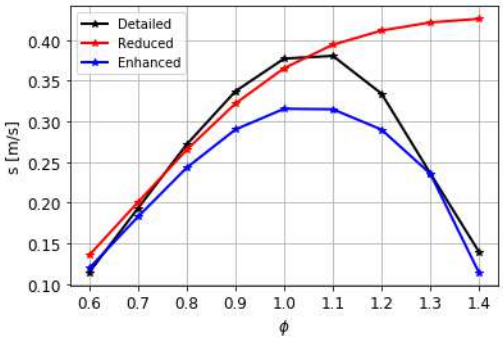

(a) Baseline flame speed

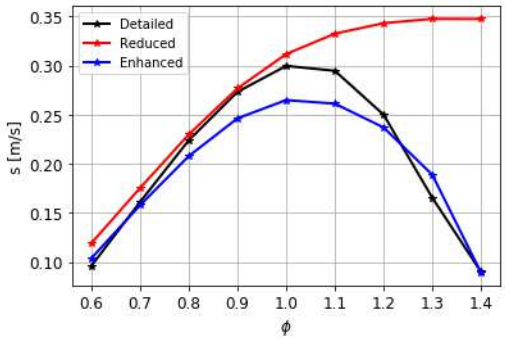

(b) BG1 flame speed

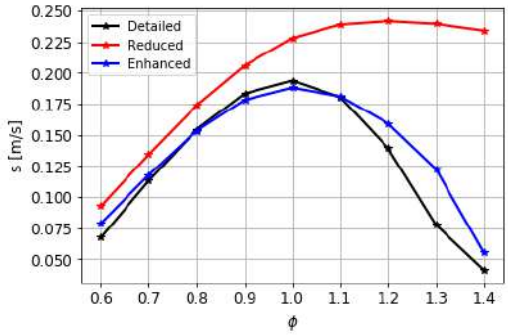

(c) BG2 flame speed

Figure 4.36: Flame speed predictions for the biogas-air premixed flame of the Tab. 4.1 at $p = 1$ bar and $T_0 = 300K$.

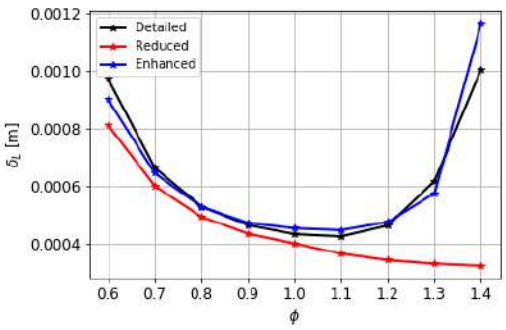

(a) Baseline flame thickness

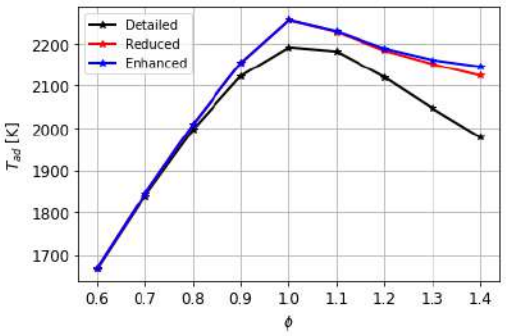

(b) Baseline adiabatic flame temperature

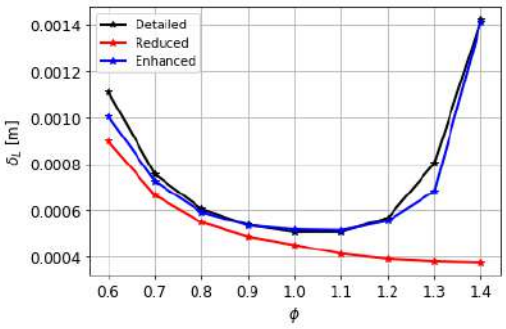

(c) BG1 flame thickness

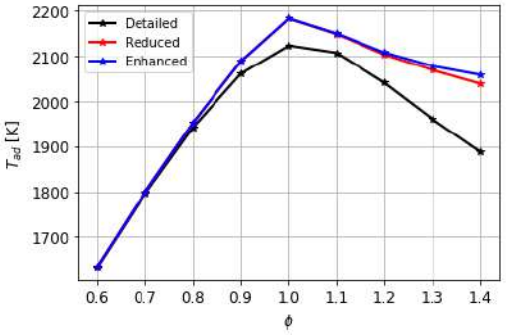

(d) BG1 adiabatic flame temperature

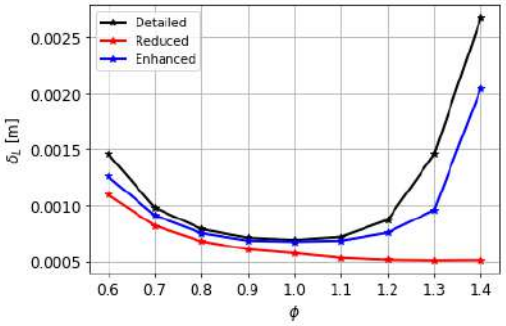

(e) BG2 flame thickness

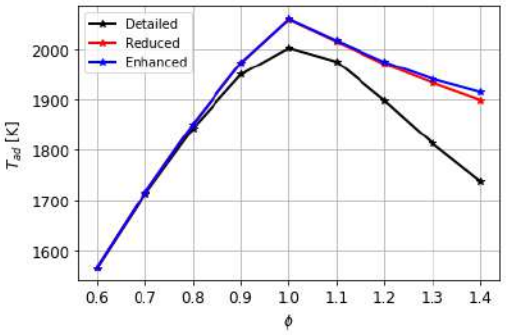

(f) BG2 adiabatic flame temperature

Figure 4.37: Flame thickness and adiabatic temperature predictions for the biogas-air premixed flame of the Tab. 4.1 at $p = 1$ bar and $T_0 = 300K$.

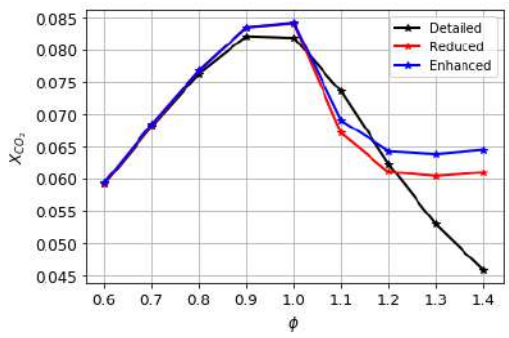

(a) Baseline CO_2 burned molar fraction

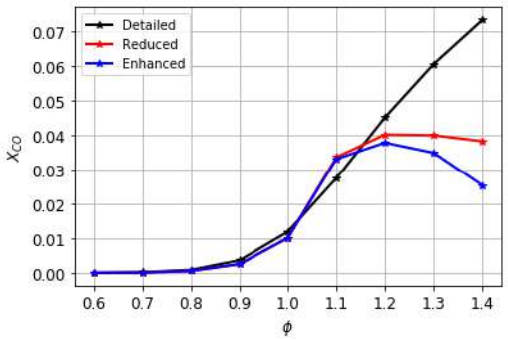

(b) Baseline CO burned molar fraction

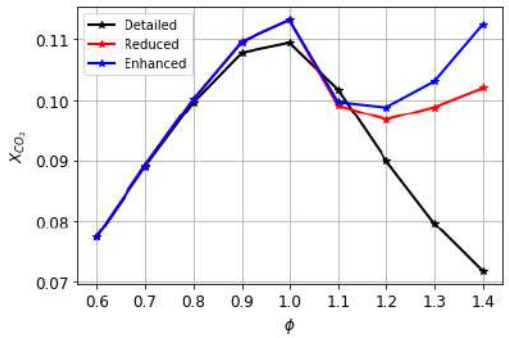

(c) BG1 CO_2 burned molar fraction

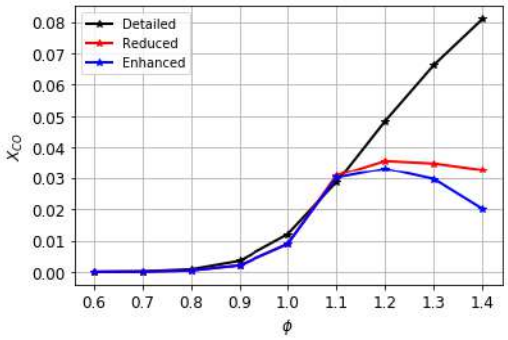

(d) BG1 CO burned molar fraction

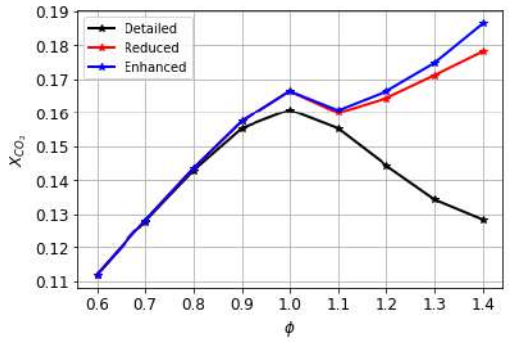

(e) BG2 CO_2 burned molar fraction

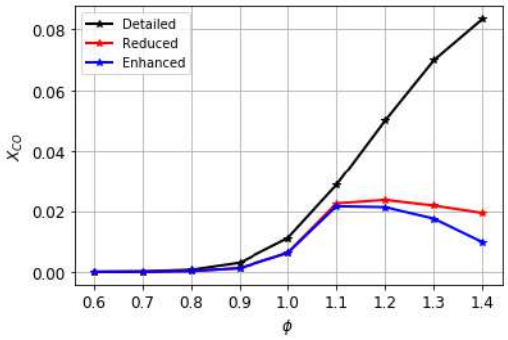

(f) BG2 CO burned molar fraction

Figure 4.38: Burned molar fractions predictions for the biogas-air premixed flame of the Tab. 4.1 at $p = 1$ bar and $T_0 = 300K$.

Chapter 5

Final Comments

The present study addresses the critical problem of model inadequacy that affects nearly all physics-based computational models. Here, the attention goes to the impact of employing reduced kinetic mechanisms on premixed combustion of biogas/methane-air mixtures. In such cases, unsatisfactory agreement in the predictions of key quantities such as autoignition delay time, flame propagation, and emissions are frequently observed when compared with experiments or high-fidelity chemical kinetics models. The model discrepancy might be responsible for significant bias in the model predictions, especially when involves biogas with large amounts of CO_2 in its composition, which requires some efforts to fix it.

The uncertainties produced by using simplified closure models, the reduced kinetics, is tackled here, using probabilistic and deterministic perspectives, by using Bayesian and machine learning tools. More specifically, to address this challenge, the present work introduces different approaches to understand and compute uncertainties on the computation of the autoignition delay time prediction or laminar flames characteristics.

In a UQ probabilistic perspective, it is proposed two models based on embedding the model discrepancy in Arrhenius parameters of the most sensitive reaction. The calibrated model matched well the detailed model data, consequently, produced reasonably small predictive error bars for the autoignition delay time predictions. Furthermore, the calibrated model is extrapolated for the flame scenario, showing the advantage of the embedded discrepancy approach proposed in [27], allowing that the calibrated mechanism be propagated through different scenarios to predict the related uncertainty of the flame properties. This form type of extrapolation of the calibration process is not explored by Najm et al. [27, 47, 102]. Here, this approach is presented as one contribution of the present work. It is verified in the first calibration experiment that the flame characteristics can not be reproduced, at rich conditions, using the enhanced reduced mechanism. However, the applicability range of the reduced model can be extended calibrating it with a pre-exponential

adjustment factor.

As mentioned before, a key aspect in model embedding is to allow a consistent use of the calibrated model for situations of more practical interest. For instance, to evaluate the variability of the flame speed and flame thickness in different operational conditions, a deep neural network surrogate to the original model was developed to alleviate the large computational burden associated with uncertainty quantification employing Monte Carlo algorithms. The surrogate demonstrate be a robust and cost effective tool, predicting accurate approximations of the flame properties. The results showed high variability on the flame properties due to the fluctuations of Arrhenius parameters especially those near the low bound for leaner mixtures, which entails a high degree of uncertainty. That might be attributed to the burning conditions near flammability, which bears the potential to amplify the propagated uncertainties.

Also, it is proposed a deep neural model discrepancy approach to improve the ability of the low fidelity models to produce reliable predictions of the combustion process. Such an approach has revealed to be very flexible and able to generalize for several forms to embed the model discrepancy. More specifically, it was proposed an approach in which the model error is embedded in the temporal evolution of chemical species concentrations. Moreover, a model discrepancy approach in which the model discrepancy is embedded in the chemical kinetics parameters was proposed. However, differently, to the probabilistic embedded approach, a neural network is built to capture an appropriate functional form for the model correction. Both approaches have shown to be very promising in modeling the model discrepancy. Furthermore, it also serves as a good test for employing a combination of supervised machine learning techniques with low fidelity models to raise their the predictability and construct useful tools to support computational simulation of complex systems such as turbulent combustion.

Those studies demonstrated the deficiency of the 2-step mechanism when employed outside of the original applicability limits, and the efficacy of Bayesian and machine learning tools to improve the modeling accuracy. Also, the results have shown the benefit of the embedding the model discrepancy in the key parameters of the model. The key advantage of that method is that it offers predictions, to any model output variable, that include structural uncertainty due to the simple form of the reduced chemical kinetics. Furthermore, the embedded approach allows extrapolating the enhanced model for different scenarios.

Future studies can be focused on pollutant formation predictions, where more complex chemical kinetic models will be needed. Also, extrapolating the machine learning model discrepancy approach to more complex and challenging simulations as found in turbulent combustion. Moreover, extending the application of machine

learning techniques to practical combustion systems, such as enhancing efficiency and emissions control [103], and modeling engine operating characteristics [104, 105].

Also, future research directions can be focused on the construction of efficiency surrogate models using physics aware neural networks [2, 55–58, 60–62, 86, 106] to deal with uncertainties in model inputs or parameters of such high demanding computational combustion simulations, allowing to provide a link between sources of uncertainties and their impacts on the QoI's of the computational model. This link can be used to mitigate possible negative impacts of these sources of uncertainties and obtain better, cheaper and more robust predictions. Initial efforts in that direction can be seen in [107], that is, in the construction of deep learning surrogate models to quantify uncertainties in seismic imaging.

References

[1] GALAGALI, N., MARZOUK, Y. M. "Bayesian inference of chemical kinetic models from proposed reactions", Chem. Eng. Science, v. 123, pp. 170–190, 2015.

[2] TRIPATHY, R., BILIONIS, I. "Deep uq: Learning deep neural network surrogate models for high dimensional uncertainty quantification", Journal of Computational Physics, v. 375, pp. 565–588, 2018.

[3] WESTBROOK, C. K., MIZOBUCHI, Y., POINSOT, T. J., et al. "Computational combustion", Proceedings of the Combustion Institute, v. 30, n. 1, pp. 125 – 157, 2005. ISSN: 1540-7489. doi: https://doi.org/10.1016/j.proci.2004.08.275. Disponível em: <http://www.sciencedirect.com/science/article/pii/S0082078404003340>.

[4] WILLIANS, F. A. Combustion Theory: The Fundamental Theory of Chemically Reacting Flow Systems. The Benjamin/Cummings Publishing Company, Inc, 1985.

[5] POINSOT, T., VEYNANTE, D. Theoretical and Numerical Combustion. Second ed. , R.T. Edwards, Inc, 2005.

[6] VERSTAPPEN, R. W. C. P., VELDMAN, A. E. P. "Symmetry-preserving discretization of turbulent flow", Journal of Computational Physics, v. 187, n. 1, pp. 343–368, 2003.

[7] AVDIC, A., KUENNE, G., DI MARE, F., et al. "LES combustion modeling using the Eulerian stochastic field method coupled with tabulated chemistry", Combustion and Flame, v. 175, pp. 201–219, 2017.

[8] VEYNANTE, D., VERVISCH, L. "Turbulent Combustion Modeling", Prog. Energy Combust. Sci., v. 28, pp. 193–266, 2002.

[9] CHEN, J., CHOUDHARY, A., SUPINSKI, B. D., et al. "Terascale direct numerical simulations of turbulent combustion using S3D", Comput. Sci. Discov., v. 2, n. 1, 2009.

[10] WESTBROOK, C. K., DRYER, F. L. "Simplified reaction mechanisms for the oxidation of hydrocarbon fuels in flames", Combustion Science and Technology, v. 27, pp. 31–43, 1981.

[11] WILLIAMS, F. "Detailed and reduced chemistry for hydrogen autoignition", J. of Loss Prevention in the Process Industries, v. 21, pp. 131–135, 2008.

[12] BOIVIN, P., JIMENEZ, C., SANCHEZ, A. L., et al. "A four step reduced mechanism for syngas combustion", Combustion and Flame, v. 158, 2011.

[13] MORRISON, R. E., OLIVER, T. A., MOSER, R. D. "Representing Model Inadequacy: A Stochastic Operator Approach", SIAM/ASA Journal on Uncertainty Quantification, v. 6, n. 2, pp. 457–496, 2018. doi: 10.1137/16M1106419. Disponível em: <https://doi.org/10.1137/16M1106419>.

[14] MUELLER, M. E., IACCARINO, G., PITSCH, H. "Chemical kinetic uncertainty quantification for Large Eddy Simulation of turbulent nonpremixed combustion", Proceedings of the Combustion Institute, 2012.

[15] NAJM, H. N., DEBUSSCHERE, B. J., MARZOUK, Y. M., et al. "Uncertainty quantification in chemical systems", International Journal for Numerical Methods in Engineering, v. 80, n. 6-7, pp. 789–814, 2009. doi: 10.1002/nme.2551. Disponível em: <https://onlinelibrary.wiley.com/doi/abs/10.1002/nme.2551>.

[16] REAGAN, M. T., NAJM, H. N., GHANEMB, R. G., et al. "Uncertainty quantification in reacting-flow simulations through non-intrusive spectral projection", Combustion and Flame, v. 132, pp. 545–555, 2003.

[17] FISCHER, M., JIANG, X. "A chemical kinetic modelling study of the combustion of $CH_4 - CO - H_2 - CO_2$ fuel mixtures", Combustion and Flame, v. 167, pp. 274–293, 2016.

[18] WEILAND, P. "Biogas production: current state and perspectives", Appl. Microbiol. Biotechnol., v. 85, pp. 849–860, 2010.

[19] FISCHER, M., JIANG, X. "An investigation of the chemical kinetics of biogas combustion", Fuel, v. 150, pp. 711–720, 2015. Disponível em: <http://dx.doi.org/10.1016/j.fuel.2015.01.085>.

[20] KAPPEL, C., LUTHER, K., TROE, J. "Shock wave study of the unimolecular dissociation of H2O2 in its falloff range and of its secondary reactions", Physical Chemistry Chemical Physics, v. 4, pp. 4392–4398, 2002. doi:

10.1039/B204364E. Disponível em: <http://dx.doi.org/10.1039/B204364E>.

[21] TSANG, W., HAMPSON, R. F. "Chemical Kinetic Data Base for Combustion Chemistry. Part I. Methane and Related Compounds", Journal of Physical and Chemical Reference Data, v. 15, 1986. Disponível em: <https://doi.org/10.1063/1.555759>.

[22] BAULCH, D. L., COBOS, C. J., COX, R. A., et al. "Evaluated Kinetic Data for Combustion Modelling", Journal of Physical and Chemical Reference Data, v. 21, 1992. Disponível em: <https://doi.org/10.1063/1.555908>.

[23] MORRISON, R. E. "Embedded discrepancy operators in reduced models of interacting species", arXiv preprint arXiv:1910.08191, 2019.

[24] MIKI, M., PRUDENCIO, E. E., CHEUNG, S. H., et al. "Using Bayesian analysis to quantify uncertainties in the $H + O2 => OH + O$ reaction", Combustion and Flame, v. 160, pp. 861–869, 2013.

[25] MIKI, M., PRUDENCIO, E. E., CHEUNG, S. H., et al. "Uncertainty quantification and robust predictive system analysis for high temperature kinetics of $HCN/O2/Ar$ mixture", Chemical Physics, v. 475, pp. 136–152, 2016.

[26] MIKI, K., CHEUNG, S. H., PRUDENCIO, E. E., et al. "Bayesian uncertainty quantification of recent shock tube determinations of the rate coefficient of reaction H + O2 OH + O", International Journal of Chemical Kinetics, v. 44, n. 9, pp. 586–597, 2012. doi: 10.1002/kin.20736. Disponível em: <https://onlinelibrary.wiley.com/doi/abs/10.1002/kin.20736>.

[27] SARGSYAN, K., NAJM, H. N., GHANEM, R. "On the Statistical Calibration of Physical Models", International Journal for Chemical Kinetics, v. 47, n. 4, pp. 246–276, 2015.

[28] OLIVER, T. A., TEREJANU, G., SIMMONS, C. S., et al. "Validating predictions of unobserved quantities", Computer Methods in Applied Mechanics and Engineering, v. 283, pp. 1310 – 1335, 2015. ISSN: 0045-7825. doi: https://doi.org/10.1016/j.cma.2014.08.023. Disponível em: <http://www.sciencedirect.com/science/article/pii/S004578251400293X>.

[29] MOSER, R. D., OLIVER, T. A. "Validation of Physical Models in the Presence of Uncertainty". In: Ghanem R., Higdon D., Owhadi H. (eds) Handbook of Uncertainty Quantification. Springer, Cham, 2015. doi: https://doi.org/10.1007/978-3-319-11259-6_2-1.

[30] CHEUNG, S. H., OLIVER, T. A., PRUDENCIO, E. E., et al. "Bayesian uncertainty analysis with applications to turbulence modeling", Reliability Engineering & System Safety, v. 96, n. 9, pp. 1137 – 1149, 2011. ISSN: 0951-8320. doi: https://doi.org/10.1016/j.ress.2010.09.013. Disponível em: <http://www.sciencedirect.com/science/article/pii/S0951832011000664>. Quantification of Margins and Uncertainties.

[31] J., B., T., P. "Examination of simplified mechanisms of CH_4 combustion in N_2/O_2 and CO_2/O_2 atmosphere using mathematical modeling", Archivum Combustionis, v. 31, pp. 255–262, 2011.

[32] KEE, R. J., COLTRIN, M. E., GLARBORG, P., et al. Chemically reacting flow: theory, modeling, and simulation. 2nd ed. , John Wiley & Sons, 2017.

[33] GLASSMAN, I., YETTER, R. A. Combustion. Fourth ed. , Elsevier Inc., 2008.

[34] BIBRZYCKI, J., POINSOT, T. "Reduced chemical kinetic mechanisms for methane combustion in O2/N2 and O2/CO2 atmosphere", Disponível em: <http://www.cerfacs.fr/cfdbib/repository/WN_CFD_10_17.pdf>.

[35] MCBRIDE, B. J., GORDON, S., RENO, M. A. Coefficients for Calculating Thermodynamic and Transport Properties of Individual Species. NASA Technical Memorandum 4513, 1993.

[36] HOUSE, J. E. Principles of Chemical Kinetics. 2nd ed. , Academic Press, 2007.

[37] LAIDLER, K. J. Chemical Kinetics. 3rd ed. , Prentice Hall, 1987.

[38] SMOOKE, M. D., GIOVANGIGLI, V. "Premixed and nonpremixed test problem results. In: Smooke M.D. (eds) Reduced Kinetic Mechanisms and Asymptotic Approximations for Methane-Air Flames", Lecture Notes in Physics, v. 384, 1991.

[39] GÖVERT, S., MIRA, D., KOK, J., et al. "Turbulent combustion modelling of a confined premixed jet flame including heat loss effects using tabulated chemistry", Applied Energy, v. 156, pp. 804–815, 2015. Disponível em: <https://doi.org/10.1016/j.apenergy.2015.06.031>.

[40] GOODWIN, D. G., SPETH, R. L., MOFFAT, H. K., et al. "Cantera: An Object-oriented Software Toolkit for Chemical Kinetics, Thermodynamics, and Transport Processes". https://www.cantera.org, 2018. Version 2.4.0.

[41] FIORINA, B., VICQUELIN, R., AUZILLON, P., et al. "A filtered tabulated chemistry model for LES of premixed combustion", Combustion and Flame, v. 157, n. 3, pp. 465–475, 2010.

[42] HOLLAND, J. R., BAEDER, J. D., DURAISAMY, K. "Towards Integrated Field Inversion and Machine Learning With Embedded Neural Networks for RANS Modeling". In: AIAA Scitech 2019 Forum. doi: 10.2514/6.2019-1884. Disponível em: <https://arc.aiaa.org/doi/abs/10.2514/6.2019-1884>.

[43] FREITAS, R. S., ROCHINHA, F. A., MIRA, D., et al. "Parametric and model uncertainties induced by reduced order chemical mechanisms for biogas combustion", Chemical Engineering Science, v. 227, pp. 115949, 2020. ISSN: 0009-2509. doi: https://doi.org/10.1016/j.ces.2020.115949. Disponível em: <http://www.sciencedirect.com/science/article/pii/S0009250920304814>.

[44] KENNEDY, M. C., O'HAGAN, A. "Bayesian calibration of computer models", Journal of the Royal Statistical Society: Series B, v. 63, n. 3, pp. 425–464, 2001.

[45] BERNARDO, J., SMITH, A. Bayesian Theory. Wiley Series in Probability and Statistics. John Wiley & Sons Ld, Chichester, England, 2000.

[46] CARLIN, B. P., LOUIS, T. A. Bayesian Methods for Data Analysis. Chapman and Hall/CRC, Boca Raton, FL, 2011.

[47] HAKIM, L., LACAZE, G., KHALIL, M., et al. "Probabilistic parameter estimation in a 2-step chemical kinetics model for n-dodecane jet autoignition", Combustion Theory and Modelling, v. 22, n. 3, pp. 446–466, 2018. doi: 10.1080/13647830.2017.1403653. Disponível em: <https://doi.org/10.1080/13647830.2017.1403653>.

[48] WIENER, N. "The homogeneous chaos", Amer. J. Math., v. 60, n. 4, pp. 897–936, 1938.

[49] ZIO, S., DA COSTA, H. F., GUERRA, G. M., et al. "Bayesian assessment of uncertainty in viscosity closure models for turbidity

currents computations", Computer Methods in Applied Mechanics and Engineering, v. 342, pp. 653 – 673, 2018. ISSN: 0045-7825. doi: https://doi.org/10.1016/j.cma.2018.08.023. Disponível em: <http://www.sciencedirect.com/science/article/pii/S004578251830416X>.

[50] SMITH, R. C. Uncertainty Quantification: Theory, Implementation, and Applications. SIAM Computational Science and Engineering Series, 2014.

[51] GILKS, W. R., RICHARDSON, S., SPIEGELHALTER, D. J. Markov Chain Monte Carlo in Practice. Chapman & Hall, London, 1996.

[52] COWLES, M. K., CARLIN, B. P. "Markov chain Monte Carlo convergence diagnostics: A comparative review", American Statistical Association, v. 91, n. 434, pp. 883–904, June 1996.

[53] KAIPIO, J., SOMERSALO, E. "Statistical and Computational Inverse Problems", Applied Mathematical Sciences, v. 160, 2005. doi: 10.1007/b138659.

[54] CALVETTI, D., SOMERSALO, E. Introduction to Bayesian Scientific Computing. Springer, New York, 2007.

[55] ZHU, Y., ZABARAS, N. "Bayesian deep convolutional encoder-decoder networks for surrogate modeling and uncertainty quantification", Journal of Computational Physics, v. 366, pp. 415–447, 2018. Disponível em: <https://doi.org/10.1016/j.jcp.2018.04.018>.

[56] MO, S., ZHU, Y., ZABARAS, N., et al. "Deep convolutional encoder-decoder networks for uncertainty quantification of dynamic multiphase flow in heterogeneous media", Water Resources Research, v. 55, pp. 703–728, 2019.

[57] GENEVA, N., ZABARAS, N. "Quantifying model form uncertainty in Reynolds-averaged turbulence models with Bayesian deep neural networks", Journal of Computational Physics, v. 383, pp. 125–147, 2019.

[58] ZHU, Y., ZABARAS, N., KOUTSOURELAKIS, P., et al. "Physics-constrained deep learning for high-dimensional surrogate modeling and uncertainty quantification without labeled data", Journal of Computational Physics, v. 394, pp. 56–81, 2019.

[59] GOODFELLOW, I., BENGIO, Y., COURVILLE, A. Deep Learning. MIT Press, 2016.

[60] RAISSI, M., PERDIKARIS, P., KARNIADAKIS, G. "Physics-informed neural networks: A deep learning framework for solving forward and inverse problems involving nonlinear partial differential equations", Journal of Computational Physics, v. 378, pp. 686 – 707, 2019. ISSN: 0021-9991. doi: https://doi.org/10.1016/j.jcp.2018.10.045. Disponível em: <http://www.sciencedirect.com/science/article/pii/S0021999118307125>.

[61] WILLARD, J., JIA, X., XU, S., et al. "Integrating Physics-Based Modeling with Machine Learning: A Survey", 2020. doi: arXiv:2003.04919.

[62] HAGHIGHAT, E., RAISSI, M., MOURE, A., et al. "A deep learning framework for solution and discovery in solid mechanics: linear elasticity". 2020.

[63] FERRERO, A., IOLLO, A., LAROCCA, F. "RANS CLOSURE APPROXIMATION BY ARTIFICIAL NEURAL NETWORKS". Lausanne, Switzerland, 2019. Proceedings of 13th European Conference on Turbomachinery Fluid dynamics & Thermodynamics.

[64] BUIST, J., SANDERSE, B., VAN HALDER, Y., et al. "Machine Learning for Closure Models in Multiphase-Flow Applications". Crete, Greece, 2019. 3rd ECCOMAS Thematic Conference on Uncertainty Quantification in Computational Sciences and Engineering.

[65] MA, M., LU, J., TRYGGVASON, G. "Using statistical learning to close two-fluid multiphase flow equations for a simple bubbly system", Physics of Fluids, v. 27, n. 9, pp. 092101, 2015. doi: 10.1063/1.4930004. Disponível em: <https://aip.scitation.org/doi/abs/10.1063/1.4930004>.

[66] MA, M., LU, J., TRYGGVASON, G. "Using statistical learning to close two-fluid multiphase flow equations for bubbly flows in vertical channels", International Journal of Multiphase Flow, v. 85, pp. 336 – 347, 2016. ISSN: 0301-9322. doi: https://doi.org/10.1016/j.ijmultiphaseflow.2016.06.021. Disponível em: <http://www.sciencedirect.com/science/article/pii/S0301932215302226>.

[67] HUANG, D. Z., XU, K., FARHAT, C., et al. "Learning Constitutive Relations from Indirect Observations Using Deep Neural Networks", Journal of Computational Physics, p. 109491, 2020. ISSN: 0021-9991. doi: https://doi.org/10.1016/j.jcp.2020.109491. Disponível em: <http://www.sciencedirect.com/science/article/pii/S0021999120302655>.

[68] LE, B. A., YVONNET, J., HE, Q.-C. "Computational homogenization of nonlinear elastic materials using neural networks", International Journal

for Numerical Methods in Engineering, v. 104, n. 12, pp. 1061–1084, 2015. doi: 10.1002/nme.4953. Disponível em: <https://onlinelibrary.wiley.com/doi/abs/10.1002/nme.4953>.

[69] LING, J., JONES, R., TEMPLETON, J. "Machine learning strategies for systems with invariance properties", Journal of Computational Physics, v. 318, pp. 22 – 35, 2016. ISSN: 0021-9991. doi: https://doi.org/10.1016/j.jcp.2016.05.003. Disponível em: <http://www.sciencedirect.com/science/article/pii/S0021999116301309>.

[70] WANG, K., SUN, W. "A multiscale multi-permeability poroplasticity model linked by recursive homogenizations and deep learning", Computer Methods in Applied Mechanics and Engineering, v. 334, pp. 337 – 380, 2018. ISSN: 0045-7825. doi: https://doi.org/10.1016/j.cma.2018.01.036. Disponível em: <http://www.sciencedirect.com/science/article/pii/S0045782518300380>.

[71] ABADI, M., AGARWAL, A., BARHAM, P., et al. "TensorFlow: Large-Scale Machine Learning on Heterogeneous Systems". 2015. Disponível em: <https://www.tensorflow.org/>. Software available from tensorflow.org.

[72] FRENKLACH, M., MORIARTY, N. W., EITENEER, B., et al. Gri mech 3.0. Relatório técnico. Disponível em: <http://www.me.berkeley.edu/gri-mech/>.

[73] FISCHER, M., JIANG, X. "An assessment of chemical kinetics for bio-syngas combustion", Fuel, v. 137, pp. 293–305, 2014.

[74] ZHANG, K., JIANG, X. "An assessment of fuel variability effect on biogas-hydrogen combustion using uncertainty quantification", International Journal of Hydrogen Energy, v. 43, n. 27, pp. 12499 – 12515, 2018. ISSN: 0360-3199. doi: https://doi.org/10.1016/j.ijhydene.2018.04.196. Disponível em: <http://www.sciencedirect.com/science/article/pii/S0360319918314137>.

[75] WESTBROOK, C. K., DRYER, F. L. "Simplified Reaction Mechanisms for the Oxidation of Hydrocarbon Fuels in Flames", Combustion Science and Technology, v. 27, n. 1-2, pp. 31–43, 1981. doi: 10.1080/00102208108946970. Disponível em: <https://doi.org/10.1080/00102208108946970>.

[76] BIBRZYCKI, J., POINSOT, T., ZAJDEL, A. "Investigation of laminar flame speed of $CH_4/N_2/O_2$ and $CH_4/CO_2/O_2$ mixtures using reduced chemical kinetic mechanisms", Archivum Combustionis, v. 30, pp. 287–296, 2010.

[77] DRISCOLL, J. F. "Turbulent premixed combustion: Flamelet structure and its effect on turbulent burning velocities", Progress in Energy and Combustion Science, v. 34, 2008.

[78] ROGG, B., CANT, R. S., BRAY, K. N. C. "On laminar flamelet modelling of the mean reaction rate in a premixed turbulent flame", Combustion Science and Technology, v. 69, pp. 53–61, 1990.

[79] ACAMPORA, L., MARRA, F., MARTELLI, E. "Comparison of Different CH4-Air Combustion Mechanisms in a Perfectly Stirred Reactor with Oscillating Residence Times Close to Extinction", Combustion Science and Technology, v. 188, pp. 707–718, 05 2016. doi: 10.1080/00102202.2016.1138810.

[80] FRANZELLI, B., RIBER, E., GICQUEL, L. Y., et al. "Large Eddy Simulation of combustion instabilities in a lean partially premixed swirled flame", Combustion and Flame, v. 159, n. 2, pp. 621 – 637, 2012. ISSN: 0010-2180. doi: https://doi.org/10.1016/j.combustflame.2011.08.004. Disponível em: <http://www.sciencedirect.com/science/article/pii/S0010218011002525>.

[81] FEINBERG, J., LANGTANGEN, H. P. "Chaospy: An open source tool for designing methods of uncertainty quantification", Journal of Computational Science, v. 11, pp. 46–57, 2015. Disponível em: <https://doi.org/10.1016/j.jocs.2015.08.008>.

[82] HAKIM, L., LACAZE, G., KHALIL, M., et al. "Modeling Auto-Ignition Transients in Reacting Diesel Jets", Journal of Engineering for Gas Turbines and Power, v. 138, n. 11, 05 2016. ISSN: 0742-4795. doi: 10.1115/1.4033502. Disponível em: <https://doi.org/10.1115/1.4033502>. 112806.

[83] LI, S., YANG, B., QI, F. "Accelerate global sensitivity analysis using artificial neural network algorithm: Case studies for combustion kinetic model", Combustion and Flame, v. 168, pp. 53–64, 2016.

[84] CHEN, Z. "On the accuracy of laminar flame speeds measured from outwardly propagating spherical flames: Methane/air at normal temperature and pressure", Combustion and Flame, v. 162, pp. 2442–2453, 2015.

[85] XIOURIS, C., YE, T., JAYACHANDRAN, J., et al. "Laminar flame speeds under engine-relevant conditions: Uncertainty quantification and minimization in spherically expanding flame experiments", Combustion and Flame, v. 163, pp. 270–283, 2016.

[86] KARUMURI, S., TRIPATHY, R., BILIONIS, I., et al. "Simulator-free solution of high-dimensional stochastic elliptic partial differential equations using deep neural networks", Journal of Computational Physics, v. 404, pp. 109120, 2020. ISSN: 0021-9991. doi: https://doi.org/10.1016/j.jcp.2019.109120. Disponível em: <http://www.sciencedirect.com/science/article/pii/S0021999119308253>.

[87] HUANG, G., , LIU, Z., et al. "Densely connected convolutional networks", Proceedings of the IEEE Conference on Computer Vision and Pattern Recognition, v. 1, pp. 3, 2017.

[88] IOFFE, S., SZEGEDY, C. "Batch normalization: Accelerating deep network training by reducing internal covariate shift", In Int Conf. on Machine Learning, 2015.

[89] GLOROT, X., BORDES, A., BENGIO, Y. v. 15, pp. 315–323, 11–13 Apr 2011. Disponível em: <http://proceedings.mlr.press/v15/glorot11a.html>.

[90] CHOLLET, F. Deep Learning with Python. Manning Publications Company, 2017.

[91] ROBINDS, H., MONRO, S. "A stochastic approximation method", Annals of Mathematical Statistics, v. 22, pp. 400–407, 1951.

[92] WEISBERG, S. Applied Linear Regression. John Wiley & Sons, Inc., 2005.

[93] KINGMA, D. P., BA, J. "Adam: A Method for Stochastic Optimization", 2015. Disponível em: <http://arxiv.org/abs/1412.6980>.

[94] GOVERT, S., MIRA, D., KOK, J. B. W., et al. "The Effect of Partial Premixing and Heat Loss on the Reacting Flow Field Prediction of a Swirl Stabilized Gas Turbine Model Combustor", Turbulence and Combustion, v. 100, 2018. doi: https://doi.org/10.1007/s10494-017-9848-4.

[95] LI, S., LI, S., MIRA, D., et al. "Investigation of dilution effects on partially premixed swirling syngas flames using a LES-LEM approach", Journal of the Energy Institute, v. 91, 2018.

[96] LEE, C.-E., HWANG, C.-H. "An experimental study on the flame stability of LFG and LFG-mixed fuels", Fuel, v. 86, n. 5-6, pp. 649–655, 2007. doi: 10.1016/j.fuel.2006.08.033.

[97] KHALIFA, M. H., AMMAR, M., OUARDA, W., et al. "Particle swarm optimization for deep learning of convolution neural network". In: 2017 Sudan Conference on Computer Science and Information Technology (SCCSIT), pp. 1–5, 2017.

[98] WANG, D., TAN, D., LIU, L. "Particle swarm optimization algorithm: an overview", Soft Computing, v. 22, pp. 387–408, 2018. doi: 10.1007/s00500-016-2474-6.

[99] MIRANDA, L. J. V. "PySwarms, a research-toolkit for Particle Swarm Optimization in Python", Journal of Open Source Software, v. 3, 2018. doi: 10.21105/joss.00433. Disponível em: <https://doi.org/10.21105/joss.00433>.

[100] SERIZAWA, T., FUJITA, H. "Optimization of Convolutional Neural Network Using the Linearly Decreasing Weight Particle Swarm Optimization". 2020. Disponível em: <arXiv:2001.05670>.

[101] CARLISLE, A., DOZIER, G. "An off-the-shelf pso". In: in: Proceeding of Workshop on Particle Swarm Optimization, 2001. Disponível em: <DOI:10.1.1.589.485>.

[102] SARGSYAN, K., HUAN, X., NAJM, H. "EMBEDDED MODEL ERROR REPRESENTATION FOR BAYESIAN MODEL CALIBRATION", International Journal for Uncertainty Quantification, v. 9, n. 4, pp. 365–394, 2019. ISSN: 2152-5080.

[103] CHENG, Y., HUANG, Y., PANG, B., et al. "ThermalNet: A deep reinforcement learning-based combustion optimization system for coal-fired boiler", Engineering Applications of Artificial Intelligence, v. 74, pp. 303 – 311, 2018. ISSN: 0952-1976. doi: https://doi.org/10.1016/j.engappai.2018.07.003. Disponível em: <http://www.sciencedirect.com/science/article/pii/S0952197618301477>.

[104] MAURYA, R. K., SAXENA, M. R. "Characterization of ringing intensity in a hydrogen-fueled HCCI engine", International Journal of Hydrogen Energy, v. 43, n. 19, pp. 9423 – 9437, 2018. ISSN: 0360-3199. doi: https://doi.org/10.1016/j.ijhydene.2018.03.194. Disponível em: <http://www.sciencedirect.com/science/article/pii/S0360319918310279>.

[105] SYED, J., BAIG, R. U., ALGARNI, S., et al. "Artificial Neural Network modeling of a hydrogen dual fueled diesel engine characteristics: An experiment approach", International Journal of Hydrogen Energy, v. 42, n. 21, pp. 14750 – 14774, 2017. ISSN: 0360-3199. doi: https://doi.org/10.1016/j.ijhydene.2017.04.096. Disponível em: <http://www.sciencedirect.com/science/article/pii/S0360319917314854>.

[106] AN, J., WANG, H., LIU, B., et al. "A Deep Learning Framework for Hydrogen-fueled Turbulent Combustion Simulation". 2020.

[107] FREITAS, R. S. M., BARBOSA, C. H. S., GUERRA, G. M., et al. "An encoder-decoder deep surrogate for reverse time migration in seismic imaging under uncertainty". 2020. Disponível em: <arXiv:2006.09550>.

[108] ADAMS, B., BAUMAN, L., BOHNHOFF, W., et al. Dakota, A Multilevel Parallel Object-Oriented Framework for Design Optimization, Parameter Estimation, Uncertainty Quantification, and Sensitivity Analysis: Version 6.0 User's Manual. Sandia Technical Report SAND2014-4633, 2014.

[109] JIANG, X., MIRA, D., CLUFF, D. "The combustion mitigation of methane as a non-CO2 greenhouse gas", Progress in Energy and Combustion Science, v. 66, pp. 176–199, 2018.

[110] EBERHART, R., KENNEDY, J. "A new optimizer using particle swarm theory". In: MHS'95. Proceedings of the Sixth International Symposium on Micro Machine and Human Science, pp. 39–43, 1995.

Appendix A

Model predictive analysis: parametric uncertainties

In addition to errors introduced by computing the reactive chemical process by reduced kinetics, there is a large number of parametric uncertainties in chemical kinetics models, which involve reaction rate constants and thermodynamic parameters, much of which are poorly known [14–16]. The starting point here is to investigate the effects of fuel variability and chemical kinetic uncertainties in combustion using a UQ-based methodology. Furthermore, this study can serve as a basis for further analysis, in an attempt to analyze the impact of the use of simplified mechanisms for renewable fuels searching "best values" in a Bayesian perspective of the kinetic parameters of the most sensitive reactions.

Here, the analysis performed relies on assuming a stochastic model for those parameters to push forward such uncertainties through the simulations (forward analysis) and try to understand the final impact on quantities of interest (QoI), outputs of the simulation. In this study, the PCE method is used to propagate the parametric uncertainties, where the Dakota Sandia [108] software is used to implement the UQ forward analysis.

Firstly, it is investigated the role played by small fluctuations on fuel composition as it occurs in heterogeneous combustion systems. In general, the fuel mixture in practical applications is not precisely known with the amount of CH_4 varying around a nominal value [109]. Following a probabilistic perspective, we model the mass fraction of methane $Y_{CH_4} = \overline{Y_{CH_4}}(1 + \sigma\xi)$, but keeping the amount of fuel fixed to maintain the same equivalence ratio. The overline stands for the expected value (mean), σ the standard deviation and ξ a uniform random variable ($\xi \sim U[-1, 1]$). For this analysis, we picked 6 fuel compositions given by the mean methane amount: $\overline{Y_{CH_4}} = \{50, 55, 60, 65, 70, 75\}$, and $\sigma = 0.05$. The consequences of this sole uncertainties in the prediction of aforementioned QoIs are depicted in Fig. A.1 for different equivalence ratios. It is observed more variability in flame physicochemical

properties for low-concentration methane mixtures than highly CO_2 diluted fuels, see Figs. A.1 and A.2. For low CH_4/CO_2 ratios, the variability in flame thickness and flame speed is larger. This occurs for both lean and rich mixtures with the effects of dilution having a more important role than fuel/air stoichiometry. The uncertainties in fuel composition also impact the resulting adiabatic flame temperature and the formation of CO, following similar trends. This means the utilization of biogas fuels in practical systems needs to account for variations in heat release rate and flame propagation as those shown in Fig. A.1. Figure A.2 shows a view of such scenario regarding only the flame speed, which is a crucial parameter during operation of premixed systems. The same trends are also confirmed here.

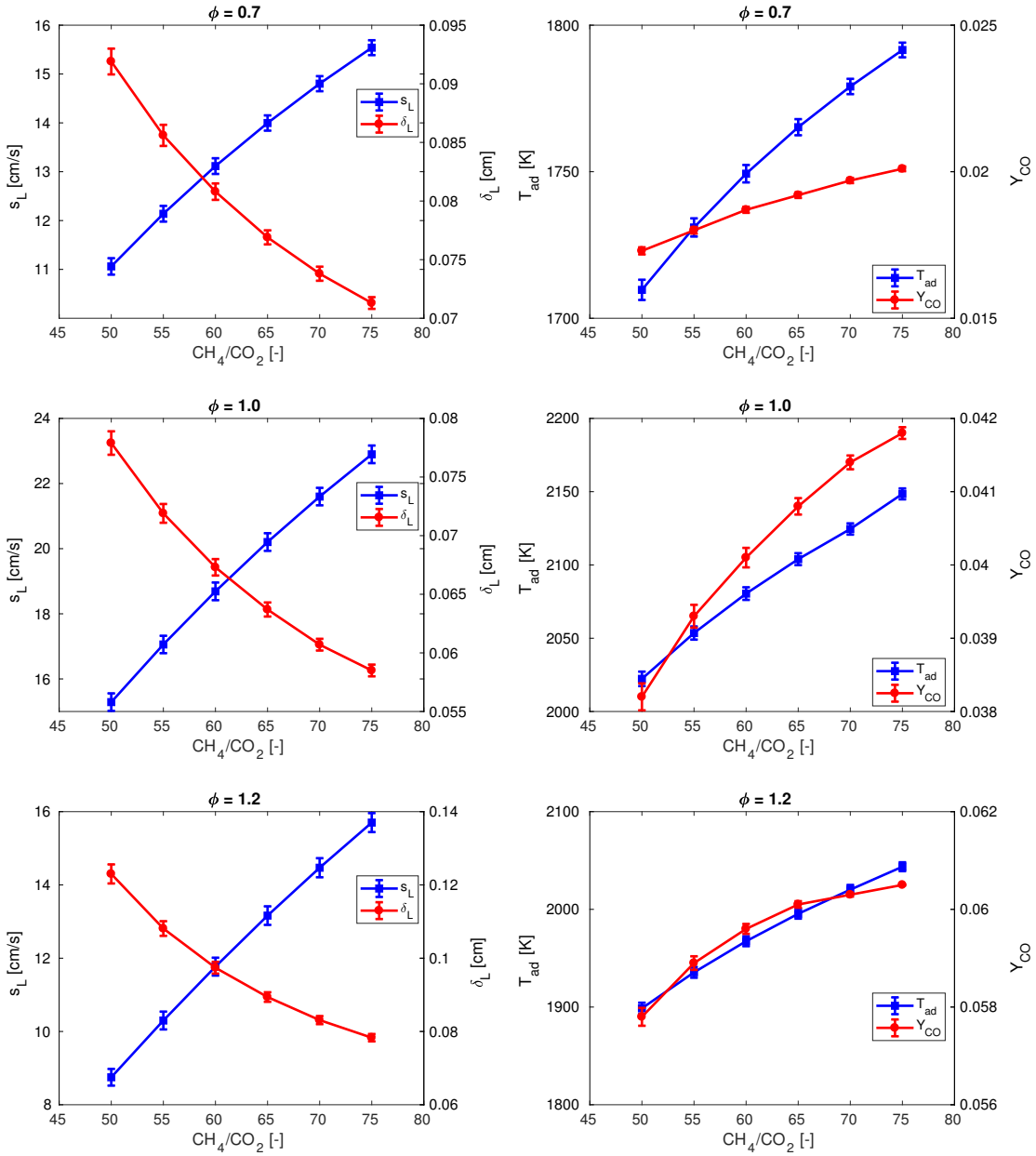

Figure A.1: Influence of fuel composition flame thickness, flame speed, adiabatic temperature and mass fraction of CO. Variation of 5% CH4 at different CH4/CO2 ratios. (GRI3.0)

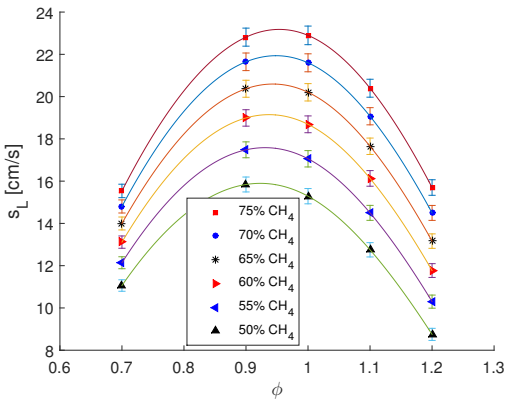

Figure A.2: Influence of fuel composition on flame speed. Variation of 5% CH4 at different equivalence ratios. (GRI3.0)

It is noted that the flame physicochemical properties presented higher variabilities in mixtures with higher concentrations of CO_2. Also, it is verified that small fluctuations of fuel composition slightly impacts the QoIs, around 3% of expected values. Thus, it is expected that uncertainties in the QoIs are due to chemical kinetics parameter uncertainties.

Sensitivity analysis of fundamental flame properties to the reaction rates can reveal the rate-limiting steps controlling the combustion processes and provide valuable insights into mechanism optimization. Here, it is carried out an analysis of the GRI3.0 mechanism from a UQ perspective. More specifically, it is investigated the effects of kinetics parameters on characteristic flame properties. Also, this study can serve as a basis to analyze the impact of using simplified mechanisms for renewable fuels, such as searching "best values" in a Bayesian perspective of the kinetic parameters of the most sensitive reactions.

In practice, kinetic parameters are estimated through indirect, scarce and noisy measurements, so it is natural to think that they bear some level of uncertainty. The aim here is to investigate the impacts caused by small fluctuations in kinetic parameters in practical combustion systems. Now, the uncertainties in the Arrhenius parameters are combined with those in the fuel composition studied before. It is assumed that the reaction rate k for each elementary step is dictated by the Arrhenius expression:

$$k(T) = AT^m e^{-\frac{E}{RT}}, \tag{A.1}$$

where $R = 8.314$ J mol^{-1} K^{-1} is the universal gas constant, T is the temperature, E is the activation energy, A, a positive value, is the pre-exponential constant and m is a model constant.

Due to the high number of reactions composing the detailed mechanism, a sensitivity analysis was performed to identify those reactions that bear more potential to impact the QoIs by the uncertainties. It helps us on obtaining

computational savings along the UQ study. So, a local sensitivity analysis [50] is employed with respect to the flame speed and flame thickness, employing the normalized derivatives: $(k/s_L \cdot \partial s_L/\partial k)$ and $(k/\delta_L \cdot \partial \delta_L/\partial k)$. To study such sensitivity on the main flame quantities, three fuel mixtures are considered and presented in Table 4.1. A baseline fuel containing only methane is included for comparison. Figure A.3 shows the flame speed and flame thickness sensitivities associated to the key reactions in the mechanism for the three fuel mixtures.

The analysis depicted in Fig. A.3 reveals that the flame sensitivities are similar for different fuels, where $H + O_2 \Longleftrightarrow O + OH$ is the most relevant regarding the uncertainty propagation. Thus, it is proposed to investigate the impacts caused by small fluctuations of the most sensitive reaction of GRI3.0 mechanism on the flame physicochemical properties. We consider the combustion chemistry as a kinetic problem with a probabilistic structure by assuming the Arrhenius factor (A) and the activation energy (E) of the most relevant reaction as stochastic variables, keeping all other parameters deterministics. Following a probabilistic perspective, the stochastic variables are modeled as:

$$\begin{aligned} A &= \overline{A}(1 + \sigma_A \xi), \\ E &= \overline{E}(1 + \sigma_E \xi), \end{aligned} \tag{A.2}$$

where $(\overline{A}, \sigma_A) = (2.650 \times 10^{16}, 0.05)\ s^{-1}$ and $(\overline{E}, \sigma_E) = (17.041 \times 10^3, 0.05)\ cal/mol$, while ξ is an independent random variable with uniform distribution [-1, 1]. Therefore, the domains of variability of the stochastic variables A and E are $[2.5175 \times 10^{16}, 2.7825 \times 10^{16}]\ s^{-1}$ and $[16.1889 \times 10^3, 17.8931 \times 10^3]\ cal/mol$, respectively. The uncertainties are presented in Figure A.4, the results indicate that Arrhenius parameters play a major part in the kinetics, since small fluctuations on Arrhenius parameters cause a high variability on the flame characteristics. Nevertheless, the difference between the three cases is not significant. These results suggest that the use of reduced schemes for methane/air oxidation would be a good starting point to develop optimized schemes for biogas, as the variations in fundamental flame parameters due to composition variations is relatively small and could be captured by the same schemes.

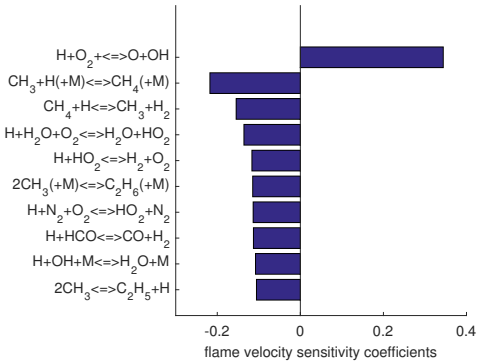

(a) Baseline flame speed sensitivity

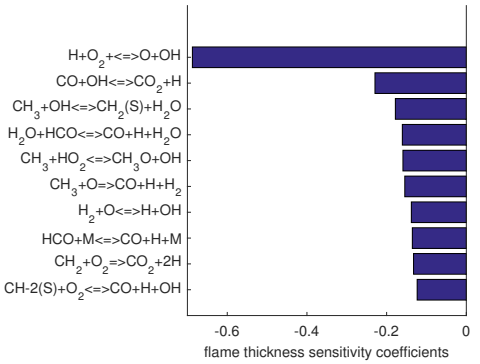

(b) Baseline flame thickness sensitivity

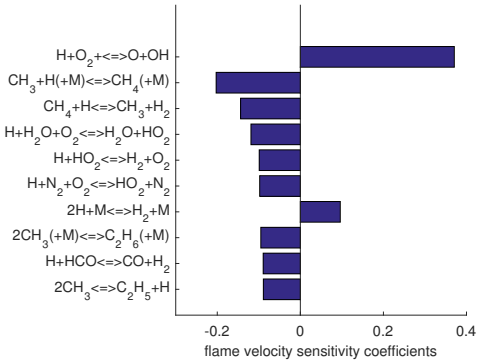

(c) BG1 flame speed sensitivity

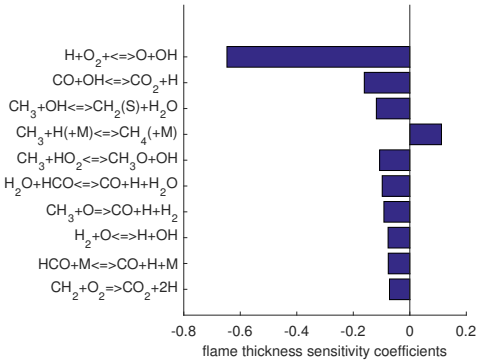

(d) BG1 flame thickness sensitivity

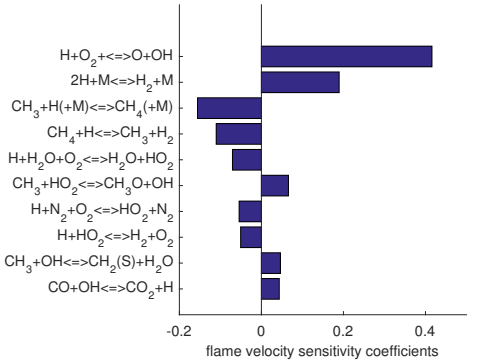

(e) BG2 flame speed sensitivity

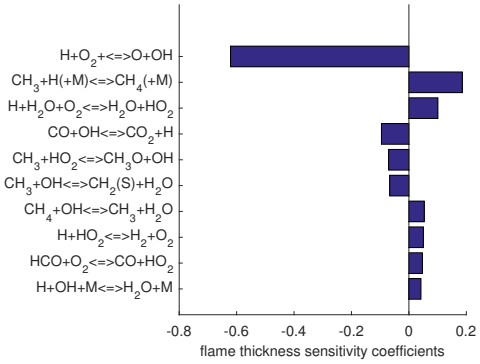

(f) BG2 flame thickness sensitivity

Figure A.3: Flame sensitivity analysis of difference fuels at stoichiometric conditions.

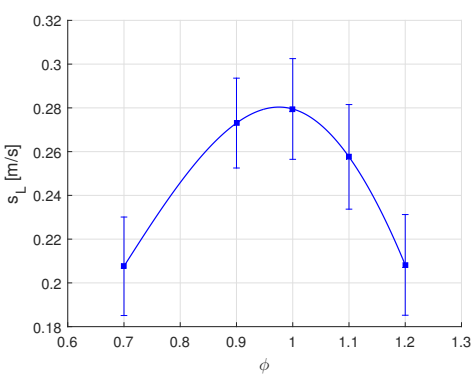

(a) Baseline flame speed

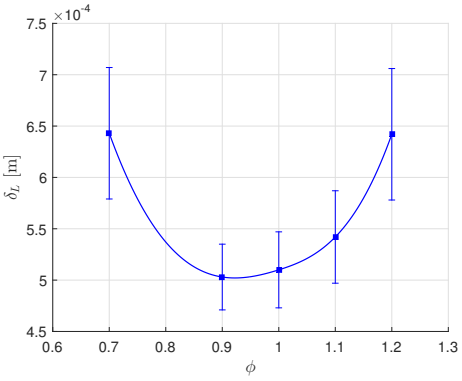

(b) Baseline flame thickness

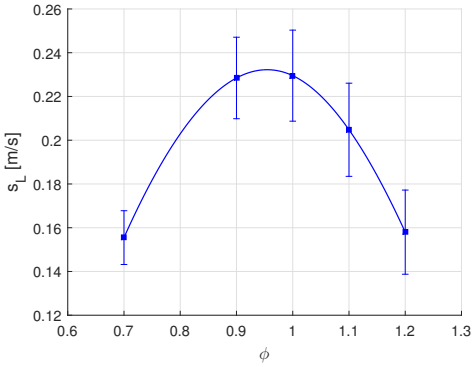

(c) BG1 flame speed

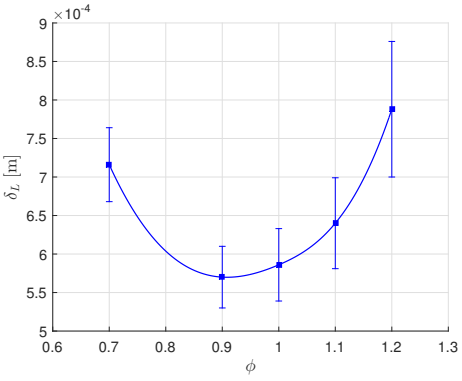

(d) BG1 flame thickness

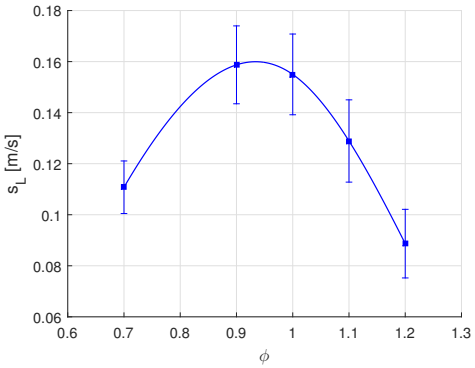

(e) BG2 flame speed

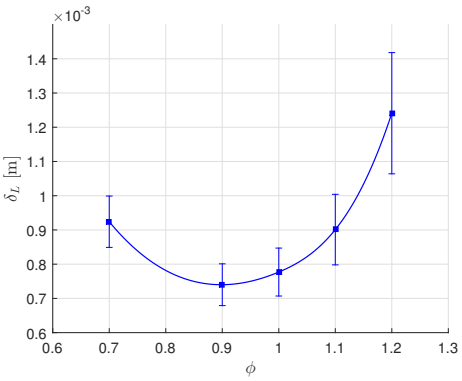

(f) BG2 flame thickness

Figure A.4: Influence of fuel composition and Arrhenius parameters on the flame speed and thickness at different equivalent ratios.

Appendix B

Neural network model discrepancy - First analysis

B.0.1 Hydrogen homogeneous combustion

Here, the neural network model discrepancy approach proposed in section 3.1.2 is applied to chemical kinetics model of hydrogen during homogeneous combustion. It is calibrated a five steps reduced model of H_2/O_2 combustion proposed by [11]. The data employed for calibration is provided by simulation results produced with a detailed mechanism also proposed by [11]. More specifically, the detailed mechanism is composed of 8 species and 21 reactions while the reduced mechanism contains 7 species and 5 reactions.

For the 0-d scenario, that low-fidelity mechanism can estimate with a good agreement the ignition delay time when compared with the full mechanism. However, the predictions of the temporal evolution of the states are far from being satisfactory, mainly after the ignition process. Therefore, it is employed a discrepancy term to the low fidelity mechanism which is embedded in the net production rates of species according Eq. (4.20). Also, it is chosen as training data fifty equally time-spaced points of the temporal evolution of the temperature profile for H_2-air mixture at atmospheric pressure, stoichiometric condition, and a range of initial temperature $T_0 \in [1200, 1500K]$ varying by $30K$. So, the training dataset is composed of 550 temperature points.

Also, the PSO method with the same settings as section 4.3 is used to train the model discrepancy term. Figures B.1(a), B.2(a), B.3(a) and B.4(a) show the temporal evolution of the temperature for the operating conditions given by the inlet temperatures equal 1200, 1300, 1400, and 1500 K, respectively. It can be seen that the enhanced model can improve the ability of the reduced model to predict the time-temperature distribution. More specifically, the enhanced model can compute the temporal evolution with L_2 relative errors lower than 10% compared to the

full mechanism. Furthermore, it is verified that the improved reduced mechanism predict with a satisfactory agreement the mass fractions of the major species, as shown in Figs. B.1(b,c), B.2(b,c), B.3(b,c) and B.4(b,c).

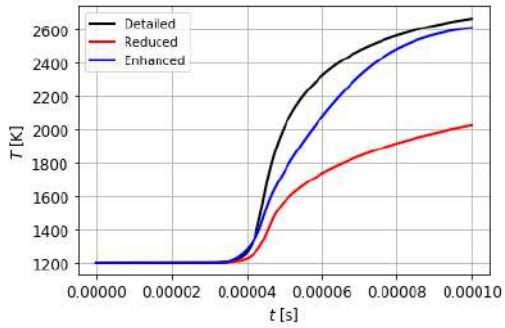

(a) Temperature

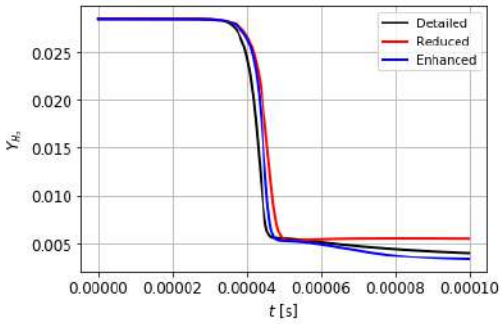

(b) H_2 mass fraction

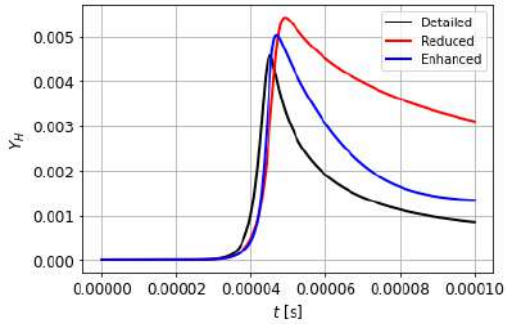

(c) H mass fraction

Figure B.1: Physicochemical properties for hydrogen combustion in the autoignition process at at $p = 1$ bar and $T_0 = 1200K$.

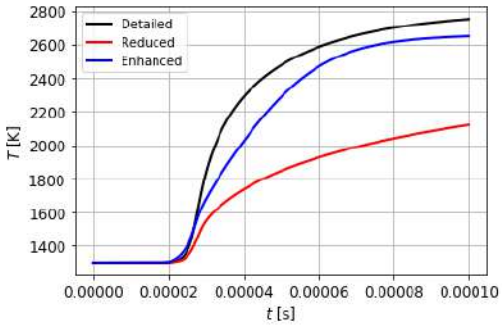

(a) Temperature

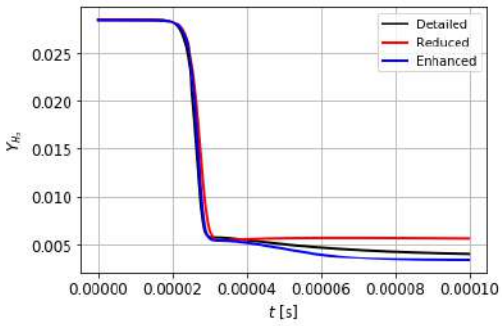

(b) H_2 mass fraction

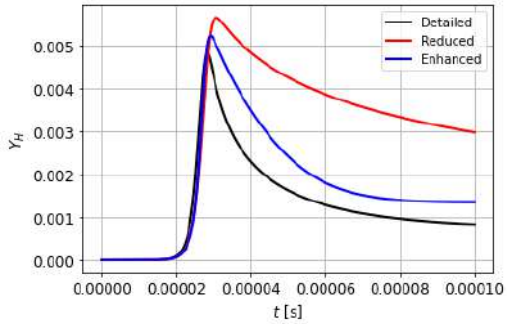

(c) H mass fraction

Figure B.2: Physicochemical properties for hydrogen combustion in the autoignition process at at $p = 1$ bar and $T_0 = 1300K$.

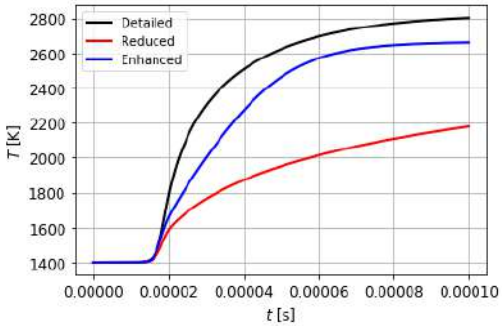

(a) Temperature

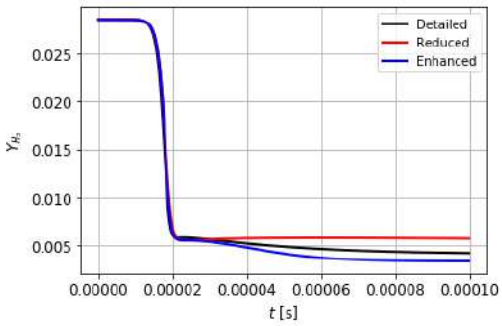

(b) H_2 mass fraction

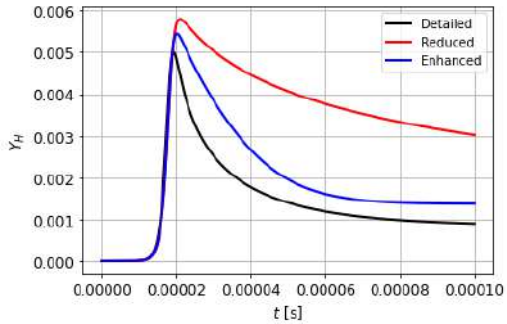

(c) H mass fraction

Figure B.3: Physicochemical properties for hydrogen combustion in the autoignition process at at $p = 1$ bar and $T_0 = 1400K$.

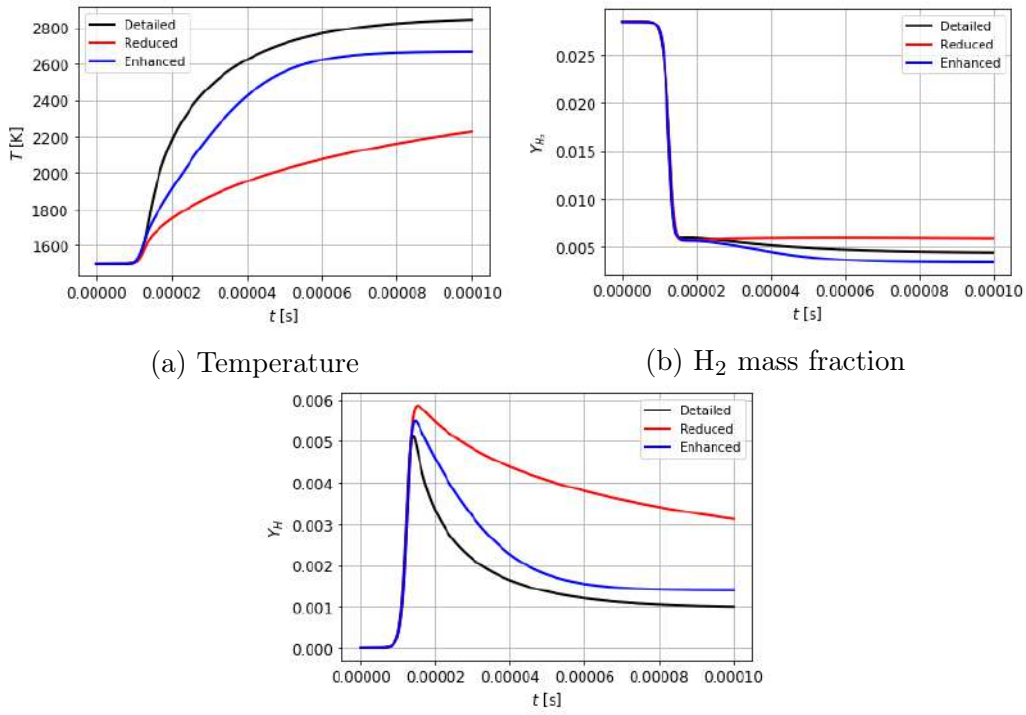

(a) Temperature

(b) H_2 mass fraction

(c) H mass fraction

Figure B.4: Physicochemical properties for hydrogen combustion in the autoignition process at at $p = 1$ bar and $T_0 = 1500K$.

B.0.2 Derivative-free optimization: Particle swarm optimization

In many optimization problems arising from scientific, engineering, and machine learning applications, objective and constraint functions are dependent only on the experiments outputs and/or predictions of a black-box simulation that do not provides derivative information. Such settings necessitate the use of methods for derivative-free, or zeroth-order, optimization.

Particle swarm optimization (PSO) is a stochastic optimization scheme based on the swarm population, simulating the animal social behavior, including insects, herds, birds, and fishes [110]. PSO algorithm is a computational method for optimizing the problem by improving the target solution iteratively.

In this scheme, each individual is called a particle defined as a potential solution of the optimized problem in an D-dimensional search space, and it can memorize the optimal position of the swarm and that of its own, as well as the velocity. In each iteration, the particles information is combined together to adjust the velocity of each dimension, which is used to compute the new position of the particle. Particles change their states constantly in the high-dimensional search space until they reach the global optimal. The unique connection among different dimensions of the problem space is introduced via the objective functions.

The mathematical description of PSO can be described as an ensemble of particles constituting a swarm of size N_{swarm}, wherein the particle position vector in the D-dimensional search space is $\mathbf{x_p} = (x_{p_1}, x_{p_2}, \ldots, x_{p_D})$, velocity vector is $\mathbf{v_p} = (v_{p_1}, v_{p_2}, \ldots, v_{p_D})$, the individual optimal position that each particle has experienced $\mathbf{P_l} = (P_{l_1}, P_{l_2}, \ldots, P_{l_D})$, and global optimal position that the swarm has experienced $\mathbf{P_g} = (P_{g_1}, P_{g_2}, \ldots, P_{g_D})$. Here, without loss of generality, the individual and the global optimal positions are those minimizing the objective function, i.e.,

$$\mathbf{P_l}^{t+1} = \begin{cases} \mathbf{x_p}^{t+1}, & \text{if } f(\mathbf{x_p}^{t+1}) < f(\mathbf{P_l}^t) \\ \mathbf{P_l}^t, & \text{otherwise} \end{cases} \tag{B.1}$$

$$\mathbf{P_g}^{t+1} = \begin{cases} \mathbf{x_p}^{t+1}, & \text{if } f(\mathbf{x_p}^{t+1}) < f(\mathbf{P_g}^t) \\ \mathbf{P_g}^t, & \text{otherwise} \end{cases} \tag{B.2}$$

, where $f(\cdot)$ represents the objective function.

The velocity and position of the particles in each iteration t is given as follows

$$\mathbf{v_p}^{t+1} = \omega_v \mathbf{v_p}^t + c_1 r_1 (\mathbf{P_l}^t - \mathbf{x_p}^t) + c_2 r_2 (\mathbf{P_g}^t - \mathbf{x_p}^t) \tag{B.3}$$

$$\mathbf{x_p}^{t+1} = \mathbf{x_p}^t + \mathbf{v_p}^{t+1} \tag{B.4}$$

, where r_1 and r_2 are random numbers in $\mathcal{U} \in [0, 1]$. In the velocity update equation (B.3), we can note that in this updated formula, the first term takes account of the previous particle velocity from inertial weight ω_v. It means that the particle has confidence in the previous state and starts moving from it. The second term depends on the distance between the particle current position and its optimal position. So, the particle moves resulting from its own experience. Thus, the parameter c_1 is called the cognitive learning factor. The third term relies on the distance between the current position of the particle and the global optimal position in the swarm, wherein the information is shared and cooperated among the particles, i.e., the moving of the particle depends on the swarm moving. Thereby, c_2 is called social learning factor.

The PSO algorithm is shown in Algorithm 3.

Algorithm 3 Particle swarm optimization

iter = 0
Initialize the swarm: position vector $\mathbf{x_p}$ (randomly) and velocity vector $\mathbf{v_p}$ (randomly)
while $iter \leq iter_{max}$ **do**
    for $i = 1$ to N_{swarm} **do**
        for $j = 1$ to D **do**
            Update the velocity and position of the particles from Eqs.(B.3) and (B.4).
        end for
        Assess the value of particle i
        if $f(\mathbf{x_i}^{t+1}) < f(\mathbf{P_i}^{t})$ **then**
            $\mathbf{P_i}^{t+1} = \mathbf{x_i}^{t+1}$
        end if
    end for
    $k = \arg min f(\mathbf{P_i}^{t+1})$
    if $f(\mathbf{x_k}^{t+1}) < f(\mathbf{P_g}^{t})$ **then**
        $\mathbf{P_g}^{t+1} = \mathbf{x_k}^{t+1}$
    end if
    $t + 1$
end while

Where *iter* is the number of iterations.